MECHANICS IN BIOLOGY OF PROGENITORS: SPHEROID GROWTH MODELING IN SILICO AND MECHANICAL INDUCTION OF HUMAN HEPATIC STEM CELL PHENOTYPE IN VITRO

Oswaldo Alonso Lozoya Iñiguez

A dissertation submitted to the faculty of the University of North Carolina at Chapel Hill in partial fulfillment of the requirements for the degree of Doctor of Philosophy in the Joint Department of Biomedical Engineering

Chapel Hill
2011

Approved by:

Dr. Lola M. Reid (co-chair)

Dr. Sharon R. Lubkin (co-chair)

Dr. Elizabeth Loboa (academic advisor)

Dr. Farshid Guilak

Dr. Richard Superfine

ABSTRACT

Stem cell biology is a collection of multivariate phenomena with strict regulatory mechanisms. These regulatory mechanisms assemble biological systems that coordinate growth and differentiation during development and remain in determined stem cells of adult tissues. In order to control these complex systems, biologists can, on the one hand, investigate how individual mechanisms affect global responses in stem cells, and on the other hand, explore how multiple mechanisms act in coordination to control the behavior of developing tissues. The types of stimuli traditionally studied in stem cell biology are biochemical; however, mechanics of stem cell environments also influence stem cell biology.

The objective of this thesis is to survey roles of mechanical variables in directing mechanisms of stem cell biology and growth of developing tissues. This inspection uses two approaches: an experimental system (*in vitro*) that controls a small set of variables to reveal their roles in stem cell biology; and a biomathematical model (*in silico*) that defines a biological system to study the effects of interactions between multiple variables on growth of developing tissues. The *in vitro* model shows that the mechanical properties of three-dimensional (3D) environments regulate phenotype of determined stem cells from the human liver. The *in silico* model reveals that growth of spheroids with properties of developing tissues exhibits two morphogenetic regimes, and explains quantitatively how expansion stops in growing spheroids that degrade their surroundings.

Each of these two models has strong implications for tissue engineering. Both models unveil paradigms of stem cell and developing tissue behavior, which researchers can use to optimize experimental conditions. Furthermore, this thesis evaluates stem cell biology from two distinct perspectives, which brings empirical and predictive aspects of tissue engineering one step closer to each other and creates useful models to close this gap.

To Kristin, my wife and the love of my life, and all my family near and far.

ACKNOWLEDGMENTS

I would like to express my sincere gratitude to my advisors and mentors, Drs. Sharon R. Lubkin and Lola M. Reid, who guided and encouraged me to pursue and achieve the visions and objectives I had for my doctoral education. Their continuous guidance and the opportunity of joining their research teams made all this work possible. I would like to extend my regards to my academic advisor, Dr. Elizabeth Loboa, for her patience and support during the management of my graduate curriculum and guidance in the fulfillment of departmental graduation requirements. I would also like to acknowledge the remaining members of the dissertation committee, Drs. Farshid Guilak and Richard Superfine, who provided access to multiple experimental resources in their research groups and trusted me with using them judiciously, as well as their support throughout my research.

My deepest gratitude goes to my family and loved ones, for supporting and believing in me at all times. The faith and love they deposit in me continually is the driving force of my ambitions, and their care and concern for my personal advance at all levels is the strength that keeps me motivated in times of despair and doubt. For all these and many more reasons, this dissertation is dedicated, first and foremost, to my wife, Kristin Lozoya. My dedications also extend to my roots back in Mexico: my mother, Verónica Angélica Iñiguez; my father, Luis Raul Lozoya; and my brothers Juan Raul and Luis Gerardo. Their relentless support in times of local hardship at my home country is inspiring and shows, without doubt, their belief in me. This dissertation is dedicated to my wife's family as well: Jackie Hackett, my

mother-in-law; Robert Hackett, my father-in-law; and Samantha Hackett, my sister-in-law. They made enduring the distance from my family back in my home country easier to bear by welcoming me into theirs with open arms and hearts. Thank you all for wishing me the best always, and thank you for being an intrinsic part of me.

This work could have not been completed without the support of the multiple research groups I worked with, both at Duke University and UNC at Chapel Hill. Special thanks go to Nancy McKinney, whose invaluable help with class registration across both institutions in the Joint Graduate Program of Biomedical Engineering at UNC and NCSU made it possible for me to maintain a successful curricular status. Special mention goes to Claire Barbier, Lucendia English, Eva Schmelzer, Rachael Turner, Eliane Wauthier and everyone directly involved in the daily activities within the Reid Lab, to whom I give my deepest appreciation.

Funding support for the fulfillment of this dissertation originated from multiple sources. All of the biomathematical studies were financed by grants from NSF (DMS-0201094) and NIH (1R01GM096195-01) to SR Lubkin. All of the experimental studies at the Reid Lab were financed by grants to LM Reid, including NIH grants (AA014243, IP30-DK065933), a Department of Energy Grant (DE-FG02-02ER-63477) and sponsored research grants from Vesta Therapeutics (Bethesda, MD) and GigaCyte (Branford, CT). Funding for one semester towards my salary and for studies at the Center for Computer Integrated Systems for Microscopy and Manipulation in UNC Chapel Hill were provided by an NIH project grant to R Superfine (5-P41-EB002025). Studies at the Orthopaedic Bioengineering Laboratory in Duke University were financed by an NIH grant to F Guilak (AR50245).

This dissertation was submitted to the evaluating Committee on February 28th, 2011.

TABLE OF CONTENTS

LIST OF TABLES

LIST OF FIGURES

CHAPTER 1. INTRODUCTION

The critical characteristics distinguishing tissues and their function arise from cells that establish maturational lineages during development. Cells define these maturational lineages with regulatory signaling mechanisms that define gradients of phenotypic properties within tissues. These regulatory mechanisms fit particular functions that fetal, childhood, adult and geriatric stages require throughout life. Each tissue specializes to perform specific functions, mediated by characteristic gene expression profiles, through lineage progression, a paradigm of stem cell and maturational lineage biology *in vivo* [1]. Differentiation mechanisms correspond to specific paracrine signaling at each stage; therefore, it is not surprising that differentiation studies traditionally focus on biochemical signals in stem cells from all stages in development (embryonic stem cells to determined ones) and each of the embryonic germ layers (endoderm, mesoderm, ectoderm).

The extracellular matrix (ECM) is a complex insoluble composite found outside of all cells that stabilizes their lineages within three-dimensional (3D) arrays. The ECM maintains each cell within appropriate configurations of antigens, receptors, transporters and ion channels, thus enabling them to respond optimally to their neighbors. The ECM components, along with bound soluble signals, present a solid-state apparatus for signaling that optimizes cells responses to their microenvironment. However, the extracellular matrix (ECM) composition also operates as a biological signal because it transitions with differentiation to assemble functional environments that cells physically need. The nature of ECM molecules,

with binding affinity to soluble signals, turn gradients in ECM chemistry into differential signaling sources, as seen in glycosaminoglycan (GAG) chains of proteoglycans (PGs) [1-4].

Each cell type in a tissue experiences mechanical forces differently, even when the tissue receives homogeneous mechanical stimulation, because the physical microenvironment evolves across the tissue's maturational gradient. Historically, researchers have overlooked this aspect when studying endodermal tissues (i.e. soft organs) that they considered mechanically unresponsive. However, limits in intercellular and diffusive transport demand that mechanical forces participate in tissue function and direct cellular activity (even if it is difficult to isolate their effects). In other words, mechanical forces help secretory organs respond quickly to systemic and local variations in physiology during healthy conditions.

Stem cell biology is a collection of multivariate phenomena. It requires carefully designed experiments with strict multivariate control to study interactions between differentiation mechanisms. Some of these tasks can be optimized by mathematical schemes. However, other multivariate conditions cannot be reproduced experimentally. It is possible to define differentiation paradigms and use them in mathematical models by quantifying cellular processes in stem cell biology with targeted experimental models. The research presented here discusses two methodologies that investigate roles of mechanics in stem cell biology. With that end, this work defines two models, one *in vitro* (experimental) and one *in silico* (computational), which lay initial groundwork to determine differentiation paradigms in response to mechanical input. Future research can enrich our knowledge of mechanotransduction in stem cell biology by transitioning between both models.

CHAPTER 2. UNDERSTANDING LIVER PHYSIOLOGY AS A ROADMAP TO STEM CELL BIOLOGY

Liver is formed by thousands of functional units called acini, which in histological sections appear hexagonal. Each acinus has terminal branches of the portal vein, hepatic artery and bile duct at each vertex – called the portal triad – and a central vein discharging to the hepatic veins on their way to the inferior vena cava. Blood flows from the portal triad to the pericentral vein across fenestrated capillaries, called hepatic sinusoids, which are lined by liver cells. In liver, the periportal-to-pericentral direction down the hepatic sinusoids maps the hepatic maturational gradient.

The Reid lab has studied hepatic maturational gradients extensively. In humans, the hepatic maturational gradient starts with a stem cell niche hosting hepatic stem cells (hHpSCs) around the portal triads. Cells in the next lineage stage, hepatoblasts (hHBs), are adjacent to them, operate as transit amplifying cells and can differentiate to biliary fates. From here on, hepatic sinusoids cross plaques of hepatocytes differentiated into later maturational stages with increasing size and ploidy, decreasing expression of stem cell genes and low-to-null cell division potential. Mesenchymal companion cells match lineages in hepatic epithelial cells across the hepatic maturational gradient, from angioblasts (ABs) at the portal triad down to endothelial and hepatic stellate cells (hHpSTCs) at later stages.

The ECM composition evolves within the hepatic maturational gradient. In liver, GAGs and PGs in the periportal region with poor to no sulfation, such as hyaluronan (HA)

and chondrotin sulfate proteoglycan (CS-PG), transition into highly sulfated ones like heparin proteoglycan (HP-PG) and heparan sulfate proteoglycan (HS-PG). Higher sulfation levels could make PGs more susceptible to chemical interactions like disulfide bridging (e.g. cross-linking) at the pericentral regions of the maturational gradient. In other words, the PG sulfation gradient in hepatic maturational gradients could suggest a concomitant stiffness gradient that also participates in homeostatic regulation and differentiation. Profiles of glycoprotein distribution – from laminin to fibronectin – as well as collagens – from network collagens in basal membranes (collagens III and IV) to fibrillar ones (collagen I) – also support this stiffness-dependent interpretation for intrahepatic differentiation.

The coming chapter discusses, in further detail, how the hepatic maturational gradient relates to gradients in paracrine signaling, phenotype, epithelial-mesenchymal interactions and matrix composition that dictate hepatic lineage specification. Later, we use this information to explore the role of mechanical properties of the microenvironment in hepatic stem cell differentiation.

CHAPTER 3. HUMAN HEPATIC STEM CELL AND MATURATIONAL LIVER LINEAGE BIOLOGY[1]

3.1. ABSTRACT

Livers are comprised of maturational lineages of cells beginning extrahepatically in the hepato-pancreatic common duct near the duodenum and intrahepatically in zone 1 by the portal triads. The extrahepatic stem cell niches are the peribiliary glands deep within the walls of the bile ducts; those intrahepatically are the canals of Hering in postnatal livers and that derive from ductal plates in fetal livers. Intrahepatically, there are at least 8 maturational lineage stages from the stem cells in zone 1 (periportal), through the midacinar region (zone 2), to the most mature cells and apoptotic cells found pericentrally in zone 3. Those found in the biliary tree are still being defined. Parenchymal cells are closely associated with lineages of mesenchymal cells, and their maturation is coordinated. Each lineage stage consists of parenchymal and mesenchymal cell partners distinguishable by their morphology, ploidy, antigens, biochemical traits, gene expression, and ability to divide. They are governed by changes in chromatin (e.g. methylation), gradients of paracrine signals (soluble factors and insoluble extracellular matrix components), mechanical forces, and feedback loop signals derived from late lineage cells. Feedback loop signals, secreted by late lineage stage cells into bile, flow back to the periportal area and regulate the stem cells and other early lineage

[1] Turner R, Lozoya OA, Wang Y, Cardinale V, Gaudio E, Alpini G, Mendel G, Wauthier E, Barbier C, Alvaro D, Reid LM. Human hepatic stem cell and maturational liver lineage biology. *Hepatology*. In press, 2011;

stage cells, in mechanisms dictating the size of the liver mass. Recognition of maturational lineage biology and its regulation by these multiple mechanisms offers new understandings of liver biology, pathologies, and strategies for regenerative medicine and treatment of liver cancers.

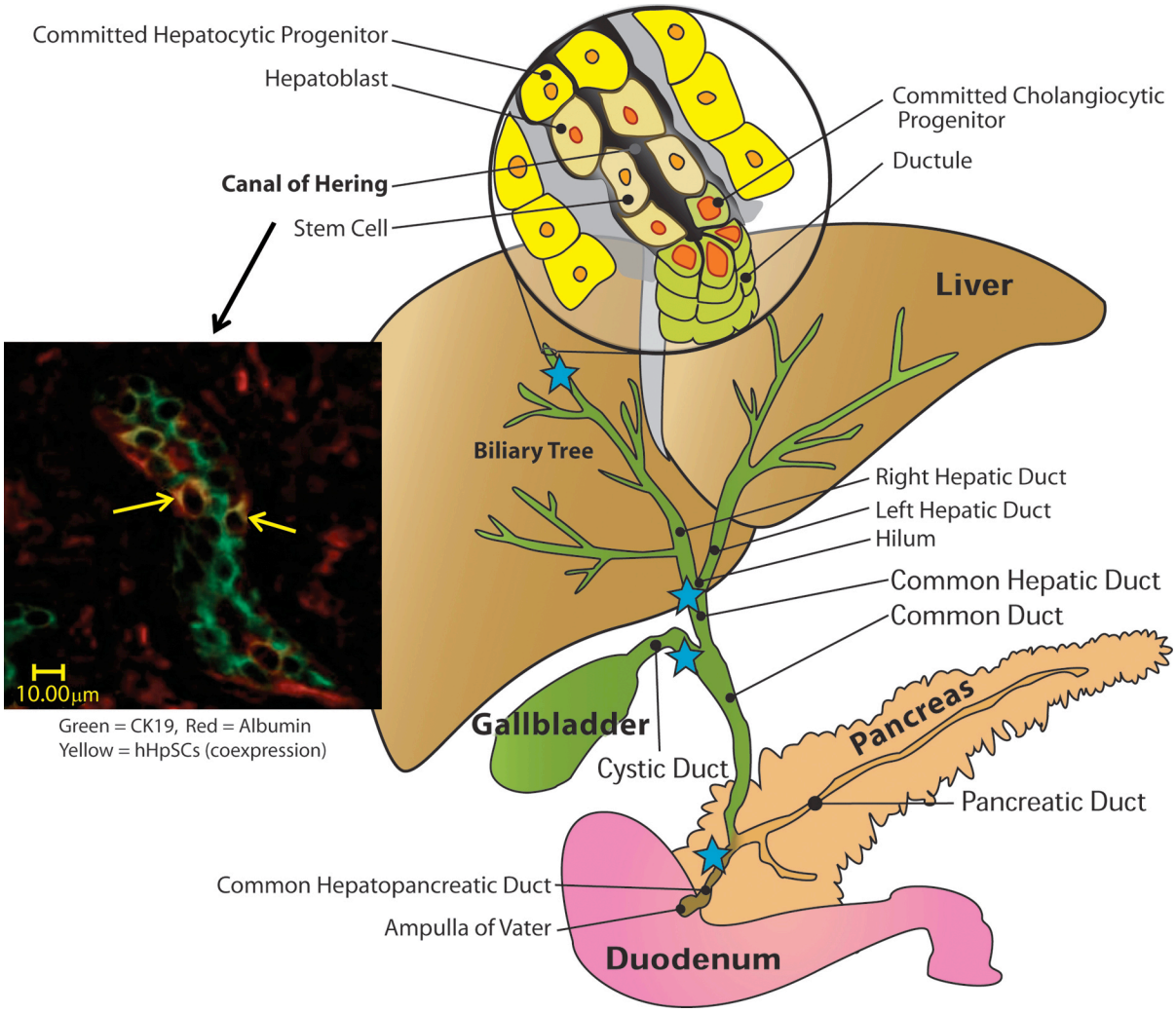

Figure 1. Schematic image of liver, the biliary tree, and pancreas and their connections with the duodenum. The blue stars indicate sites at which there are high numbers of peribiliary glands, the stem cell niches of the biliary tree.

3.2. THE LIVER'S MATURATIONAL LINEAGES

Hepatic stem cells and their mesenchymal partners, angioblasts, give rise to daughter cells maturing into lineages of parenchymal and mesenchymal cells with stepwise changes in cell size, morphology, ploidy, gene expression, growth potential and signaling [3, 5-7]. Currently, there is evidence for at least 8 intrahepatic lineage stages (Figure 1 and Figure 2) [8, 9]. Continued efforts to characterize the liver's lineage biology should result in recognition of additional stages. This overview focuses on early intrahepatic lineage stages in human livers and includes aspects of their regulation. Information on later lineage stages of cells, additional background and references is included in the online supplement.

Stage 1. Hepatic stem cells (hHpSCs) are multipotent stem cells located within the liver's stem cell compartment, the ductal plates of fetal and neonatal livers, and canals of Hering in pediatric and adult livers [9-15]. The compartment represents the anatomic and physiological link between the intralobular canalicular system of hepatocytes and the biliary tree and resides along sites that project starlike from the portal tracts. They constitute ~0.5-2% of the parenchyma of livers of all age donors. The hHpSCs cells range in size from 7-10μm in diameter and have a high nucleus-to-cytoplasm ratio. Tolerant of ischemia, they can remain viable in cadaveric livers for up to ~6 days after asystolic death [13, 15].

The hHpSC phenotypic profile includes epithelial cell adhesion molecule (EpCAM), neural cell adhesion molecule (NCAM), CD133, CXCR4, SOX9, SOX17, FOXA2, cytokeratins(CK) 8/18/19, Hedgehog proteins (Sonic and Indian), intranuclear telomerase protein, claudin 3, MDR1, weak expression of albumin and MHC antigens. They do not express α-fetoprotein (AFP), intercellular adhesion molecule (ICAM-1), P450s, or markers for hemopoietic (e.g. CD34/38/45/90, glycophorin), endothelial (e.g. VEGFr, CD31, von

Willebrand factor) or mesenchymal cells (e.g. CD146, desmin, vitamin A, CD105) [8, 12, 16]. It remains unclear whether C-kit (CD117), expressed in the liver's stem cell niches [14, 17, 18], is on hHpSCs or associated angioblasts, as CD117+ flow cytometry selects for angioblasts [12, 16].

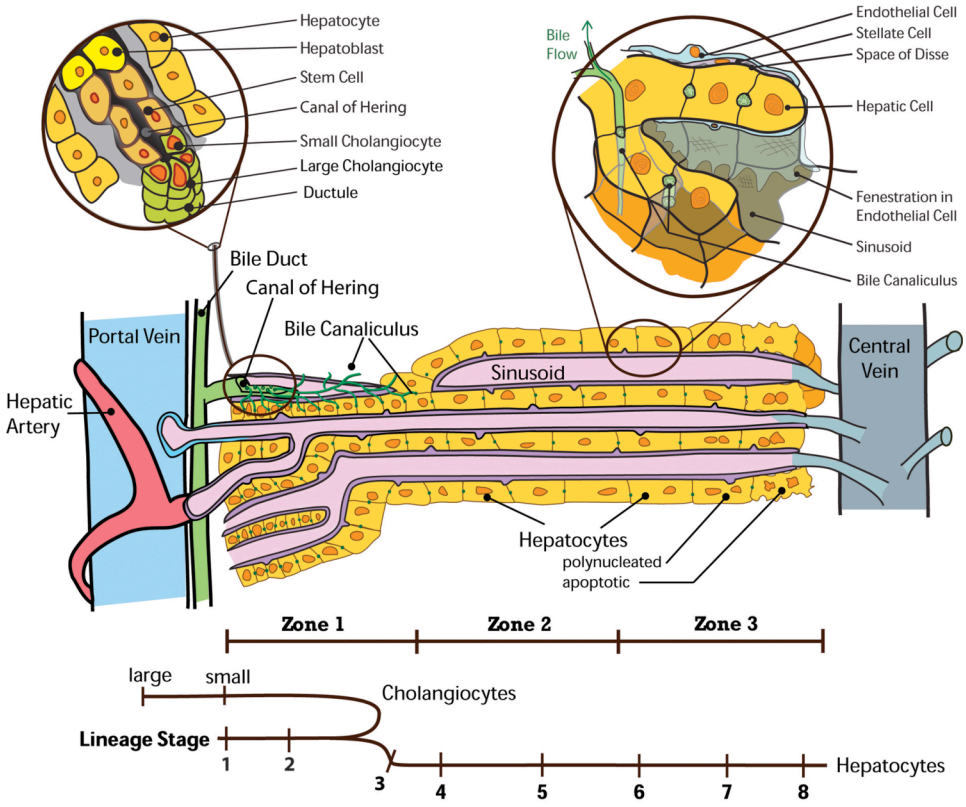

Lineage Stage (of viable cells)	1	2	3	4	5	6	7
Parenchymal Cells	Hepatic stem cells (hHpSCs)	Hepatoblasts (hHBs)	Committed progenitors	Diploid Adult cells: Periportal parenchymal cells	Diploid Adult cells: Midacinar hepatocytes	Diploid Adult cells: Pericentral diploid hepatocytes	Tetraploid pericentral parenchymal cells
Mesenchymal cells	Angioblasts	Endothelial and Stellate Cell Precursors		Endothelia (hepatocytes) Stellate Cells (cholangiocytes)	Endothelia	Endothelia	Endothelia
Size	7-10μm	10-12μm	"Small Cholangiocytes" 6-7μm Hepatocytic progenitors 12-15 μm	"Large Cholangiocytes" ~14μm Hepatocytes 18-20μm	22-25μm	25-30μm	>30μm
Growth	Maximum (complete cell division)			Intermediate (complete cell division)		Negligible (DNA synthesis but with little, if any cytokinesis)	
Genes	Early			Intermediate		Late	
Matrix	Type III, IV, and V collagens, laminins, hyaluronans, CS-PGs, HS-PGs			<<<<Gradient>>>>		Type III, IV, VI collagens, HP-PGs	

Lineage Stage 8 consists of apoptotic cells located near the central vein.

Figure 2. Schematic image of intrahepatic maturational lineages.

Some proteins, such as CK19, are synthesized and found in punctuate form, but not converted to filaments, as seen in hepatoblasts [12]. Similarly, little albumin is synthesized but not packaged as in later lineage stages, implicating lineage-dependent distinctions in post-transcriptional and translational protein processing.

The hHpSCs are isolated by dual immunoselection for EpCAM+/NCAM+ cells from livers of all donor ages. In adult livers, which have scarce hepatoblast populations, EpCAM+ selection alone results in predominant hHpSCs isolation [8, 12].

In culture, the hHpSCs form colonies capable of self-replication [19] and of differentiation to mature cells in culture and *in vivo* [12, 16]. Cells expand *ex vivo* if cultured in Kubota's Medium, a serum-free medium containing only insulin, transferrin/fe, lipids, no copper, and low calcium [20, 21] or if co-cultured with angioblasts. These feeders are replaceable with purified type III collagen substrates, low cross-linking hyaluronan hydrogel embedding or a mixture of both [16, 22]. If transplanted *in vivo*, they yield mature liver tissue. If cultured under distinct conditions (see below) they lineage-restrict into hepatoblasts [23].

Stage 2. Hepatoblasts (hHBs) are diploid bipotent cells giving rise to hepatocytic and cholangiocytic lineages, associated with precursors of both endothelia and hepatic stellate cells, and the liver's probable transit amplifying cells [16]. They reside throughout parenchyma of fetal and neonatal livers or as single cells and small cell aggregates tethered to the ends of canals of Hering in adult livers [14]. With donor age, hHBs decline to <0.01% of the parenchymal cells in postnatal livers [12, 14]. They expand during regenerative processes associated with certain diseases such as cirrhosis. Previously, hHBs were referred to as "intermediate hepatobiliary cells of the ductular reactions" [24]; extensive

characterization enabled us to update their nomenclature with hepatoblasts [14]. They can be isolated by dual immunoselection for EpCAM+/ICAM-1+. They have enormous expansion potential cultured in Kubota's Medium, especially if supplemented with EGF and HGF, or on feeders of stellate cell precursors replaceable by substrata of type IV collagen, laminin, hyaluronans or mixtures of these, albeit without proven self-replication [16, 25, 26].

The hHBs, larger (10-12μm) and with higher amounts of cytoplasm than hHpSCs, have an antigenic profile that overlaps with hHpSCs [8, 12, 18]. Shared phenotypic traits include CXCR4, CD133, SOX17, MDR1, cytokeratins(CK) 8/18 and 19, Hedgehog proteins (Sonic and Indian), and null expression of late P450s (e.g. P450-3A) or markers for hemopoietic, endothelia or mesenchymal cells (as in hHpSCs). Protein expression changes include reduction in EpCAM levels with primary localization to plasma membrane surfaces; filamentous CK14 and CK19 [9, 14, 27]; elevated albumin levels with discrete cytoplasmic packaging [12]; switch from NCAM to ICAM-1; expression of early P450s (e.g. P450-A7) and CK7; and strong positive expression of hepatic-specific AFP, distinct from a hemopoietic progenitor variant form with alternative splicing of exon 1, a probable clue of mesendoderm to endoderm differentiation [28]. They have approximately 5X the telomerase activity of hHpSCs and telomerase protein localized both in the nucleus and in the cytoplasm [29]. A comparison of the phenotypic profiles of HpSCs and HBs can be found in Table 1, Figure 3 and Figure 4.

Stage 3. Committed progenitors are ~12-15μm diploid, unipotent, immature cells. These precursors give rise to only one adult cell type. They lose most stem cell gene expression (e.g. NCAM, Hedgehog proteins), express either hepatocytic or biliary markers, and abound in fetal and neonatal tissues or chronic liver diseases (viral, alcoholic and non-

alcoholic fatty liver diseases, autoimmune hepatitis, cholangiopathies), unlike normal adult tissues [30].

Table 1. Phenotypic profiles of multipotent cell populations in human livers.

Property	**Human Hepatic Stem Cells (hHpSCs)**	**Human Hepatoblasts (hHBs)**
Average diameter (measured by forward scatter in flow cytometric analyses of isolated cells)	7-9 μm	10-12 μm
Nucleus to cytoplasmic ratio	Highest observed of all parenchymal progenitor subpopulations evaluated	Intermediate between that in hHpSCs and mature parenchymal cells
Percentage of parenchymal cells [12]	0.5-1.5 % in livers of all donor ages and with minimal ischemia; percentages higher in ischemic livers	>80% (fetal livers)
		~50% (neonatal livers) [percentages change rapidly day by day postnatally]
		<0.01% (adult livers)
Survival after cardiac arrest (tolerance for ischemia) [12]	Viable cells for several days after cardiac arrest	Viable for more than a day, but not as long as hHpSCs
Morphology of colonies *in vitro* [12]	Uniform; densely packed; look similar to ES cell colonies	Cord-like colonies interspersed with clear channels that are presumptive canaliculi
Evidence for Self-renewal [31]	Clonogenic expansion with stability of phenotype; doubling times of ~36 hours on plastic; can be passaged repeatedly; fastest doubling times (~20-24 hours) for hHpSCs on substrata of type III collagen	Significant expansion potential but not yet evidence for self-replication (under the conditions tested to date). Probable transit amplifying cells
Pluripotency [12]	Multipotent	Bipotent
Anaerobic metabolism (metabolomic studies) [22]	+++	+++
Conditions for clonogenic expansion [20]	Kubota's Medium plus feeders of angioblasts replaceable with type III collagen (monolayers) or hyaluronans into which is mixed type III collagen (3-D)	Kubota's Medium plus feeders of hepatic stellate cells replaceable with type IV collagen/laminin (monolayers) or hyaluronans into which is mixed type IV collagen/ laminin (3-D)
CD44 (hyaluronan receptor) [26]	High concentrations	High concentrations
Claudin 3 [8]	+++	Negative

Indian Hedgehog [9]	+++ Highest level in cells in the center of the colonies	++ Lower levels, but pattern of distribution is the same
Sonic Hedgehog [9]	++ Located at edge of cells; concentrated in cells at edge of colonies at sites of high concentration of angioblasts	+ Lower levels, but pattern of distribution is the same
Patched (Hedgehog receptor) [9]	+++ Found in all cells and in colonies throughout the colony	++ Levels lower, but still evident
Telomerase [29]	+ mRNA encoding telomerase and the protein found in nucleus. No telomerase protein in the cytoplasm	+++ mRNA encoding telomerase and the protein found in nucleus; with differentiation, increasing numbers of the cells have it in the cytoplasm; 5X higher activity than in hHpSCs
P450s [8]	Negative for all assayed	P450 A7 but not late forms of P450s
CK 8 and 18 [8]	++	++
CK 19 [8, 12]	++ (not in filament form)	++ (filaments evident)
E-cadherin [12]	++	++
EpCAM [12, 14]	+++ (throughout the cells)	++ (plasma membrane)
NCAM /ICAM-1 [12, 14]	++ /-	-/++
Albumin [12]	±	++
α-fetoprotein [12, 14]	Negative	+++
Mesenchymal Markers[2]	Negative	Negative
Angioblasts/ **Endothelial Cell Markers**[3]	Negative	Negative
Hemopoietic markers[4]	Negative	Negative

[2] Mesenchymal markers found on hepatic stellate cells and myofibroblasts: α-smooth muscle actin (ASMA), desmin, CD146)MeICAM), vitamin A, VCAM, HGF, and SDF-1α. The precursors to the stellate cells express lower levels of these markers.

[3] Angioblasts/Endothelial cell markers: CD31, VEGFr, von Willebrand factor, VCAM, and on hemangioblast subpopulations: CD34. *Note: CD117 was found inconsistently on cells within hHpSC colonies and was never observed on hHB colonies. Flow cytometric sorting for CD117+ cells from fetal liver cell suspensions yielded angioblasts. Therefore, we assume that it is on angioblasts closely associated with the hHpSCs.*

[4] Hemopoietic markers: CD14, CD34, CD38, CD45, CD90, glycophorin A (red blood cell antigen).

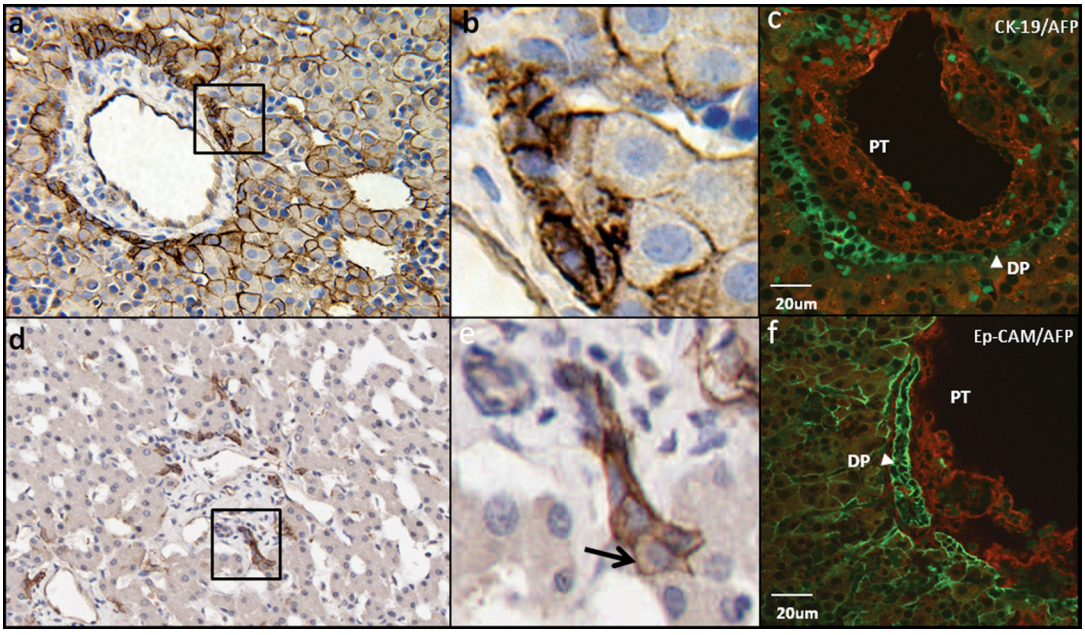

Figure 3. Human hepatic stem cell and hepatoblast phenotypes *in vivo*. a,b) EpCAM expression in fetal liver: EpCAM expressed in the ductal plate is not only at the cell surface but also in the cytoplasm. EpCAM expressed in the hepatoblasts is specific to the cell surface. d,e) EpCAM expression in adult liver: one end of the Canal of Hering connects to the bile duct, the other end connects to hepatoblasts (arrow), indicating that the hepatoblasts are derived from primitive hepatic stem cells harbored in Canals of Hering. c) Double staining for CK-19/AFP and f) EpCAM/AFP of human fetal liver in the portal triad area and analyzed by confocal microscopy. CK-19 (c, green) is expressed not only by remodeling ductal plates but faintly expressed by some of the hepatoblasts. EpCAM (f, green) is detected in all the parenchymal cells and biliary epithelial cells forming bile duct and ductal plate (DP). AFP (red) is expressed by hepatoblasts throughout the fetal liver and undetectable in the ductal plate. PT: Portal triad; DP: Ductal Plate. Originally published in Hepatology, DOI:10.1002/hep.22516 [14][5] and J Exp Med, DOI:10.1084/jem.20061603 [12][6].

Committed hepatocytic progenitors, also called intermediate hepatocytes, express albumin, enzymes associated with glycogen synthesis (e.g. glucose-6-phosphate), and lack biliary markers (e.g. CK19) and AFP. They are associated with endothelial cell precursors and are located *in vivo* in the liver plates between the HBs and the diploid adult hepatocytes.

[5] ©John Wiley and Sons. Zhang L, Theise N, Chua M, Reid LM. The stem cell niche of human livers: symmetry between development and regeneration. *Hepatology*. 2008; 48:1598-607

[6] ©Schmelzer E, Zhang L, Bruce A, Wauthier E, Ludlow J, Yao HL, et al. Originally published in *J Exp Med*. 204:1973-87. doi:10.1084/jem.20061603

"Small cholangiocytes" are diploid biliary cells, 6-8μm with cuboidal shape, a high nucleus-to-cytoplasm ratio, small endoplasmic reticulum [32, 33], and are associated with hepatic stellate cell precursors [16]. They co-localize with hHpSCs in the stem cell niche, lining the canals of Hering, intrahepatic bile ducts and bile ductules with internal diameters below 15μm. Direct links between the canals of Hering and bile ductules, which may traverse the limiting plate and thus may have an intralobular segment (periportal) in addition to their intraportal location, support current hypotheses that point to small cholangiocytes as committed biliary progenitors [34]. In human and rodent livers, they express high levels of the anti-apoptotic proteins annexin V and bcl2 (B-cell lymphoma 2 protein). At a functional level, they express endothelin receptors type A (EDNRA) and type B (EDNRB), endogenous opioid peptides, insulin, histamine (H1), acetylcholine (M3), and α-1-adrenergic agonists, aquaporin 4; they are negative for the Cl-/HCO3- exchanger and receptors for secretin or somatostatin. During chronic feeding with bile salts taurocholate and taurolithocholate, small cholangiocytes express otherwise negative Na+-dependent apical bile acid transporter (ABAT) *de novo*, suggesting a role in the cholehepatic recirculation of bile salts in conditions of overload [35]. Finally, cystic fibrosis transmembrane conductance regulator (CFTR) is present in human, but not rodent, small cholangiocytes [34].

Stages 4-6. Diploid adult cells are the only parenchymal cells with significant proliferative capacity under all known *in vitro* or *in vivo* conditions. Exceptions are in conditions potentially involving genetic reprogramming through chromatin demethylation, the only known mechanism for restoring cytokinensis, as occurs in tyrosinemia [36] or with massive loss of mature parenchymal cells (e.g. >80%) due to a transgene [37]. Diploid adult hepatocytes ("small hepatocytes"), partnered with endothelia, can undergo 6-7 rounds of

division within 3 weeks in culture but have limited subcultivation capacity [20]. Large cholangiocytes, partnered with stellate cells, are columnar shape, display a small nucleus and conspicuous cytoplasm, an abundant Golgi apparatus between the apical pole and the nucleus, and rough endoplasmic reticulum more abundant than small cholangiocytes [33, 38, 39]. Large cholangiocytes line interlobular ducts located in the portal triads. The connections of hHpSCs in canals of Hering to the septal and segmental bile ducts has not yet been investigated, and markers in septal ducts, segmental ducts and larger ducts are found also in cells in peribiliary glands, the stem cell niches of the biliary tree [40]. Large cholangiocytes express CFTR and Cl-/HC03- exchanger, aquaporin 4 and aquaporin 8, secretin and somatostatin receptors other than receptors for hormones and neuropeptides. In addition, they express the Na+-dependent bile acid transporter ABAT (apical bile acid transporter), MDR (multidrug transporter) and MRP (multidrug resistance associated proteins). When large cholangiocytes are damaged by acute carbon tetrachloride (CCl4) or GABA administration, small cholangiocytes proliferate, and acquire phenotypical and functional features of large cholangiocytes [41, 42], suggesting that the population of small cholangiocytes lining the canals of Hering and ductules may represent precursors of large cholangiocytes lining larger ducts. The integrated differential gene expression between small and large normal cholangiocytes demonstrate through microarray that the proteins related to cell proliferation tend to be highly expressed by small cholangiocytes, whereas large cholangiocytes express functional and differentiated genes [39]. This is consistent with studies showing, either with bile duct injury due to CCl4 and GABA administration or with bile duct regrowth following partial hepatectomy, that small cholangiocyte proliferation is activated presumably to repopulate bile ducts. These findings suggest that small cholangiocytes are less mature, have

a high resistance to apoptosis, and have marked proliferative activities, while large cholangiocytes are more differentiated contributing mainly to ductal bile secretion and absorption. Therefore, while hepatocytic cell lineages proceed from periportal areas toward the central vein, cholangiocytes proceed in the opposite direction from canals of Hering/ductules toward larger ducts. See the online supplement (Section 3.5) for further information.

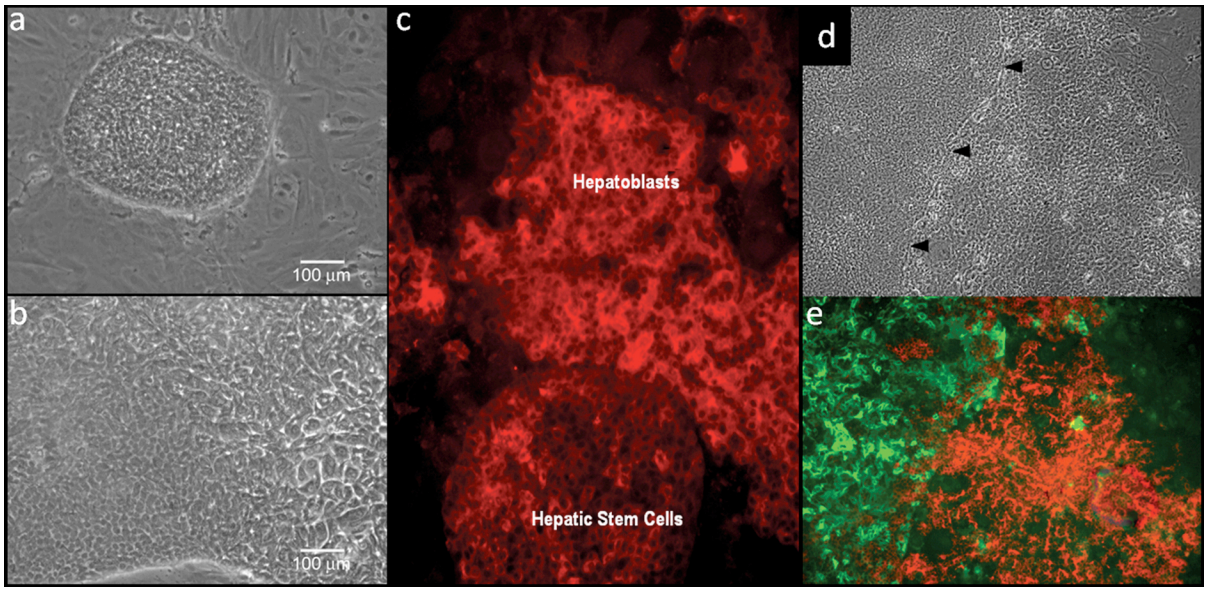

Figure 4. Human hepatic stem cell and hepatoblast phenotypes in culture. a) Morphology of human hepatic stem cells and b) human hepatoblasts in culture on plastic. c) Albumin staining of human hepatic stem cells, transitioning to hepatoblasts. d) The border between the hepatic stem cell colony and hepatoblast outgrowths is marked by arrowheads by phase microscopy; this border is also distinguishable by e) fluorescence microscopy of hepatic stem cells stained with NCAM (green) and hepatoblasts stained with ICAM (red). Originally published in Hepatology, DOI:10.1002/hep.22516 [14][7] and J Exp Med, DOI:10.1084/jem.20061603 [12][8].

[7] ©John Wiley and Sons. Zhang L, Theise N, Chua M, Reid LM. The stem cell niche of human livers: symmetry between development and regeneration. *Hepatology*. 2008; 48:1598-607

[8] ©Schmelzer E, Zhang L, Bruce A, Wauthier E, Ludlow J, Yao HL, et al. Originally published in *J Exp Med*. 204:1973-87. doi:10.1084/jem.20061603

3.3. REGULATION OF THE PARENCHYMAL CELL LINEAGES

3.3.1. Paracrine Signaling between Epithelial-Mesenchymal Partners

Paracrine signaling is the primary form of regulation between parenchymal cells and partnering mesenchymal cells and represents classic epithelial-mesenchymal relationships widely described in developmental biology since the 1930s. A new facet is that coordinate maturation of these [parenchymal]:[mesenchymal] cell associations, starting with [hHpSCs]:[angioblasts] and splitting into lineages of [hepatocyte]:[endothelia] and [cholangiocyte]:[stellate cells], gives rise to lineage-dependent gradients of paracrine signals [16] that govern the biological responses of cells at each lineage stage. Defined subsets of these lineage-dependent paracrine signals, soluble and insoluble matrix ones, can be used to establish cells at a specific lineage stage in culture (Figure 5).

The intrahepatic stem cell niche contains type III collagen, α6β4 integrin-binding form of laminin, hyaluronans and a minimally sulfated chondroitin sulfate proteoglycan (CS-PG) [16]. Transition to [hHBs]:[endothelia and stellate cell precursors] results in changes to type IV collagen, αVβ1 integrin-binding laminin, hyaluronans, more sulfated CS-PGs and forms of heparan sulfate-PGs (HS-PGs). The [hepatocyte]:[endothelia] lineages are associated with network collagens (e.g. type IV and VI) and increasingly sulfated forms of HS-PGs ending, in zone 3, in heparin-PGs (HP-PGs). The [cholangiocyte]:[stellate cell] lineages are associated with fibrillar collagens (e.g. types I and III) and progression from CS-PGs towards highly sulfated PGs, including dermatan sulfate-PGs (DS-PGs) [16, 26, 31]. Many soluble signals bind to and work synergistically with matrix components to regulate the cells, particularly PGs and their glycosaminoglycan chains (GAGs). Matrix-bound soluble signals

are biphasic, yielding mitogenic versus differentiative responses depending on the specific matrix chemistry with which they are associated.

3.3.2. Feedback Loop Signaling

Late lineage stage cells produce positive and negative signaling regulators, including bile salts, various soluble factors and matrix components [43]. Positive regulators include hepatopoietin, released by dying zone 3 cells that stimulate stem/progenitors expansion (M. Roach, J. Hambor, unpublished observations). Negative regulators include ecto-nucleotidases expressed by portal hepatoblasts like NTPDase2, which inhibits purinergic activation of basolateral P2Y receptors in periportal cholangiocytes under homeostatic conditions. Conversely, loss of NTPDase2 expression after experimental cholestasis in portal hepatoblasts allows activation of periportal P2Y receptors and increases cholangiocyte proliferation [44].

Another facet of regulation is mediated by acetylcholine. It stimulates proliferation of stem/progenitor cells and cholangiocytes expressing M3 acetylcholine receptors [45]. In normal liver and even after partial hepatectomy, late lineage stage hepatocytes lacking M3 receptors release acetyl cholinesterase into the bile that delivers it to zone 1 where it destroys acetylcholine in the stem cell niche, thus blocking proliferation of stem/progenitor cells and cholangiocytes. In contrast, during conditions of pericentral damage, the acetyl cholinesterase is not released, resulting secondarily in induction by acetylcholine of stem/progenitor cell expansion. Denervated transplanted livers lack acetylcholine modulation of proliferation of cells lining the canals of Hering. Hepatitis-injured transplanted livers also exhibit lower numbers of progenitor and reactive ductular cells than innervated matched

controls. Experiments in rats with galactosamine-damaged livers confirm that vagotomy induces impaired regeneration of progenitors and ductal reaction in cholangiocytes [46].

Mechanotransduction mechanisms are another major set affecting lineage biology, most involving cytoskeletal rearrangements. The cytoskeleton is a ubiquitous cellular component with characteristics of amplification systems and connections with matrix. Some of these connections allow cells to sense microenvironment rigidity through non-muscle myosin II, which directs stiffness-dependent differentiation in mesenchymal stem cells [47]. Germ layer organization and cell sorting depends on cell adhesion forces and cortex tension relying on actomyosin network activity [48]. Integrins connect the cytoskeleton to matrix substrata, recruit focal adhesions that adapt cells to mechanical stresses, bind ligands and regulate intracellular signaling [49]. Mechanical stretch in liver cells induces activation and synthesis of morphogens in the TGF-β family of Activin/Nodal signaling [50]. SMAD transcription factors regulate TGF-β signaling pathways and regulate gene expression through kinesin-mediated nucleocytoplasmic shuttling along intact microtubules [51, 52].

Primary cilia in cells from soft organs also participate in mechanotransduction by probing and amplifying the effects of intraluminal flow above cell apical surfaces. They mediate polarized signal transduction pathways that use the cytoskeleton to ensure specific and non-diffusable signal trafficking to the nucleus [53]. PDGRα and Hedgehog signaling take place in primary cilia [54, 55] in livers of all ages [9] through dynein-mediated shuttling of Gli transcription factors [56]. Some chromatin targets of Gli transcription factors include PTCH, WNT and BMP genes, all involved in embryonic development and differentiation mechanisms [57-59]. Hedgehog expression gradients also demarcate the extension of

endodermal organs during development [55, 60]. In conjunction, this information suggests primary cilia are relevant participants in endoderm maturation and differentiation.

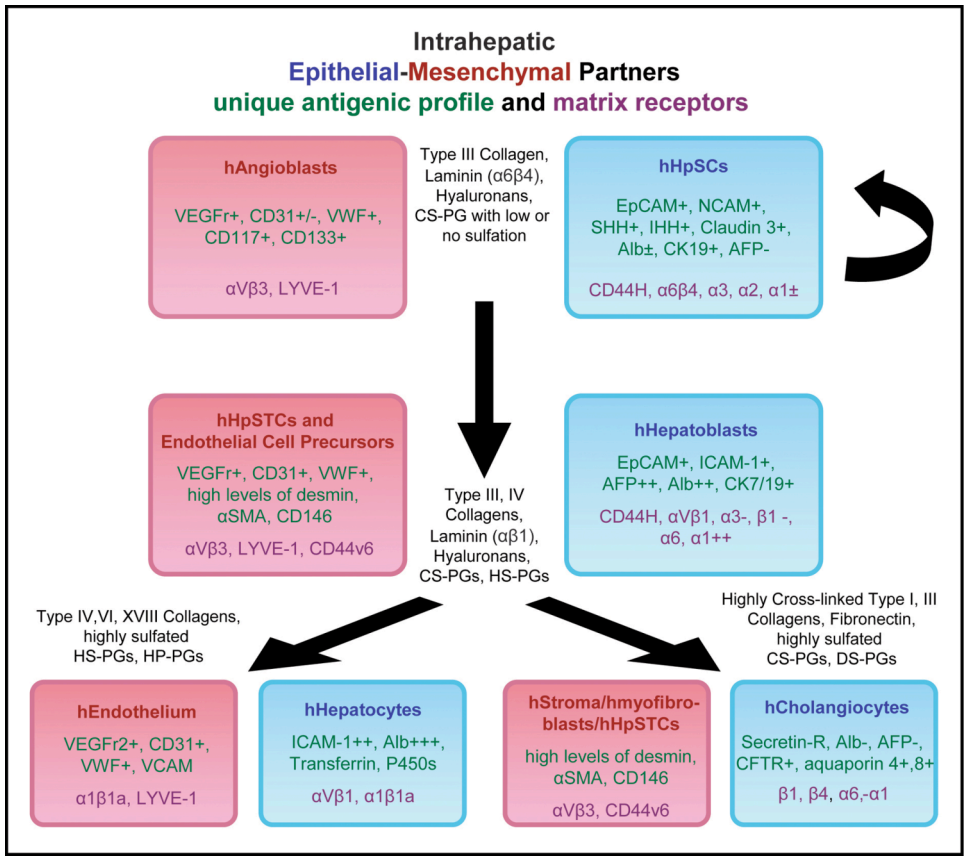

Figure 5. Schematic image indicating the coordinate maturation of the epithelia (parenchymal cells) and their mesenchymal partners and some of the identified extracellular matrix components found at the particular lineage stages. Not shown in the figure are the soluble signals that are also lineage dependent. Some of the lineage dependent soluble signals identified are noted in parentheses beside the lineage stage at which they are found: hepatic stem cells (LIF, IL-6, IL-11, and acetylcholine); hepatoblasts (HGF, EGF, bFGF, IL-6, IL-11, and acetylcholine); hepatocytes (HGF, EGF, bFGF, T3, glucagon, and hydrocortisone); cholangiocytes (VEGF, HGF, bFGF. and acetylcholine).

Bile secretion is an important mechanism for homeostatic control of tissue mass, operating as an inductor in mechano-transduction. Bile is a Newtonian fluid in normal physiological conditions with salt concentration-dependent viscosity [61]. Bile tonicity increases while flowing in the pericentral-to-periportal direction as hepatic parenchyma

perform secretory functions. Abnormal bile tonicity is characteristic of pathological conditions [62]. Shear forces from bile flow, proportional to bile viscosity, function as long-range mechanical signals communicating states of hepatic function across the entire liver maturational gradient to cholangiocytes in the proximal biliary tree through primary cilia bending. This bending triggers stress-induced Ca2+, cAMP signaling cascades and receptor-mediated PDGRα and Hedgehog signaling, which makes bile a mechanical probe for liver homeostatic control [45].

Liver Regeneration. Two distinct forms of liver regeneration take place after: a) partial hepatectomy, and b) selective loss of pericentral cells. After partial hepatectomy, feedback loop signaling is essentially intact. DNA synthesis occurs in cells across the liver plates but only a portion of the cells undergo cytokinesis, yielding increased numbers of polyploid cells, higher numbers of apoptotic cells, and more rapid turnover of the liver with restoration of the normal ploidy profiles within weeks [63]. Feedback loop signaling is the explanation for liver cells in culture in which secreted signals from late lineage stage cells inhibit the growth of any early lineage stage cells [21].

Selective loss of pericentral cells with toxic injury to zone 3 cells (and sometimes also to zone 2) results in muting of the feedback loop signaling that activates rapid cell division of early lineage stage cells [15, 64]. In response, periportal cells undergo rapid hyperplastic growth (complete cell division) followed by differentiation. These phenomena, the classic "oval cell response" in rodents and the "ductular reactions" seen in human massive hepatic necrosis (e.g. acetaminophen toxicity, acute hepatotropic viral infection), have long been recognized to involve extensive expansion of the stem/progenitor cell populations [15]. Chronic injury to the liver, as occurs with repeated drug exposures, radiation, or certain viral

infections like hepatitis B or C, result in loss of late lineage stage cells, eliciting chronic regenerative responses.

3.3.3. Relevance to Clinical Programs

Hepatic lineage biology and mechanisms of its regulation will have relevance for many clinical programs. Examples include tissue sourcing for clinical programs, strategies for liver cell therapies, immunological issues, and most profoundly an understanding of liver tumors and logical strategies by which to treat liver cancers.

Sourcing of tissue for any clinical therapy is dictated by the proportion of cells at the different lineage stages in tissue of a given donor age. Fetal and neonatal tissues with lineages skewed towards early stages will be ideal for stem/progenitor cell therapies, whereas adult livers will be ideal for programs requiring rapid need for late lineage stage functions.

Liver cell therapies for inborn errors of metabolism will be affected by feedback loop signaling, since there will be no selection for the transplanted cells over endogenous cells necessitating higher numbers of cells to be transplanted. By contrast, patients with liver failure due to virus, drugs or radiation (involving a loss of feedback loop signals) can be transplanted with smaller numbers of cells given the strong selective pressure for transplanted cells to expand quickly to reconstitute liver mass.

Concerns regarding a need for immunosuppression will be affected by lineage biology. Non-immunogenic stem/progenitors can acquire immunogenicity with maturation that potentially can be managed by use of stellate cells, known to produce immunomodulatory signals. Liver cell therapies should also use grafting methods that optimize liver engraftment and prevent cell loss to ectopic sites unlike vascular route delivery, especially for stem/progenitors [65].

3.3.4. Liver Cancer Stem Cells

The idea that cancers are transformed stem/progenitor cells originated with the pioneering work of Van Potter in the 1960s, who proposed that hepatomas contain cells undergoing “blocked ontogeny” [66]. This idea was further elucidated for all types of cancers by Barry Pierce and Stewart Sell [67] who clarified that many functions thought to be related to cancer (e.g. AFP expression) are normal functions of an expanded stem/progenitor cell population and that identification of key distinctions must involve comparison of cancer cells to their normal stem cell [64, 68]. Indeed, normal stem/progenitor cells are strikingly similar to tumor cells in morphology, gene expression, and growth properties, and tumors can be identified as an expanded lineage stage [64, 69]. The clinical use of stem cells may come with an increased risk of tumors depending on the donors (e.g. if there are undiagnosed tumor cells among the endogenous stem cells) and on the patient’s medical condition (e.g. severe immunosuppression).

Strategies for cancer therapies will be revolutionized if revamped with lineage biology knowledge. Treatments with drugs or radiation are known to affect later lineage stages preferentially. If a specific treatment also targets the lineage stage(s) containing malignantly transformed cells, then the treatment can be curative. If they fail to target that stage, there will be a lethal rebound effect: the treatment kills cells in later lineage stages, mutes feedback loop signaling, and secondarily unhinges early lineage stages where malignant cells reside. Therefore, future cancer therapies should involve strategies identifying the lineage stage of the tumor and whether the treatment targets that stage or, alternatively, uses lineage mechanism regulation, such as feedback loop signals, to control the rate of growth of tumor cells.

3.4. CONCLUSIONS

The intrahepatic maturational lineages begin within the stem cell compartments, located periportally, and progress through the midacinar region and ending near the central vein. The parenchymal cells, along with their mesenchymal cell partners, are governed by gradients of paracrine signals, including sets of soluble factors and insoluble extracellular matrix components, and by specific mechanical forces. Feedback loop signals regulate the stem/progenitors, controlling liver mass and tissue regeneration. Understanding stem cell and lineage biology in the liver and their regulation offers new considerations for basic and industrial investigations and for more biologically rational clinical program strategies.

3.5. ONLINE SUPPLEMENT

While the review focuses on summarizing the literature regarding the earliest lineage stages that comprise the hepatic stem cells, hepatoblasts and committed progenitors, this online supplement provides additional information and references on what is known of normal cells. For information on the many studies on oval cells, cells that expand in hosts exposed to one or another oncogenic insult, or in progenitors occurring in disease states, we refer you to several excellent articles and reviews [70-77]. The supplement online figures (Figure 6 to Figure 13) also complement those used within the review (Figure 1 to Figure 5).

3.5.1. Ploidy

All tissues are organized with a stem cell niche containing stem cells and committed progenitors that give rise to daughter cells, maturing step-wise to adult cells, and transitioning to apoptotic cells [78]. The kinetics of the lineage and tissue turnover is tissue-specific and correlates inversely with the extent of polyploidy [79-82]. Rapidly regenerating tissues have lineages with fast kinetics and typically have only 5-10% polyploid cells [83].

Newly recognized lineages are those associated with quiescent tissues (e.g. liver, pancreas, lung, kidney), with turnovers estimated to be months to years [3]. The extent of polyploidy in these tissues in adults is from 20% to 95% [5].

Fetal and neonatal tissues are entirely diploid. The transition to an adult ploidy profile occurs within 3 weeks in mice; within 4 weeks in rats; and by late teenage years in humans [5]. The adult profile is also distinct in different species. Humans are mostly diploid and with the remainder being tetraploid. The livers of adult rats are only ~10% diploid, ~80% tetraploid, and ~10% octaploid. Mice have livers with cells that are only 5% diploid and 95% polyploid with the ploidy levels going from tetraploid to 32N. In all mammalian species the diploid cells are found periportally transitioning to polyploidy cells with progression towards the central vein.

With increasing age in all mammals, the percentage of diploid cells steadily declines. In humans, the percentage of diploid cells in liver decreases from over 70% in young adults to less than 50% in the elderly, a presumed variable in the age-dependent loss of regenerative capacity of the tissues [82].

3.5.2. Extrahepatic Lineages in the Biliary Tree

Multipotent stem cell populations have been identified recently in the peribiliary glands of the biliary tree, giving rise to liver, bile duct, and pancreas under specific culture conditions or with transplantation *in vivo* [16, 84]. The antigenic and biochemical profiles of the biliary tree stem cell populations at different sites in the extrahepatic bile ducts are suggestive of multiple lineage stages with the most primitive ones being within the hepato-pancreatic common duct near to the duodenum. Later stages are found in the cystic duct and hilum. Related cells, possibly transit amplifying cells, are found within the gallbladder that

does not have peribiliary glands. Further characterization of these cells should elucidate possible precursor-descendent relationships including if they are precursors to intrahepatic lineages. A review summarizing the extant knowledge of these newly discovered lineages is given elsewhere [85].

3.5.3. Comments on intrahepatic lineage stages

The zonal distribution of the liver's known heterogeneity of functions has been described extensively in the past. Below and in Table 1 and Table 2, we summarize these past studies on functions occurring preferentially in specific zones (periportal, midacinar, and pericentral) within the liver acinus.

Intrahepatic Lineage Stage 4. Periportal parenchymal cells (zone 1) are comprised of "small hepatocytes" and intrahepatic biliary epithelia, or "large cholangiocytes". The hepatocytes are ~18 μm and the large cholangiocytes are ~14 μm in diameter. The hepatocytes form plates or cords of cells bound on their lateral borders to each other by a mix of lateral matrix components (cell adhesion molecules, proteoglycans), tight junctions (cadherins), and gap junctions (connexins). The proteoglycans on the lateral borders are known to regulate multiple aspects of gap junction functions as well as to be essential for transcription (mRNA synthesis) of tissue-specific genes [86-88]. In the center of the lateral border of connection between two hepatocytes is the bile canaliculus, a region of undulating membrane studded with enzymes and pumps that transfer hepatocyte-derived products into bile in the canaliculus.

Hepatocytes are unique among epithelia in having two basal surfaces, the "top" and "bottom", that are bound to extracellular matrix components (collagens, proteoglycans, adhesion molecules) in the Space of Disse and produced by the hepatocytes and their

mesenchymal cell partners, endothelial cells. The periportal hepatocytes peak in the zone 1 metabolic activities (see Table 2 and Table 3). In brief, they produce factors and enzymes associated with gluconeogenesis, amino acid and ammonia metabolism, urea synthesis, and glutathione peroxidase [89-94].

Intrahepatic Lineage Stage 5. Midacinar hepatocytes (Zone 2) are diploid in humans, tetraploid in rats, and 4-8 N in mice, ~22-25 μm in diameter [5]. The past strategies for studying zonation of functions, selective destruction of periportal or pericentral cells with detergents followed by characterization of the surviving cell suspensions, are not able to give precise definition to the functions of zone 2 cells [95]. Recognition of some unique features of the midacinar parenchymal cells has emerged with immunohistochemical and in situ hybridization studies on sections of livers. The midacinar hepatocytes are the first stages to have peak levels of certain transcription factors regulating albumin enabling these cells to produce especially high levels of the protein [92, 93]. In addition, transferrin mRNA is expressed in earlier lineage stages, but it does not translate to protein at detectable levels until zone 2 (midacinar), correlating with production of specific elongation factors associated with translation of transferrin mRNA to protein [8]. It is unknown whether this is true for other proteins. There must be distinctions in posttranscriptional and translational regulation of certain mRNAs for early lineage stage cells versus later ones, an hypothesis yet to be fully explored.

Intrahepatic Lineage Stage 6. Pericentral diploid hepatocytes (zone 3) are found in small numbers in human livers, but in rats and mice there are none; they have only polyploid cells in zone 3. The diploid parenchymal cells in humans decline with age in parallel with an increase in polyploidy. In culture, they are able to undergo DNA synthesis but with limited, if

any, ability to undergo cytokinesis, and no capacity to be subculture [21]. In addition to albumin, tyrosine aminotransferase, and transferrin, they also strongly express a number of the P450s that handle xenobiotic metabolism (e.g. P450-3Aa), glutathione transferases, and UDP-glucuronyl-transferases [96, 97].

Intrahepatic Lineage Stage 7. Pericentral polyploid parenchymal cells (zone 3) in all species can undergo DNA synthesis but are unable to undergo cytokinesis [5]. In humans they are tetraploid; in rats they are octaploid; and in mice they are 16-32 N. They are much larger (>30 μm in diameter in humans and up to 75 μm in rodents) due to the hypertrophy associated with polyploidy. They express high levels of the late genes including the late P450s, glutathione transferases, UDP-glucuronyl-transferases, glutamine synthetase and heparin proteoglycans [63, 98]. These cells have never been observed to divide in culture or in bioreactors under all conditions tested and do not divide if transplanted *in vivo* into quiescent livers. However, if transplanted into hosts with very severe liver failure such as occurs in tyrosonemia or following death of most parenchymal cells due to a suicide transgene, murine tetraploid and octaploid hepatocytes have been shown capable of division [36, 37, 99]. This has been claimed evidence that all hepatocytes are stem cell-like [100]. The more likely interpretation is that these are examples of reprogramming phenomena in which demethylation events are occurring. Thus, it is not logical to imagine using such late lineage stage parenchymal cells for reconstitution of livers in most forms of liver cell therapies.

Intrahepatic Lineage Stage 8. Apoptotic cells are found in highest numbers near the central vein. It is also the site for high numbers of macrophages, long known to be involved in apoptosis. The macrophages secrete tumor necrosis factor (TNF), triggering apoptosis

through the Fas ligand binding to the Fas receptor, and activating caspases, a family of proteins mediating apoptosis through multiple targets that include poly-ADP ribose polymerase, nuclear lamins, and DNA fragmentation factor [63, 101-105].

Table 2. Zonal Distribution of Cellular Subpopulations. Table 2 and Table 3 have been prepared from data in reviews on heterogeneity of functions in liver by Gebhardt [106] (see Figure 3, Figure 4, Table 2 and Table 3) and by Jungermann and Kietzmann [95] (see Figure 2, Figure 3, Table 2 and Table 3) and from diverse, more recent studies [43, 46, 107, 108]. Nomenclature: ++++ = strong signal; + = weak signal ; -- = no signal.

Cellular Subpopulations	Stem Cell Niche[9]	Zone 1	Zone 2	Zone 3
Parenchymal Cell Populations				
Hepatic stem cells (HpSCs)	++	-	-	-
Hepatoblasts (HBs)	++	-	-	-
Committed progenitors (small cholangiocytes, hepatocytic progenitors	++	-	-	-
Hepatocytes	-	+++	+++	+++
Cholangiocytes (large cholangiocytes; later lineage stages of biliary cells are extrahepatic)	-	+++	-	-
Mesenchymal/Endothelial Cell populations				
Angioblasts (CD117+, CD133+, CD31-)	++ (with HpSCs)	-	-	-
Endothelial cell precursors (CD133+, CD31+)	++ (with HBs)	++ (with committed hepatocytic progenitors)	-	-
Endothelia cells (few, large fenestrations)	-	++	+	-
Endothelia cells (numerous, small fenestrations)	-	-	++	+++
Hepatic stellate cell (HpSTC) precursors (CD146+, ASMA+, vitamin A ±, GFAP-)	++ (with HpSCs and hHBs)	-	-	-
Hepatic stellate cells (CD146++, ASMA++, Vitamin A++, GFAP +)	+ (with committed biliary progenitors or small cholangiocytes)	+++ (with large cholangiocytes)	+/- (+ in disease states)	- (+ in disease states)
Stromal cells	-	++ (most are part of extrahepatic biliary tissue)	-	-
Hemopoietic Cells				
Hemopoietic progenitors (CD34+)	++	-	-	-

[9] Stem cell niche: ductal plates (also called limiting plates) in fetal and neonatal livers; canals of Hering in pediatric and adult livers.

Kupffer Cells (monocytes)	-	++ (phagocytosis)	++	+++ (cytotoxicity)
Lymphocytes	-	++	++	++
Pit cells (liver natural killer cells)	-	++	++	++

Table 3. Intrahepatic Zonation of Functions. Table 2 and Table 3 have been prepared from data in reviews on heterogeneity of functions in liver by Gebhardt [106] (see Figure 3, Figure 4, Table 2 and Table 3) and by Jungermann and Kietzmann [95] (see Figure 2, Figure 3, Table 2 and Table 3) and from diverse, more recent studies [43, 46, 107, 108]. Nomenclature: ++++ = strong signal; + = weak signal ; -- = no signal.

	Protein or Activity/ mRNA[10]	Zone 1 Periportal	Zone 2 Mid-Acinar	Zone 3 Perivenous
Carbohydrate Metabolism				
Phosphoenolpyruvate carboxykinase (glycogen from pyruvate)	Protein	+++		+
	mRNA	++++		+
Fructose-1,6-bisphospatase	Protein	+		+
	mRNA	+++		+
Gluconeogenesis (from lactate, amino acids)		+++		+
Gluconeogenesis (from pyruvate)		+++		+
Glycogen Synthesis (from lactate)		+++		++
Glycogen Synthesis (from glucose)		++		+++
Pyruvate kinase Type L		+		+++
Glycolysis (glucose to pyruvate)			--	+++
Glucokinase (glycogen from glucose)	Protein	+		++
	mRNA	+		+
Amino Acid and Ammonia Metabolism				
Tyrosine aminotransferase		++	+	+
Serine dehydratase		+++		+
Glutamine synthetase (glutamine from ammonia; also from glutamate, α-oxoglutarate, ornithine)		--		+++
Ureogenesis (from ammonia, amino acid nitrogen via carbamoyl phosphate synthetase)		+++		+
Lipid Metabolism				
HMG-CoA reductase	Protein	+++		--
	mRNA	++		--
β-Oxidation		+++		+
Liponeogenesis Ketogenesis		+		+++
Cholestrol Biosynthesis		+++	--	--
Bile Acid Synthesis		--	+	++

[10] Information in this column is given only when expression of the mRNA and the protein are distinct (e.g. mRNA is found, but not protein); if nothing is listed, then it means that both mRNA and protein were found.

Sulfation		+++		+
Glucuronidation		+		+++
Glutathione Content		+++		+
Glutathione-S-Transferases		+		+++
Glutathione Peroxidase		+++		+
Bile Acid Uptake	Na^+ dependent	+++	+	--
	Na^+ independ.	++		++
Uptake of many organic anions and cations in presence (with) or absence (without) of albumin	without	++	+	--
	with	++		++
Oxidative Energy Metabolism				
Succinate dehydrogenase		++		--
O_2 uptake		++++		++
Mixed Function oxidation (NADPH cytochrome c reductase, epoxide hydrolase)		--	++	++++
Cytochrome P450 Isozymes				
Cyp 3A7		+++		-
CYP 1A, IIA, IIB, IIE, 3[a]		-	++	++++
Specific Proteins				
Transferrin	Protein	+/-	++	+++
	mRNA	+++	+++	+++
ICAM-1 (HBs, sinusoidal endothelia and parenchyma associated with them)		++	+++	++++
NCAM (only HpSCs)		++ ***(niche)***	-	--
EpCAM *(HpSCs, HBs, intrahepatic cholangiocytes*		+++ ***(niche)***	-	-
α-Fetoprotein (only HBs)		++ ***(niche)***		--
Albumin		++	++++ (full transcriptional regulation)	
Connexin 26		+++		+
Connexin 32		+		+++
Extracellular Matrix Components				
FIbronectin (tissue)		++	++	++
Fibronectin (plasma)		--		++++
Collagen I		+	+	+
Collagen III		++	++	++
Collagen IV		++++	++	++
Collagen V		++++	++	?
Collagen VI		++++	++	++
Collagen XVIII		++	++	++
Laminin		++++		--
Hyaluronans (produced by hHpSTCs and endothelia)		++++		---
Chondroitin sulfate-PGs		++++	++	+
Heparan sulfate-PGs		+	++	+++
Heparin-PG		-	-	+++
Dermatan sulfate-PGs		++	+	+

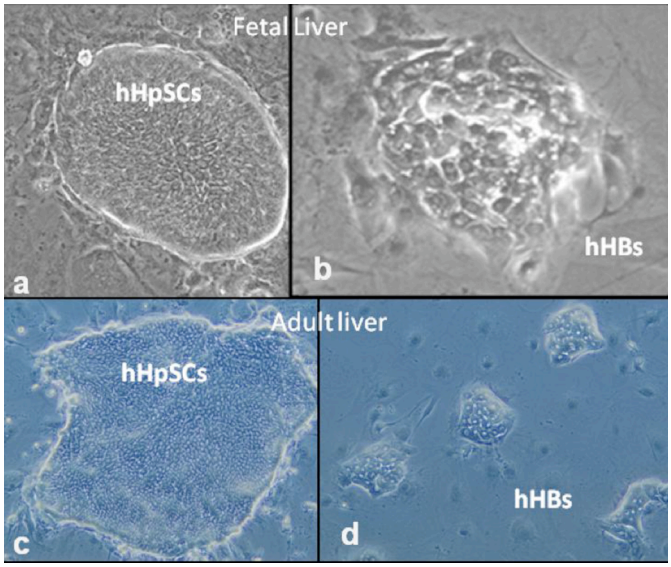

Figure 6. Phase micrographs of colonies of hHpSCs and hHBs from fetal versus adult human livers. The cultures are on culture plastic and in serum-free Kubota's Medium. Originally published in J Exp Med, DOI:10.1084/jem.20061603 [12][11].

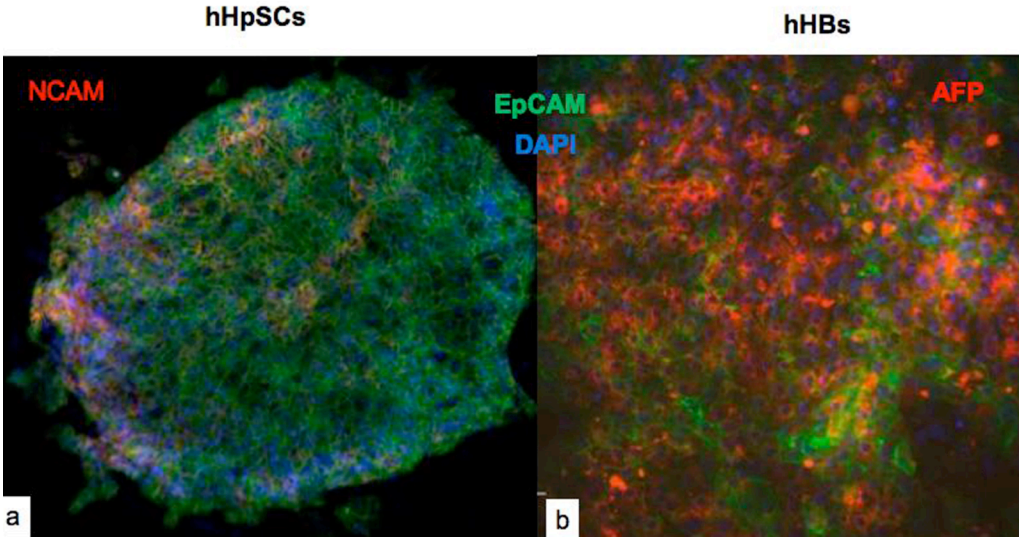

Figure 7. Cultures of hHpSCs (a) and hHBs (b) that were assayed for expression of EpCAM (green) and for NCAM (red in hHpSCs) and AFP (red in hBs). The nuclei in all of the cells are blue from staining with DAPI. Originally published in Hepatology, 2010;52: 1443-1454 [16][12].

[11] ©Schmelzer E, Zhang L, Bruce A, Wauthier E, Ludlow J, Yao HL, et al. Originally published in *J Exp Med*. 204:1973-87. doi:10.1084/jem.20061603

[12] ©John Wiley and Sons. Wang Y, Yao H-L, Cui C-B, Wauthier E, Barbier C, Costello MJ, et al. Paracrine signals from mesenchymal cell populations govern the expansion and differentiation of human hepatic stem cells to adult liver fates. *Hepatology*. 2010; 52:1443-54

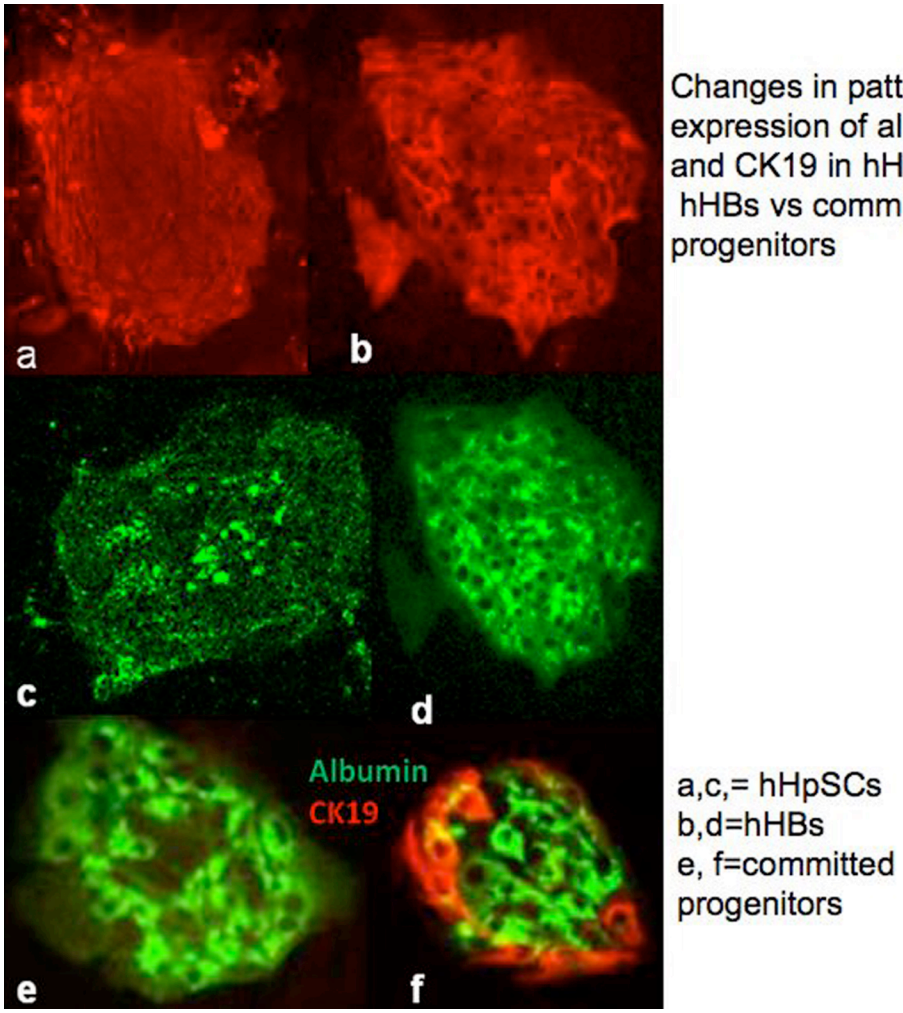

Figure 8. Immunohistochemistry demonstrating the change in expression of cytokeratin 19 (red) and of albumin (green) in hHpSCS versus hHBs versus committed progenitors. Note that CK19 is punctuate in hHpSCs and filamentous in hHBs and committed progenitors. Albumin is particulate in hHpSCS but transitions into the classic albumin aggregates found in all later lineage stages of parenchymal cells from hHBs to mature hepatocytes. Originally published in J Exp Med, DOI:10.1084/jem.20061603 [12][13].

[13] ©Schmelzer E, Zhang L, Bruce A, Wauthier E, Ludlow J, Yao HL, et al. Originally published in *J Exp Med*. 204:1973-87. doi:10.1084/jem.20061603

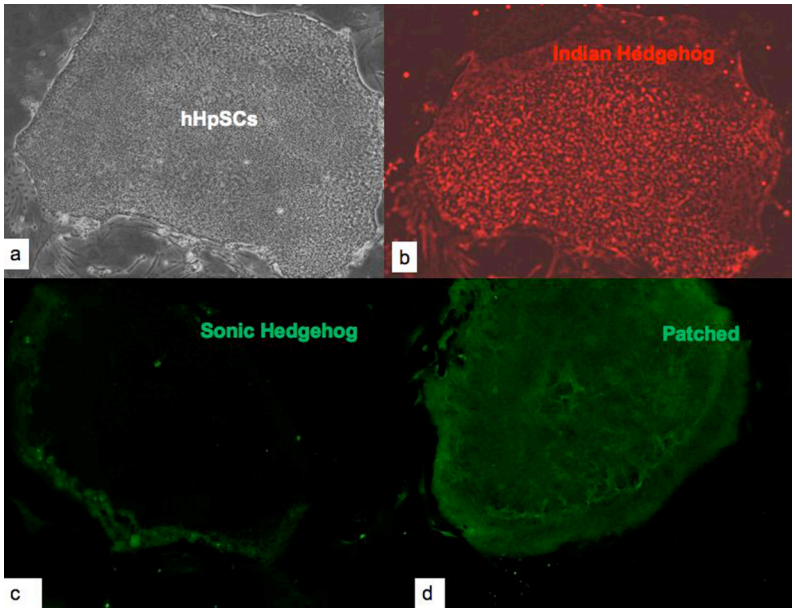

Figure 9. Phase microscopy of a colony of hHpSCs (a). The colony was then assessed for Indian Hedgehog (red) (b), sonic Hedgehog (c) that is found at the edges of the colony, and patched (d) that is the Hedgehog receptor and found throughout the colony. Originally published in Amer J Physiol Gast Liver Physiol 2005; 290: G859–G870 [9][14].

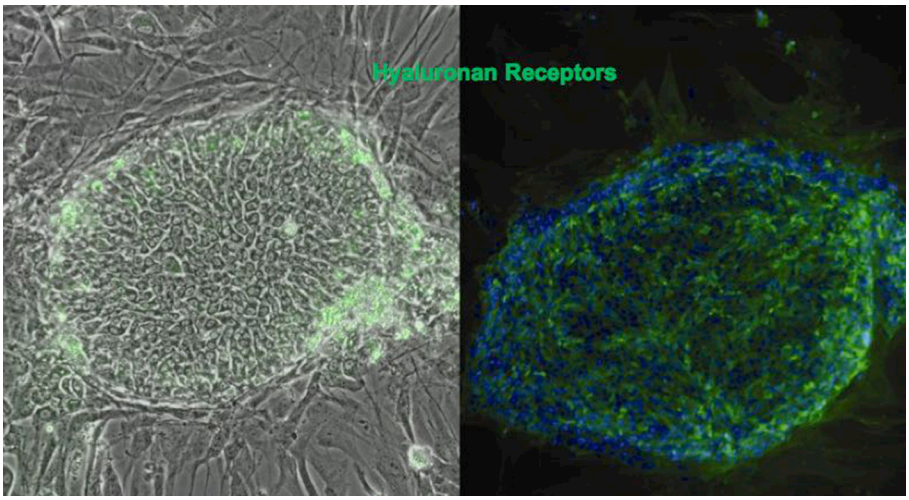

Figure 10. Immunohistochemistry demonstrating expression of hyaluronan receptors. Originally published in J Biomed Mater Res B Appl Biomater 2007; 82: 156-168 [26][15].

[14] Sicklick JK, Li YX, Melhem A, Schmelzer E, Zdanowicz M, Huang J, et al. *Am J Physiol Gastrointest Liver Physiol.* 2006. Hedgehog signaling maintains resident hepatic progenitors throughout life. 290(5):G859-70. doi:10.1152/ajpgi.00456.2005.

[15] ©John Wiley and Sons. Turner WS, Schmelzer E, McClelland R, Wauthier E, Chen W, Reid LM. Human hepatoblast phenotype maintained by hyaluronan hydrogels. *J Biomed Mater Res B Appl Biomater*. 2007; 82:156-68

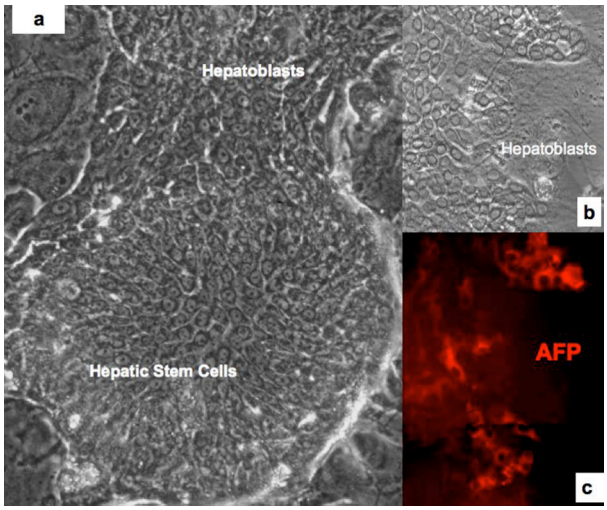

Figure 11. Lineage restriction of hHpSCs to hHBs after plating on a feeder layer that contributes paracrine signals inducing differentiation. Phase microscopy of both hHpSCs and hHBs. (b) magnified image of the edge of the colony at which hHBs are located; (c) immunohistochemistry of the cells in (b) assessing expression of alpha-fetoprotein (AFP).

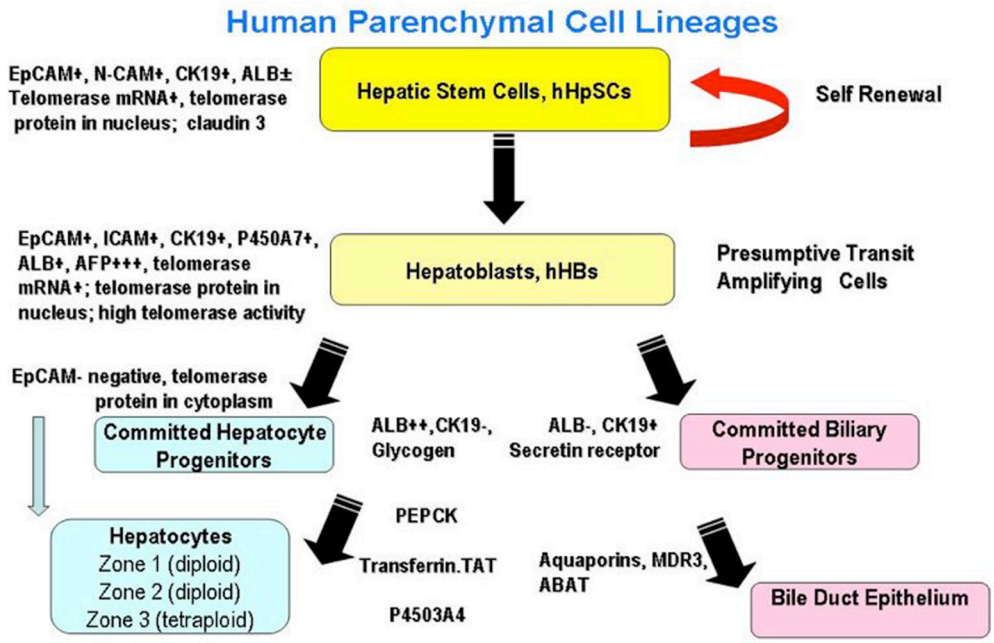

Figure 12. Schematic illustration of the parenchymal cell lineages and noting some of the changes in gene expression with maturation to either hepatocytes or cholangiocytes. Originally published in Hepatology 2010; 52: 1443-1454 [16][16].

[16] ©John Wiley and Sons. Wang Y, Yao H-L, Cui C-B, Wauthier E, Barbier C, Costello MJ, et al. Paracrine signals from mesenchymal cell populations govern the expansion and differentiation of human hepatic stem cells to adult liver fates. *Hepatology*. 2010; 52:1443-54

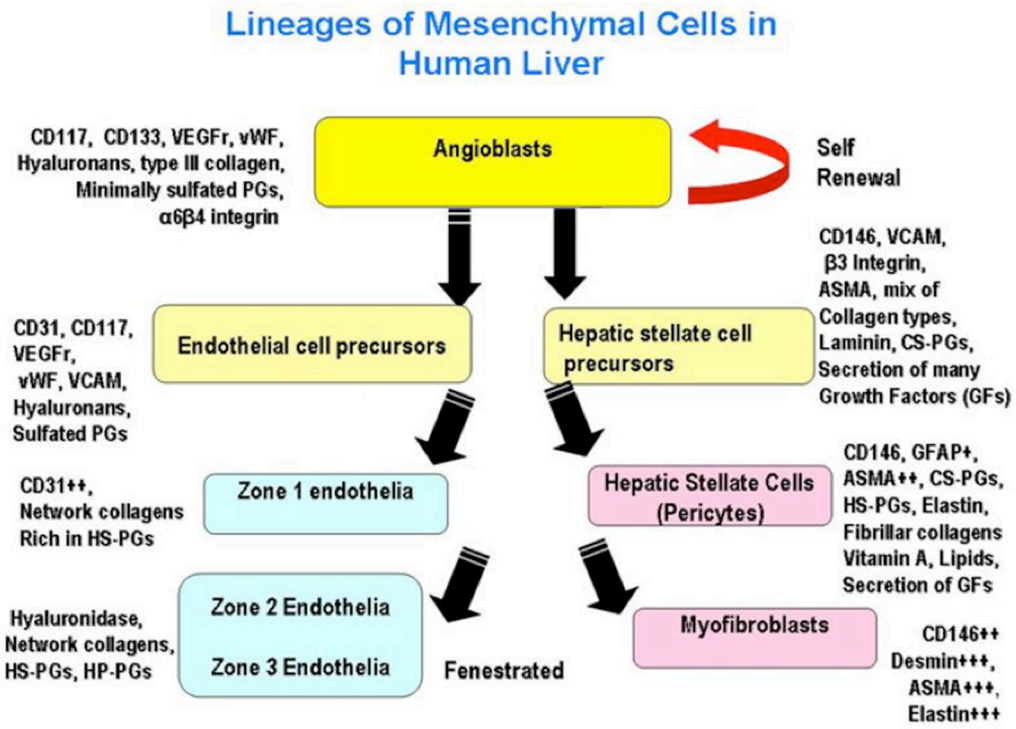

Figure 13. Schematic illustration of the mesenchymal cell lineages and noting some of the changes in gene expression as they mature to either endothelia or stromal cells. Originally published in Hepatology 2010; 52:1443-1454 [16][17].

[17] ©John Wiley and Sons. Wang Y, Yao H-L, Cui C-B, Wauthier E, Barbier C, Costello MJ, et al. Paracrine signals from mesenchymal cell populations govern the expansion and differentiation of human hepatic stem cells to adult liver fates. *Hepatology*. 2010; 52:1443-54

CHAPTER 4. PHYSICAL SIGNALING AND PRINCIPLES OF MECHANOTRANSDUCTION: TRANSITIONING FROM MECHANICAL FORCES TO CELL BEHAVIOR

The mechanical context of tissue function dictates the mechanical forces cells experience within tissues. Cells obey a "principle of compliance" in which they adapt their individual function to their environment, but cells also adapt their environment dynamically to function collectively as a tissue. Mechanotransduction signaling pathways that operate in specific cell types depend on mechanical contexts in tissues and are a footprint of cell adaptation to their tissue environment. Cells experience diverse mechanical stimuli with a collection of distinct mechanosensory libraries and assemble them into modules of mechanotransduction to comply with changing physical conditions. In essence, by creating multiple modules that respond to mechanical forces, cells can combine them to address multiple modalities that involve mechanical induction [109, 110].

In general, mechanotransduction mechanisms obey the "function follows form" principle because these mechanisms operate via intracellular structures with mechanical function that determine the physical integrity of the cell. Transducing forces into signaling cascades and cellular activity involves focal and cell-cell adhesions, cytoskeletal and actomyosin networks, ion-exchange channels and transmembrane receptors to ECM molecules. Cells transmit physical cues to the nucleus through these structures and convert them to post-transcriptional processes that cellular machinery can interpret, inducing multiple

cellular mechanisms. Some recognized mechanisms with mechanical features include cell shape changes, migration, ciliary beating, cell cortex tension, cell adhesion to ECM molecules, motor protein trafficking, flagellar motility and cellular spreading [111].

There are particular features that make mechanotransduction radically different from the more widely studied ligand-receptor signaling. All signaling depends explicitly on transport. Autocrine and paracrine ligand-receptor signaling is limited in time and space by the physics of diffusion, whereas mechanical forces can propagate – and consequently induce cellular activity – across much larger scales, quickly. In addition, physical contact between cells and their surroundings implies that complex cellular phenomena without obvious mechanical participants, such as differentiation and intercellular signaling, occur under characteristic physical conditions. These features of mechanotransduction have radical implications in understanding cellular development and stem cell biology [112].

A biological consequence of mechanotransduction is cell differentiation, which arises in maturational tissue gradients within evolving ECM compositions and signaling gradients. However, cell differentiation also takes place when evolving mechanical properties of the ECM transmit forces differently to the cells as the ECM changes mechanically. Mechanical properties of tissues are different across distinct locations in maturational gradients, in which ECM compositions vary by distributing glycoproteins, collagens or degrees of PG sulfation heterogeneously across tissues [1, 107, 113-115].

Mechanotransduction operates in all tissues, including soft organs like liver. We hypothesize that the adult liver, with heterogeneous but well organized composition, responds to mechanical stimuli differentially across the maturational gradient. Within this gradient, the effects of mechanical forces on differentiation vary as cells across hepatic

lineages adapt to their microenvironment, and correlate with the progression in the hepatic ECM profile. In agreement with this notion, the hypothesis which drives our experimental approach is that local mechanical properties of the ECM are not only a consequence of lineage-dependent specification within the hepatic maturational gradient, but also a driving stimulus to differentiation.

CHAPTER 5. MECHANICAL STIFFNESS OF THE MICROENVIRONMENT REGULATES PHENOTYPE OF HUMAN HEPATIC STEM CELLS[18]

5.1. ABSTRACT

Human livers are comprised of maturational lineages of parenchymal and mesenchymal cells beginning in stem cell niches, the canals of Hering, and ending in polyploid cells at the central vein. The stem cell niche contains hepatic stem cells (hHpSCs) in partnership with angioblasts embedded in a microenvironment of soluble signals and matrix components that includes hyaluronan (HA). In our work, we investigated whether matrix mechanics dictates differentiation in hHpSCs by surveying changes in their phenotype and hepatic functions when cultured in three-dimensional (3D) environments with known mechanical properties. We mimicked the stem cell niche by embedding isolated hHpSCs in 3D HA hydrogels prepared with Kubota's Medium (KM), cross-linked with poly(ethylene glycol)-bis-acrylate (PEGDA) and containing soluble signals tailored for hepatic stem cells. It provided cell attachment, matched diffusion properties of cell suspensions, possessed shear thinning properties, showed a perfectly elastic response to mechanical loading, and exhibited predictable mechanical stiffness (shear modulus |G*|) depending on HA and PEGDA concentrations. Increased stiffness/rigidity controlled hHpSC expansion and induced differentiation to an intermediate state between hHpSCs and the next maturational stage,

[18] Lozoya OA, Wauthier E, Turner RA, Barbier C, Guilak F, Superfine R, Reid LM. Mechanical stiffness of the microenvironment regulates phenotype of human hepatic stem cells. Article, in preparation for submission to peer-reviewed journal, appears as this chapter with authors' permission.

hepatoblasts (hHBs). The mRNA and protein expression levels of differentiation markers, such as alpha-fetoprotein (AFP) and E-cadherin (CDH1), decreased with increasing hydrogel rigidity below an apparent stiffness bifurcation region around |G*| = 200 Pa. Matrix rigidity proved a significant regulatory variable even within the stem cell niche microenvironment. To our knowledge, this is the first study of its kind on a determined stem cell population with endodermal origin.

5.2. INTRODUCTION

The liver is one of the most complex organs in the body and is responsible for toxin removal, production of bile and hormones, regulation of nutrients, and the synthesis of serum proteins [116]. After acute injury, liver can regenerate rapidly within a few weeks [63]. However, for patients in severe conditions resulting in liver failure, organ transplantation is the only established treatment. Some alternative therapeutic strategies under development include transplantation of liver cells in patients, bioartificial livers as assist devices and cell grafting [65]. Grafting technologies use a 3-dimensional (3D) microenvironment that mimicks paracrine signaling between epithelial and mesenchymal cells in liver and contains mixes of extracellular matrix (ECM) components that bind specific soluble signals. We pursue forms of liver cell therapies that use purified hepatic stem cells (hHpSCs) transplanted by grafting technologies. Cell grafting helps hHpSCs localize to the target tissue, expand and differentiate to adult fates, and facilitates graft vascularization [65].

Liver is organized in functional unit (acini) hosting all hepatic maturational lineages. In histological sections, acini have hexagonal shape and six sets of portal triads at the vertices, each containing a hepatic artery, portal vein and bile duct. A central vein connected to the vena cava occupies the center of each acinus. By convention, three zones delineate liver

acini: zone 1 is periportal; zone 2 is midacinar; and zone 3 is pericentral [117]. Changes in matrix chemistry are concomitant with progression of cell maturity within liver zones. The hepatic stem cell niche, located in the periportal zone 1 contains HAs, laminin forms that bind to α6β4 integrin, type III collagen, unique forms of minimally sulfated chondroitin sulfate proteoglycans (CS-PGs), limited amounts of type IV collagen and no type I collagen. This matrix composition permits a few stable interactions of growth factors with hHpSCs. It transitions to different matrix chemistry in the pericentral zone 3, containing type 1 collagen, fibronectin, and unique forms of heparin proteoglycans (HP-PGs) [118-121]. As cells emerge from the niche and into the hHB-associated matrix, they encounter type IV collagen, laminin, and more highly sulfated forms of CS-PGs that stabilize continuous binding of growth factors. These proteoglycan/growth factor complexes are critical to dictate differentiation of cells towards adult fates [122].

Successful cell expansion *ex vivo* requires cultures mimicking paracrine signals from the original epithelial-mesenchymal relationship in tissues, where soluble and insoluble signals bound to the lateral and basal forms of ECM mediate dynamic interactions between epithelium and mesenchyme [12, 16, 93, 122-125]. However, the role of the mechanical properties of the ECM environment remains undefined. This aspect is relevant to tissue engineering: if intrahepatic differentiation is also a response to mechanical induction, then we can regulate maturation of hepatic progenitors within hydrogels by controlling culture conditions *ex vivo* at the macroscopic level before *in vivo* engraftment.

We assessed the effects of mechanical properties of HA hydrogels with diverse concentrations of HA and PEGDA on embedded hHpSCs cultured in a serum-free medium. Our work defines a method to prime hHpSC differentiation in static cultures that uses a

single mechanical input – the mechanical properties of the 3D environment. Our method also defines a culture model that is predictable and repeatable in experimental conditions.

5.3. MATERIALS AND METHODS

Sourcing and processing of human livers. Human fetal liver tissue was provided by an accredited agency (Advanced Biological Resources, San Francisco, CA) from fetuses between 16-20 weeks gestational age obtained by elective terminations of pregnancy. The research protocol was reviewed and approved by the IRB for Human Research Studies at the UNC. The processing of the tissue was done as described previously [12, 16, 21].

Kubota's Medium (KM). KM consists of any basal medium, here being RPMI 1640 (Gibco /Invitrogen, Carlsbad, CA), with no copper, low calcium below 0.5 mM (here being 0.3 mM), trace elements (zinc--10-12M and selenium—10-9M), insulin (5 μg/ml), transferrin/fe (5 μg/ml), high density lipoprotein (10 μg/ml) and a mixture of free fatty acids bound to bovine serum albumin. Detailed methods for its preparation are given in a methods review [21].

Hyaluronans (HA) and their cross-linker, PEGDA. All HA materials were obtained from a commercial source, Glycosan Biosciences (Salt Lake City, Utah) and consist of thiol-modified carboxymethyl HA (or CMHA-S), a chemically modified HA derivative with disulfide bridges for cross-linking by an oxidative reaction into hydrogels using poly(ethylene glycol)-bis-acrylate (or PEGDA) as cross-linking catalyst. The level of cross-linking activity and stiffness of the hydrogel can be regulated by the amounts of CMHA-S and PEGDA added [126-130]. Specific concentrations of CMHA-S and PEGDA dry reagents were mixed separately in KM at pH 7.4 at a specific concentration of CMHA-S and of PEGDA, and were warmed for 30 minutes at 37°C to enhance dissolution of dry reagents

(as instructed by manufacturer). Separate formulations of mixtures of CMHA-S and PEGDA were prepared as summarized in Table 4.

Table 4. Formulations used in mechanical characterization experiments for KM-HA hydrogels in terms of their pre-mix CMHA-S and PEGDA solutions. Final KM-HA hydrogel composition for each formulation was achieved by mixing the CMHA-S and PEGDA solutions at a 4:1 ratio. All KM-HA hydrogel formulations shown were used in diffusion coefficient measurements; only lettered formulations (A, B, C, D, E, F) were used for rheometry and seeding of hHpSC colonies.

Final contents (4:1 apportionment)		**PEGDA initial solution content (1 part)**			
		2.0% (w/v)	**4.0% (w/v)**	**6.0% (w/v)**	**8.0% (w/v)**
CMHA-S initial solution content (4 parts)	**1.0% (w/v)**	***Formulation A*** CMHA-S 0.8% (w/v) PEGDA 0.4% (w/v)	CMHA-S 0.8% (w/v) PEGDA 0.8% (w/v)	CMHA-S 0.8% (w/v) PEGDA 1.2% (w/v)	***Formulation B*** CMHA-S 0.8% (w/v) PEGDA 1.6% (w/v)
	1.5% (w/v)	CMHA-S 1.2% (w/v) PEGDA 0.4% (w/v)	***Formulation C*** CMHA-S 1.2% (w/v) PEGDA 0.8% (w/v)	***Formulation D*** CMHA-S 1.2% (w/v) PEGDA 1.2% (w/v)	CMHA-S 1.2% (w/v) PEGDA 1.6% (w/v)
	2.0% (w/v)	***Formulation E*** CMHA-S 1.6% (w/v) PEGDA 0.4% (w/v)	CMHA-S 1.6% (w/v) PEGDA 0.8% (w/v)	CMHA-S 1.6% (w/v) PEGDA 1.2% (w/v)	***Formulation F*** CMHA-S 1.6% (w/v) PEGDA 1.6% (w/v)

HA hydrogel rheometry. Multiple hydrogel formulations, prepared as indicated above, were immediately homogenized by vortexing and delivered as liquids within less than 10 minutes post-mix in individual 9.5 mm x 6.2 mm sterile cloning cylinders (Cole-Parmer) placed inside individual wells as casts in a multi-well plate (500 µl of HA hydrogel per sample, 4 samples per tested formulation). Maximum hydrogel cross-linking occurred without additional media for 1 hour under sterile conditions in an incubator at 5% CO2/air mix and 37°C. Afterwards, hydrogels were supplied with 2.5 ml of HK media and incubated overnight prior to testing.

Rheological properties of cell-free HA hydrogels were measured at the Center for Computer Integrated Systems for Microscopy and Manipulation (CISMM) at UNC Chapel

Hill. The testing system made use of an AR-G2 stress- and temperature-controlled rheometer (TA Instruments, oscillation torque and velocity tolerances: 1% and 5%, respectively; temperature tolerance: 0.2°C) with a cone-and-plate (CAP) geometry setup at a constant 26-μm cone-to-plate truncation gap, a 40-mm diameter 1° angle stainless steel cone, a Peltier plate equilibrated at 37°C and equipped with a H_2O-filled solvent trap (minimum required sample volume: approximately 300 μl per individual sample). HA hydrogel is loaded for testing by uniform cone-and-plate compression down to the truncation gap distance, ensuring full contact with the cone surface area, and with system locked until normal pre-stress response from the compressed HA hydrogel sample equilibrates. The testing system uses negative feedback controls to equilibrate sample pre-stress before tests and maintain equilibrated sample pre-stress in real time throughout tests. The testing system software accounts for compressive pre-stress in samples when calculating shear responses from measurements. After HA hydrogel setup, a frequency sweep test was performed with an oscillatory shear stress amplitude of 0.6 Pa and forcing frequencies ranging from 0.01 Hz to 100 Hz (increasing logarithmic frequency ramp mode at 10 points per decade with 3 seconds of stress conditioning and 3 seconds of sampling under controlled flow). Data were recorded separately for each individual sample, and experimental variables were calculated directly from measurements using post-processing tools from the testing system software, including regression analysis routines for rheological constitutive models [131].

Diffusivity assays. Multiple hydrogel formulations, prepared as indicated above, were immediately homogenized by vortexing and a single 200-μl volume was delivered as a liquid inside an individual well in a 24-well plate for each formulation (sample thickness: ~ 1 mm) within less than 10 minutes post-mix. HA hydrogels were incubated without additional

media for 1 hour under sterile conditions in an incubator at 5% CO_2/air mix and 37°C to allow maximum cross-linking after mixing. Samples were then supplemented with equal volumes (200 μl) of additional KM supplied with 2.5 mg/ml (0.036 mM) fluorescein-conjugated 70-kDa Dextran molecules (D70, Invitrogen), allowed to diffuse into samples during overnight incubation by swelling prior to testing.

Diffusion coefficients of HA hydrogels were measured using a fluorescence recovery after photobleaching (FRAP) system in the Orthopaedic Bioengineering Laboratory at the Duke University School of Medicine. "In-well" testing was performed on samples after equilibration to room temperature for imaging purposes without prior aspiration of D70-supplemented KM. FRAP was performed with a laser scanning confocal microscope (Zeiss LSM 510) using an effective 20x amplification objective (10x/0.3 NA Plan-Neofluor air lens objective with additional 2x scanning control zoom). A total of 5 individual 30-second photobleaching spots (13.5-mW 458/488 nm excitation Argon laser, bleached geometry: 35-um diameter circle) were tested per sample, and a single unidirectional scan pre-bleaching image, a single unidirectional scan image immediately after the end of photobleaching, and 28 unidirectional scan time-series images at 4.0-second delay intervals afterwards (256 x 256 pixels frame size, 0.9 um/pixel resolution) were acquired for post-processing through a single channel (LP 505 nm, green emission channel). A fiducial mark at the bottom of an unused well was used as height reference datum and imaging data were recorded separately for each individual sample at a distance into the bulk of the hydrogel of 400 μm from the reference datum. Diffusion coefficients were calculated for all samples with curve-fitting analysis post-processing routines [132] of fractional fluorescence recovery of the bleached region,

measured by spatial Fourier transformation decay of normalized images, plotted against the frequency-scaled time.

Culture selection for hHpSCs and seeding of HA hydrogels. Freshly processed human fetal livers were cultured in serum-free KM in an incubator at 5% CO_2/air mix and 37°C to allow for culture selection of hHpSCs during 3 weeks, yielding colonies each containing approximately 2,000 – 5,000 cells per colony. The hHpSC colonies were isolated by pipette aspiration from culture plates and resuspended again in serum-free KM. The collected hHpSC colonies were pelleted by slow centrifugation and resuspended in pre-mix PEGDA solutions (Table 4) immediately after supernatant aspiration. PEGDA solutions with resuspended hHpSC colonies were then homogenized by vortexing with separate CMHA-S solutions. Samples consisted of 0.15-ml volumes of HA hydrogels with a seeding density of 80 hHpSC colonies/ml (100 hHpSC colonies per 1.25 ml) of HA hydrogel, delivered as liquids immediately after hydrogel mixing into 10-mm diameter 0.4-μm polycarbonate membrane tissue inserts (Nunc) and placed in individual wells of a 24-well culture plate. Samples were incubated without additional media for 1 hour under sterile conditions in a 5% CO_2/air mix and 37°C incubator to allow maximum cross-linking after mixing (sample thickness: ~ 2 mm). Samples were then supplemented with 1 ml of KM each and allowed to swell with media in culture for 24 hours, which also allows hHpSC colonies to adapt to their new 3D environment within HA hydrogels. Medium was replaced daily during the length of the experiment (1 week).

Viability assays. Viability was assessed using alamarBlue® (AbD Serotec, Kidlington, UK), an indicator of enzymatic reduction activities, by measurements of absorbance at 530 nm and 600 nm with a cytofluor Spectramax 250 multi-well plate reader (Molecular Devices,

Sunnyvale, CA). The cultures of hHpSCs in the HA hydrogels (4 samples per formulation, 0.15 ml sample volume) were incubated for 1 week in serum-free KM. Samples were supplemented with 10% volume of alamarBlue® reagent (AbD Serotec) every other day starting on day 2 post-seeding, collected after a 24-hour incubation period and stored at 4°C in the dark under sterile conditions until testing.

Quantitative Real Time PCR (qRT-PCR) analyses. Total RNA from monolayer cultures (positive control cell lines, hHpSC colonies) and freshly isolated hHBs was extracted with the RNeasy Mini Plus kit (QIAGEN); total RNA from 3D cultures in HA hydrogels was extracted using TRI Reagent (Invitrogen). Gene-specific primers (Table 5) were validated using cDNA templates generated from relevant cell lines expressing each gene of interest. Gene expression baselines were defined using cDNA templates generated from hHBs and 2-dimensionally grown hHpSCs colonies obtained from 3 different fetal livers. The hHBs were isolated from initial fetal liver preparations and constituted ~99% of the parenchymal cell fraction [8, 12, 21, 133]. Colonies of hHpSCs were isolated by pipette aspiration from monolayer cultures 3 weeks after plating freshly isolated parenchymal cell fractions; the parenchymal cells of these colonies were essentially 100% hHpSCs [12, 16, 21]. Gene expression levels of hHpSCs in HA hydrogels were measured for 6 different hydrogel formulations (4 samples per formulation, 0.15 ml sample volume, seeding density: 80 colonies/ml HA hydrogel) with hHpSCs obtained from the same fetal liver source, incubated in parallel with daily medium changes of KM, collected after 1 week of culture and fully repeated for 2 different fetal livers. Quantitative Real Time PCR (qRT-PCR) measurements were performed with an Applied Biosystems® 7500 Real-Time PCR System available in the Functional Genomics Core Facility at UNC Chapel Hill for the following

genes: AFP, EpCAM, NCAM, E-cadherin (CDH1) and Hyaluronan Receptor CD44 (Table 5). All measurements of relative expression were normalized with respect to GAPDH by the absolute quantification method described elsewhere [134, 135].

Analysis of secreted protein production. Concentration levels of secreted AFP, albumin and urea in culture media were measured to determine hepatic functions of hHpSC in the different hydrogel formulations throughout 1 week of culture. Media supernatant was collected daily from samples of 6 different hydrogel formulations (4 samples per formulation, 0.15 ml sample volume, seeding density: 80 colonies/ml HA hydrogel) starting on day 2 post-seeding and stored frozen at -20°C until analyzed. Secretion of AFP was measured by enzyme-linked immunosorbent assays (ELISA) using human AFP ELISA kits (ALPCO Diagnostics, Salem, NH). Albumin production was measured by ELISA using human albumin ELISA quantitation sets (Bethyl Laboratories, Montgomery, TX). Urea production was analyzed using blood urea nitrogen colorimetric reagents (Bio-Quant Diagnostics, San Diego, CA). All assays were measured individually with a cytofluor Spectramax 250 multi-well plate reader (Molecular Devices, Sunnyvale, CA).

Histology and sectioning. Samples of hHpSC-seeded HA hydrogels in each of 6 different hydrogel formulations and cultured for a week (4 samples per formulation, 0.15 ml sample volume, seeding density: 80 colonies/ml HA hydrogel) were fixed for at least one hour with 4% buffered paraformaldehyde. Fixed samples were embedded in HistoGel™ specimen medium, with the resulting construct transferred into a cryomold and embedded in Tissue-Tek OCT compound (Sakura Finetechnical, Tokyo, Japan) for flash freezing. Samples were submitted to the Histology Research Core Facility at UNC Chapel Hill for serial cryosectioning at 15 μm – 20 μm section thickness. Thinner sections were not feasible

due to the hydrogel handling properties. Frozen sections were stored at -80°C until staining, at which time they were stabilized to room temperature before PBS washing at the beginning of immunochemistry protocols.

Table 5. Primer sequences used in gene expression assays for hHpSC differentiation.

Gene (NCBI ID)	Description	Primer Sequence (5' → 3')	NCBI Ref. Seq. (Accession)	Positive Control Cell Line
AFP	α-fetoprotein (hepatic-specific variant)	Forward: CCATGAAGTGGGTGGAATCAA Reverse: TCTGCAGTACATTGGTAAGAATCCA	NM_001134.1	Hep3B (hepatoblastoma)
CDH1	E-cadherin	Forward: TCACAGTCACTGACACCAACGA Reverse: GGCACCTGACCCTTGTACGT	NM_004360.3	
EPCAM	Epithelial cell adhesion molecule	Forward: GACTTTTGCCGCAGCTCAGGAAG Reverse: GCCAGCTTTGAGCAAATGACAGTATTTTG	NM_002354.1	
CD44	Hyaluronic acid receptor	Forward: TGCCGCTTTGCAGGTGTAT Reverse: GGCCTCCGTCCGAGAGA	NM_000610.3	MDA-MB-231 (metastatic breast adenocarcinoma)
NCAM	Neural cell adhesion molecule	Forward: GCGACCATCCACCTCAAAGT Reverse: CTCCGGAGGCTTCACAGGTA	NM_000615.5	SK-N-SH (neuroblastoma)
GAPDH	Glycerine aldehyde-3-phosphate dehydrogenase	Forward: AAGGTGAAGGTCGGAGTCAA Reverse: AATGAAGGGGTCATTGATGG	NM_002046.3	Endogenous housekeeping

Immunohistochemistry. Histological sections were washed with PBS, bordered using a PAP-PEN, and blocked with 1X PBS + 0.1% Triton + 10% goat serum. Primary antibodies

for hHpSC differentiation markers AFP, EpCAM, NCAM, E-cadherin (CDH1) and Hyaluronan Receptor CD44 (Table 6) were applied and incubated overnight at 4°C, followed by washing and incubation of fluorophore-conjugated secondary antibodies for 2 hours at room temperature. Once labeled, fluorescence mounting media supplemented with DAPI was applied. Slides were imaged using fluorescence or laser confocal microscopy. Established cancer cell lines were used as positive controls for primary antibody validation of differentiation markers using secondary antibody fluoroprobes. Primary antibody specificity was confirmed by negative staining in isotype controls with secondary antibody fluoroprobe incubation.

Table 6. Antibodies used in immunochemistry assays for hHpSC differentiation.

Marker	Description	Manufacturer (Cat. No.)	Source (Isotype/Emission)	Stock Concentration	Titer	Positive (Cell Line)
AFP (human)	α-fetoprotein	Santa Cruz Biotechnology®, Inc. (sc-8399)	mouse anti-human (IgG_{2A})	200 μg/ml	1:100	Hep3B
CDH1 (human)	E-cadherin	Abcam® Inc. (ab8993)	mouse anti-human (IgG_{2B})	1 mg/ml	1:100	
EPCAM (human)	Epithelial cell adhesion molecule	Lab Vision/Neomarkers (MS-181-P1)	mouse anti-human (IgG_1)	200 μg/ml	1:500	
CD44 (human)	Hyaluronan receptor	Abcam® Inc. (ab6124)	mouse anti-human (IgG_{2A})	100 μg/ml	1:100	MDA-MB-231
NCAM (human)	Neural cell adhesion molecule	BD Pharmingen™ (559043)	mouse anti-human (IgG_{2B})	1 mg/ml	1:500	SK-N-SH
IgG_{2A} (mouse)	Alexa Fluor® 488	Invitrogen™ Molecular Probes® (A21131)	goat anti-mouse (488 nm)	2 mg/ml	1:800	N/A
IgG_{2B} (mouse)	Alexa Fluor® 488	Invitrogen™ Molecular Probes® (A21141)	goat anti-mouse (488 nm)			
IgG_1 (mouse)	Alexa Fluor® 568	Invitrogen™ Molecular Probes® (A21124)	goat anti-mouse (568 nm)			
Nuclear stain	UltraCruz™ fluorescence mounting medium with DAPI	Santa Cruz Biotechnology®, Inc. (sc-24941)	N/A	1.5 μg/ml	N/A	

Fluorescence microscopy. Histological sections of hHpSC-seeded HA hydrogels stained with secondary antibody fluoroprobes were identified using fluorescence microscopy. Negative controls were used to normalize backgrounds and eliminate image acquisition noise. Microscopy equipment consisted of an Olympus IX70 Inverted Fluorescence Microscope equipped with a Hg/Xe arc lamp for epi-illumination and an Olympus DP72 Digital Camera controlled with cellSens™ Digital Imaging Software for image acquisition.

Laser confocal microscopy. Histological sections of hHpSC-seeded HA hydrogels stained with secondary antibody fluoroprobes were identified using laser confocal microscopy. Negative controls were used to normalize backgrounds and eliminate image acquisition noise. Microscopy equipment consisted of a Leica SP2 Laser Scanning Confocal Microscope equipped with a Hg/Xe arc lamp for epi-illumination, excitation lasers at wavelengths of 350/364 nm (UV), 488/476/488/514nm (blue Ar laser), 561 nm (green solid-state diode pump laser) and 633 nm (visible red HeNe laser). LCS Software was used for image acquisition and processing.

Statistical analysis. Mechanical characterization experiments were displayed within a 95% confidence interval per engineering practice conventions. Experimental quantitative data were displayed in a mean ± standard error format in charts or displayed within a 99% confidence interval in plots for side-to-side comparison (as indicated). Significance of gene expression levels (logarithmically transformed) with respect to both hHpSCs and hHBs (p-value: * < 0.05, ** < 0.01, *** < 0.001) was determined by two-tailed Student's t-test. For immunohistochemistry studies, marker expression was qualitatively assessed by fluorescence or laser confocal microscopy. All individual sample measurements were performed at least in duplicate.

Principal Component Analysis (PCA) of gene expression was performed on data from hHpSCs and hHBs for all markers. The data from each marker was logarithmically transformed, followed by mean-centering and scaling with respect to the standard deviation of its transformed data. The covariance matrix was computed and used to calculate 5 eigenvalues with corresponding eigenvectors describing the principal components of the phenotype changes in hHpSC –to-hHB differentiation. For overall gene expression analysis, principal component scores were calculated for the first two eigenvalues (PC1 and PC2) and projected onto a two-dimensional plane defined by their eigenvectors for all data, including KM-HA-grown hHpSCs. Significance of gene expression levels with respect to both hHpSCs and hHBs (p-value: * < 0.05, ** < 0.01, *** < 0.001) and across KM-Ha formulations was determined on PC scores by two-tailed Student's t-test.

5.4. RESULTS

5.4.1. Mechanical properties of cell-free HA hydrogels.

5.4.1.1. Rheological properties across diverse formulations of CMHA-S and PEGDA

All HA-based hydrogels in the proposed research were assembled from equivalent components mixed in different proportions (Table 4). Under these experimental conditions, any differences in the behavior of hHpSCs across diverse 3D culture formulations should result from differences in the mechanical properties and composition of the HA hydrogels. We used serum-free KM to assemble our hydrogels, since our culture hydrogels would require embedded hHpSCs to have access to nutrients in KM throughout the experiment. To indicate that our hydrogels are distinct from those described elsewhere [130], we will refer to them as KM-HA hydrogels.

Our data shows that stiffness, viscoelastic properties and viscosity of KM-HA hydrogels depend on CMHA-S and PEGDA content (Table 4). KM-HA hydrogels maintained a constant stiffness across a broad forcing frequency range while exhibiting a perfectly elastic behavior (Figure 14a) and exhibited shear thinning, as their viscosity decreased with increasing forcing frequency (Figure 14b). Most importantly, the contents of CMHA-S and PEGDA controlled the mechanical properties of KM-HA hydrogels predictably (Figure 15a).

5.4.1.2. Diffusion in KM-HA hydrogels

We measured diffusion in KM-HA hydrogels using fluorescence recovery after photobleaching (FRAP) technology. Our tests showed that the differences in diffusivity between KM-HA hydrogels and serum-free KM are negligible and statistically insignificant, with diffusion coefficients ranging between 8 and 10 $\mu m^2/s$ (Figure 15b).

5.4.2. Effects of stiffness of the KM-HA hydrogels implicate mechanical properties as critical for the regulation of the maturational lineage stage of hHpSCs

5.4.2.1. Size, morphology, viability and proliferation of KM-HA-grown hHpSCs

Colonies of hHpSCs resemble embryonic cell colonies in plastic cultures: they have a roughly round shape, are well delimited at their edges and host cells with small sizes. We lifted 2D-grown hHpSC colonies by pipetting and mixed them with KM-HA hydrogels. As they adapt to their new 3D environment, hHpSC colonies abandon their flat configurations and can either agglomerate to spheroid-like structures or fold into complex 3D structures (Figure 16a). After 1 week of culture, cell morphology becomes diverse and some cells enlarge to about 15 um in size, which is characteristic of hHBs. This occurs at different degrees in all KM-HA formulations, and can be observed by immunostaining with antibodies for cell surface markers for hHpSCs and hHBs like EpCAM, CD44 and CDH1 (Figure 16b

and Figure 16c). Viability, measured as metabolic efficiency by alamarBlue® reduction, is only enriched for certain KM-HA hydrogel formulations after 1 week of culture (Figure 16d), even though nuclei shape does not suggest cell death or apoptosis.

5.4.2.2. Functional Assays of Hepatic Metabolism for KM-HA-grown hHpSCs

We sustained hHpSCs in KM-HA hydrogels for 1 week in static cultures with KM, replaced and collected daily after 24-hr incubation. We performed immunosorbent assays to determine absolute concentrations in collected KM of secretory proteins that define hepatic function. Throughout culture, hHpSCs in all tested compositions for KM-HA hydrogels (lettered formulations, Table 4) secreted AFP and albumin at increasing concentrations, while urea synthesis equilibrated to comparable levels in all KM-HA hydrogels by day 7 (Figure 17).

We obtain a more distinctive picture of hHpSC function in each KM-HA hydrogel when we normalize our data with respect to levels of viability at selected intervals (Figure 16d). This normalization yields rates of metabolic efficiency, which we interpret in terms of apparent number of functional colonies. This calculation reveals that the minimum secretion rates per colony at the end of culture for all assays (AFP, albumin and urea) correspond to KM-HA hydrogels with 1.6% CMHA-S contents (lettered formulations E and F, Figure 17).

Secretion rates of AFP, albumin and urea from hHpSCs in KM-HA hydrogels also vary in time throughout culture. Secretion rates always increase for AFP and albumin, and do so with distinctively faster paces in KM-HA formulations with 1.2% CMHA-S or less (lettered formulations A, B, C, and D). In contrast, urea secretion rates only increase throughout culture in KM-HA hydrogels with contents of 1.2% CMHA-S or less, while equilibrating or even decreasing in KM-HA hydrogels with 1.6% CMHA-S (lettered formulations E and F,

Figure 17). Moreover, the minimum secretion rates across all assays at the experimental endpoint correspond to KM-HA hydrogels with 1.6% CMHA-S and 0.4% PEGDA (lettered formulation E), which also exhibit the highest levels of viability (Figure 16d).

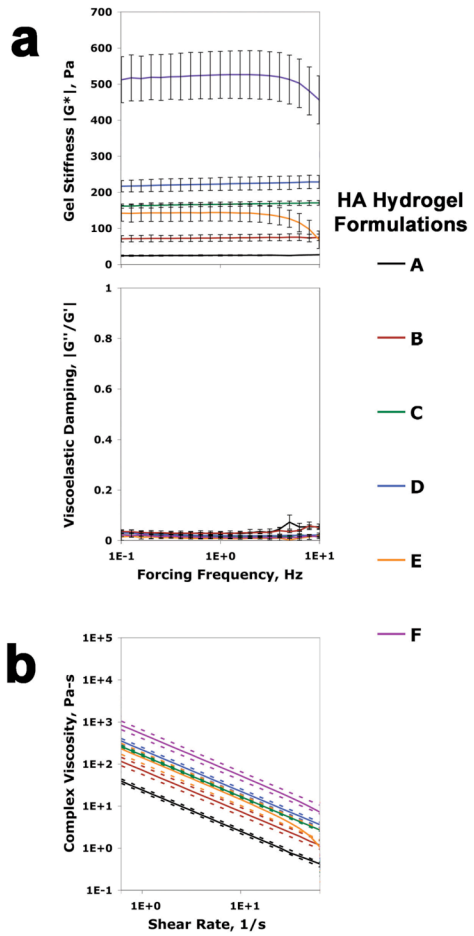

Figure 14. Rheological measurements on KM-HA hydrogels. a) The shear modulus |G*| of HA hydrogels, a measurement of mechanical gel stiffness, remains constant while viscoelastic damping |G''/G'|, a measurement of deformation response delay upon external forcing, is negligible within the 0.1 Hz – 10 Hz forcing frequency range for each of the formulations tested; error bars: 95% confidence interval of measurements at each frequency tested. b) HA hydrogels exhibit shear thinning, i.e. decrease in viscosity with increasing forcing frequencies, across experimental 0.6 1/s – 60 1/s shear rate range [0.1 Hz – 10 Hz forcing frequency]; upper and lower limits: power law model-based 95% confidence interval (Cox-Merz rule assumption, $R^2 > 0.993$ for all formulations in the 0.3 1/s – 30 1/s shear rate range [0.05 Hz – 5 Hz forcing frequency]). Rheological measurements performed only on lettered formulations shown in Table 4.

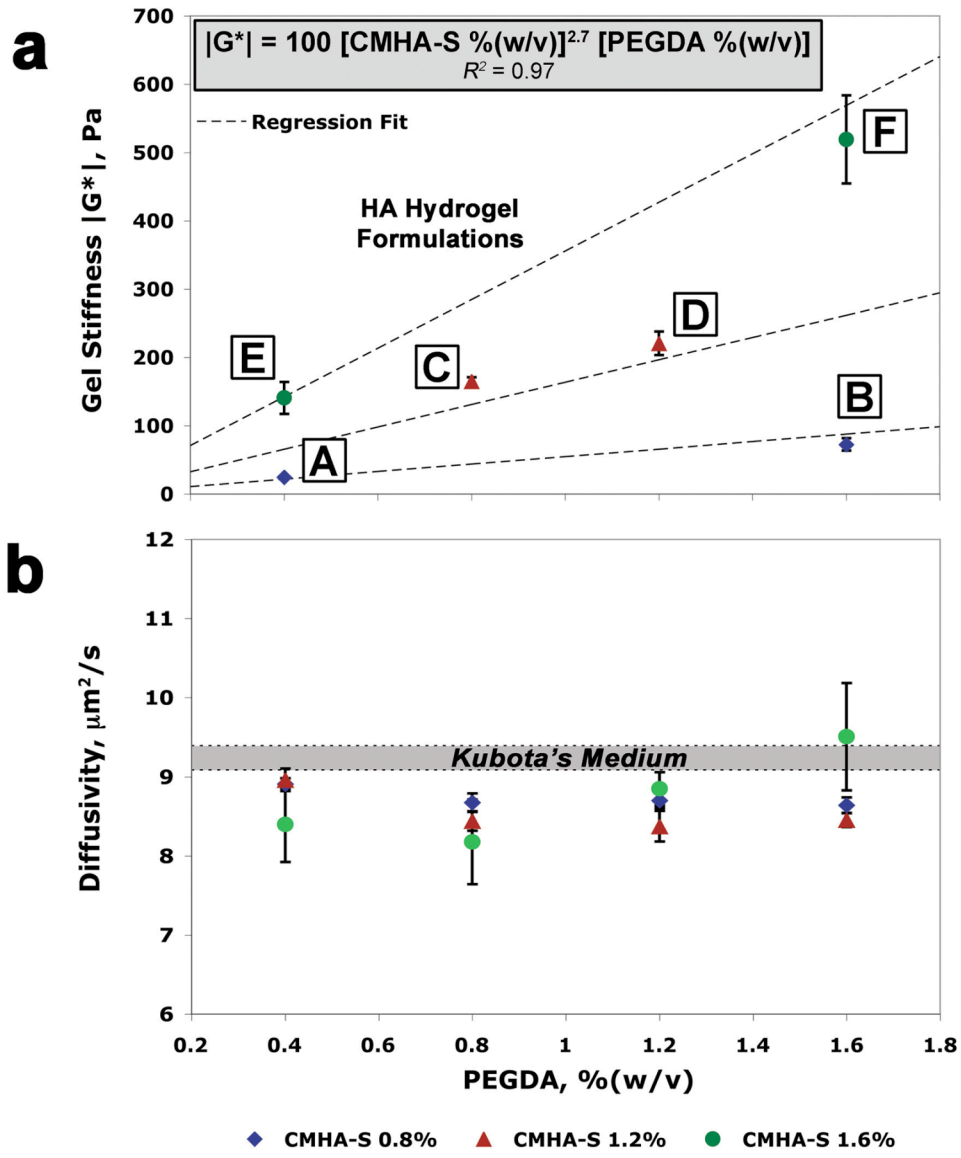

Figure 15. Mechanical characterization of KM-HA hydrogels. a) Stiffness of KM-HA hydrogels is controllable and depends on CMHA-S and PEGDA contents. The average shear modulus |G*| increases with increasing CMHA-S and PEGDA contents following a power-law behavior, thus providing direct control of the final mechanical properties of KM-HA hydrogels during the initial hydrogel mixing; rheological measurements performed only on lettered formulations shown in Table 4. Error bars: ± 1 standard deviation for measurements in the 0.05 Hz – 5 Hz forcing frequency. b) Diffusion in KM-HA hydrogels. Measurements of diffusivity within HA hydrogels by FRAP (70 kDa fluorescein labeled dextran) do not differ significantly from Kubota's medium alone; diffusivity measurements performed on all formulations shown in Table 4. Error bars: 95% confidence interval of measurements.

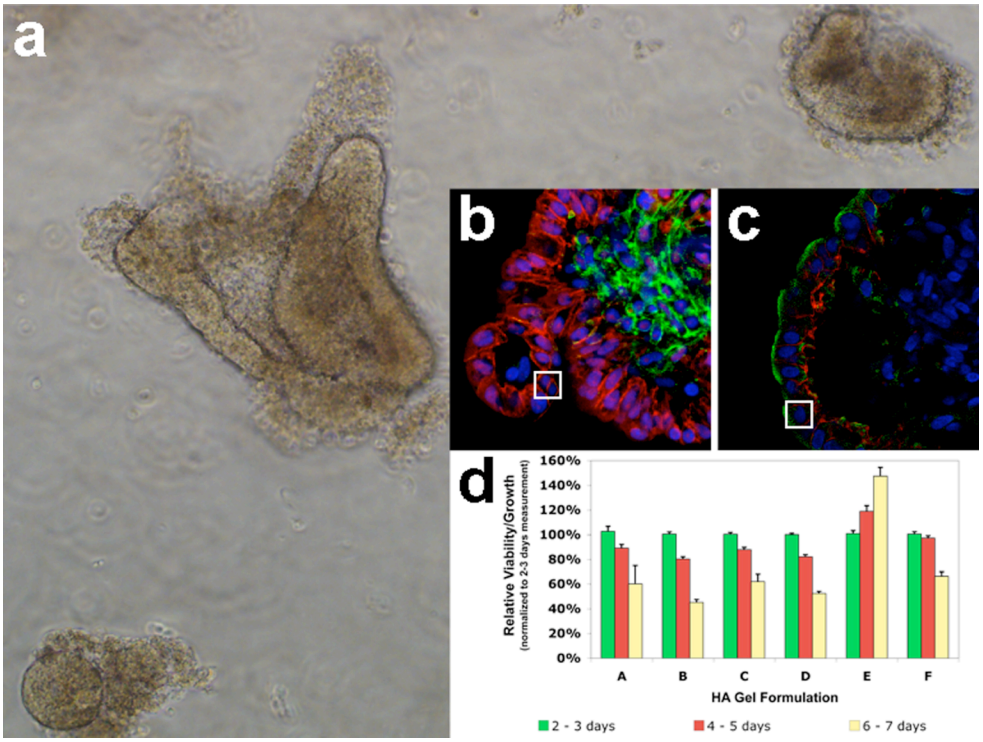

Figure 16. Size, morphology and proliferation of hHpSCs in KM-HA hydrogels. Colonies of hHpSCs acquire three-dimensional configurations and exhibit a) spheroid-like agglomeration (bottom left) or folding (middle, top right) upon seeding in KM-HA hydrogels [image frame: 900 µm × 1200 µm]. Confocal microscopy on histological sections of hHpSC-seeded KM-HA hydrogels reveals mixed cell morphology phenotypes after 1 week of culture, with cell sizes of b) about 7 µm, or c) up to 10-15 µm amongst parenchymal cells [cell nuclei in blue from DAPI counterstaining, EpCAM in red for both b) and c), green for either b) CD44, or c) CDH1; image frames b) and c): 150 µm × 150 µm; white highlight in b) and c): 15 µm × 15 µm]. d) Viability of hHpSCs in KM-HA hydrogels, measured by alamarBlue metabolic reduction, reveals functional recovery and proliferation in KM-HA hydrogels with 1.6% CMHA-S and 0.4% PEGDA (formulation E, Table 4) throughout 1 week of culture; alamarBlue reduction measurements after 24-hr incubation, normalized with respect to measurements at 2-3 days post-seeding.

5.4.2.3. Gene expression of differentiation markers in hHpSCs within KM-HA hydrogels

After 1 week of culture, levels of mRNA expression of EpCAM in hHpSC colony cells seeded within KM-HA hydrogels were significantly higher than those of 2D-grown hHpSC colonies or freshly isolated hHBs. Statistical boundaries for CD44 gene expression in hHpSCS and hHBs overlap; nonetheless, CD44 expression significantly varies across KM-HA formulations within the boundaries of either lineage stage. Levels of mRNA expression

of NCAM, AFP and E-cadherin (CDH1) for hHpSCs in KM-HA hydrogels are significantly different from those of 2D-grown hHpSC colonies. These expression levels, however, do not fall within statistical bounds of hHB expression and, in the case of AFP, are much lower than hHB mRNA expression levels (Figure 18). Therefore, hHpSCs acquired an early hHB profile in KM-HA hydrogels, as shown by AFP, CDH1 and NCAM mRNA expression.

Principal Component Analysis (PCA) of our quantitative measurements of gene expression of differentiation markers for hHpSCs (NCAM, AFP, CDH1) and markers common to hHpSCs and hHBs (CD44, EpCAM) shows that the expression variability in the hHpSC-to-hHB differentiation mechanism can be sufficiently described by only two principal components (96% cumulative variance) that are orthogonal to each other. Principal Component 1 (PC1) is strongly influenced by AFP, EpCAM, NCAM and CDH1, characterizes the differentiation phenomenon, and accounts for roughly 77% of the total variability. Principal Component 2 (PC2), influenced mostly by CD44, characterizes the intra-phenotypic variation and accounts for about 19% of the total variability (Figure 19a).

Data from KM-HA-grown hHpSCs projected onto the PC1-PC2 plane shows that their genetic expression profile is in an intermediate state between hHpSCs and hHBs, with all variation across KM-HA conditions orthogonal to the differentiation direction (Figure 19b). All data for KM-HA-grown hHpSCs are significantly distinct from either lineage stage (Figure 19c and d). When compared amongst each other, gene expression profiles for KM-HA-grown hHpSCs distribute in the PC plane distinctively with respect to the CMHA-S content of each KM-HA formulation, most significantly in PC2. In other words, intra-phenotypic variation in hHpSCs grown in KM-HAs is primarily dictated by the amount of HA in KM-HAs (Figure 19e and f). In addition, the distribution of intra-phenotypic

variation (PC2) for KM-HA-grown hHpSCs suggests a trend, although not statistically significant (Table 11), that outlines a stiffness-dependent bifurcation with increasing PC2 scores for KM-HA formulations with $|G^*| < 200$ Pa that peaks at KM-HA formulation C ($|G^*| = 165$ Pa) in our experiment, and decreasing PC2 scores for stiffer KM-HA hydrogels (Figure 19d). This trend is not evident in the PC1 differentiation score (Figure 19c).

In summary, this analysis shows that KM-HA-grown hHpSCs acquire comparable intermediate phenotypes in their differentiation progression from hHpSCs to hHBs across all KM-HA formulations. When compared across KM-HA formulations, gene expression levels of KM-HA-grown hHpSCs are most distinct with respect to their intra-phenotypic variation. This intra-phenotypic variation, which is mainly described by CD44 expression, selectively distributes KM-HA-grown hHpSCs with respect to the HA content of their KM-HA hydrogel in PC space. In addition, gene expression in KM-HA-grown hHpSCs also suggests a trend outlining a stiffness-dependent bifurcation with respect to intra-phenotypic variation, which is absent in the direction of differentiation in the PC space.

5.4.2.4. Protein expression of differentiation markers in hHpSCs within KM-HA hydrogels

We determined translational expression in hHpSCs by immunostaining for most targets. We found limited to null AFP staining, which agrees with low (yet positive) gene expression levels reported above (Figure 18). Nevertheless, we were able to use ELISA, a more sensitive assay, to compare AFP accumulation in media with mRNA expression. Although low, secretion rates of AFP by KM-HA hydrogel-seeded hHpSCs showed both increasing concentrations with time and qualitative correlation with mRNA expression levels at the experimental endpoint across KM-HA formulations (Figure 20).

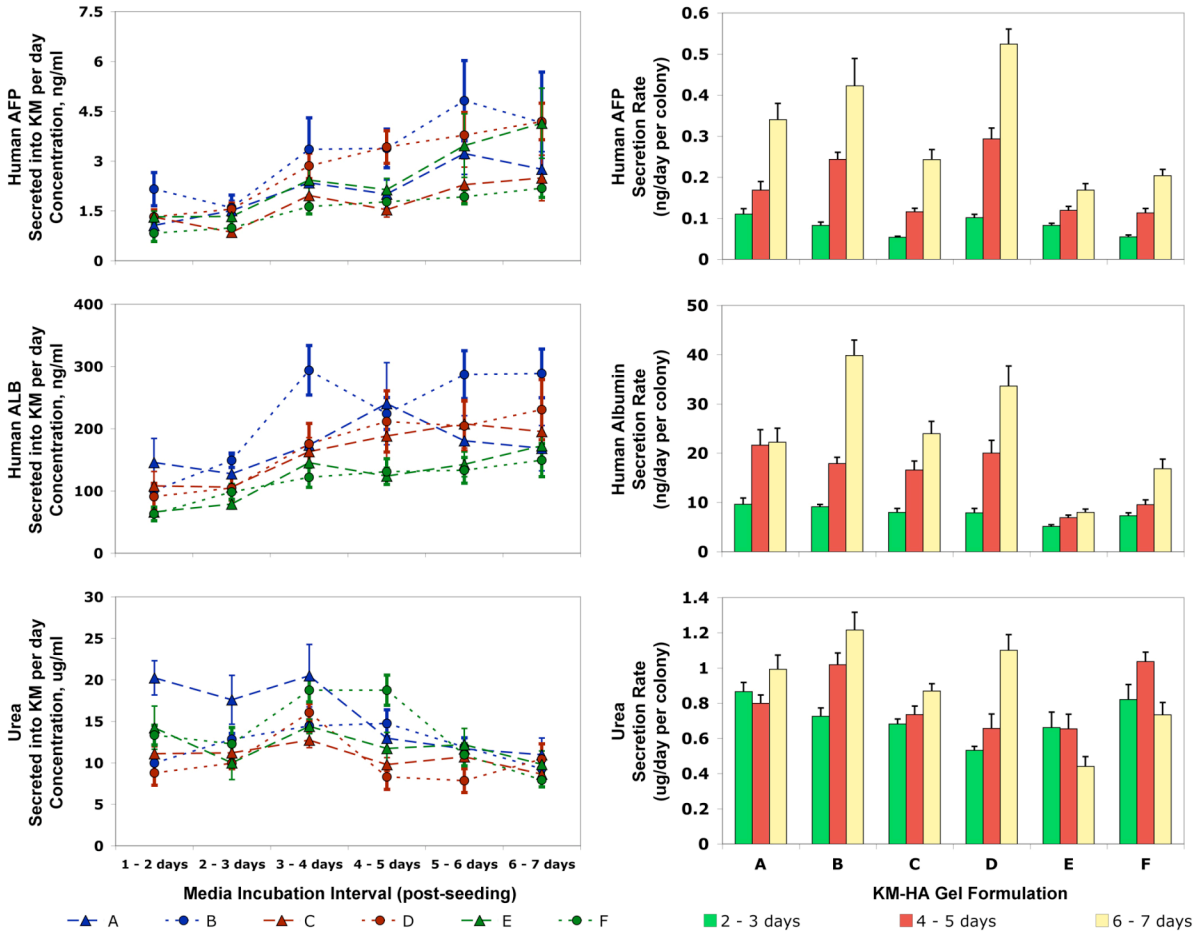

Figure 17. Secretion of human AFP, albumin and urea by hHpSCs seeded into KM-HA hydrogels. Colonies of hHpSCs in KM-HA exhibit some hepatic function with increasing concentrations of human AFP and albumin found in culture media (KM) and equilibration of urea synthesis by day 7 post-seeding. The metabolic secretion rates of human AFP, human albumin and urea are distinctive by day 7 post-seeding amongst KM-HA formulations, with minimum rates for AFP, albumin and decreased urea synthesis in KM-HA hydrogels with 1.6% CMHA-S and 0.4% PEGDA (formulation E, Table 4). Left column: metabolite concentration in culture media collected daily after 24-hr incubation for each lettered formulation (Table 4). Right column: metabolite mass secretion rate per hHpSC colony in culture media after 24-hr incubation; total metabolite mass in media is normalized to number of functional hHpSC colonies at each interval as calculated by relative viability and proliferation assay with alamarBlue reduction (Figure 16d; approximate number of colonies seeded per sample: 12). All data reported as mean ± standard error.

We studied EpCAM, NCAM, CD44 and CDH1 protein expression in thick sections of HA-grown hHpSC colonies by fluorescence microscopy to understand how their overall expression within colonies correlates with gene expression. Expectably, all hydrogel

formulations hosted EpCAM+ cells. Cells also expressed NCAM and CD44; however, CD44 appeared enriched in KM-HA formulations with 1.2% CMHA-S or less, whereas NCAM remained rich in all KM-HA hydrogels. For CDH1, protein expression paralleled mRNA expression in KM-HA formulations with |G*| < 200 Pa (A, B, E and C in Table 4). However, at higher stiffness levels, protein was undetectable (Figure 18 and Figure 20).

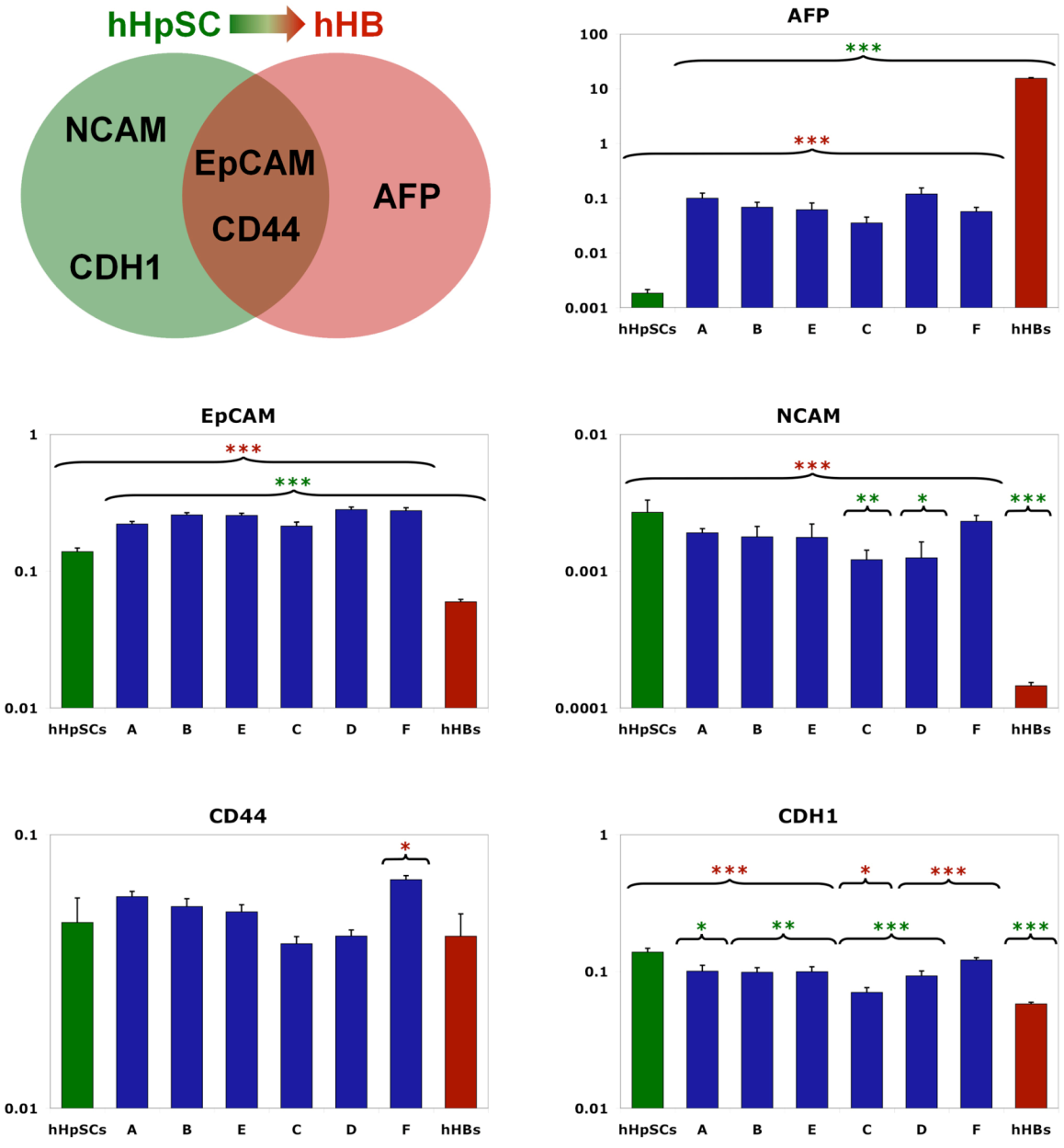

Figure 18. Gene expression levels by qRT-PCR for hepatic progenitor markers in KM-HA-grown hHpSCs after 1 week of culture (previous page). Comparisons between the mRNA expression levels of markers for hHpSCs and their immediate descendents hHBs (hepatic-specific AFP, EpCAM, NCAM, CD44 and CDH1) show that KM-HA-grown hHpSCs acquire early hHB characteristics at the transcriptional level in passive culture for 1 week. The expression ranges in hHpSCs and freshly isolated hHBs for CD44 are comparable; the expression levels for the remaining markers are statistically distinct, with approximately 2-fold decrease in EpCAM, 3-fold decrease in CDH1, NCAM silencing and AFP enrichment upon hHpSCs differentiation into hHBs. In all KM-HA hydrogels, mean expression levels of seeded hHpSCs for AFP, NCAM and CDH1 shifted outside the hHpSC range towards the hHB range, while EpCAM expression is enriched throughout, after 1 week of culture. KM-HA formulations ordered with respect to increasing stiffness (|G*| = 25 Pa for A, |G*| = 73 Pa for B, |G*| = 140 Pa for E, |G*| = 165 Pa for C, |G*| = 220 Pa for D, and |G*| = 520 Pa for F). Expression levels (mean ± standard error) were normalized with respect to GAPDH. Measurements in lettered KM-HA formulations (Table 4) compared to hHpSC colonies (green) and freshly isolated hHBs (red) for significance (Student's t-test).

We next analyzed how these differentiation markers distributed within our cultures by confocal microscopy, both across hHpSC colonies in KM-HA hydrogels and within cells. We found that, in general, there was very little co-localization of EpCAM with all other surface markers (NCAM, CD44 and CDH1) across planes of colonies. The few subsets of cells that expressed all these targets were usually exposed to external colony surfaces in direct contact with KM-HA hydrogel material (Figure 21). Further confocal analysis revealed that EpCAM+ cells in colonies within KM-HA hydrogels distributed EpCAM at their basal surfaces and towards homotypic cell-cell interactions; in contrast, cells expressing NCAM, CD44 and CDH1 localized to "outer" surfaces of colonies and presented these proteins at their apical surface with no intracellular co-localization with EpCAM (Figure 22).

5.5. DISCUSSION

Liver histology reflects hepatic maturational lineage progression within each acinus, the functional unit of the liver. Liver acini have hexagonal shape (in histological sections) and six sets of portal triads at the vertices. Each portal triad contains a hepatic artery, portal vein and bile duct. The center of each acinus is occupied by a central vein that is connected to the

vena cava [117]. Incoming blood flows from the gut and from the spleen into the liver via the portal triads. It passes across plates of liver cells before discharging into the central vein to exit the liver. By convention, three zones delineate liver acini: zone 1 is periportal; zone 2 is midacinar; and zone 3 is pericentral. Cell properties like size, ploidy, growth rates, ECM, and gene expression vary along these zones in gradient fashion. In this respect, zones 1, 2 and 3 correspond to cells in early, intermediate and late maturational stages, respectively.

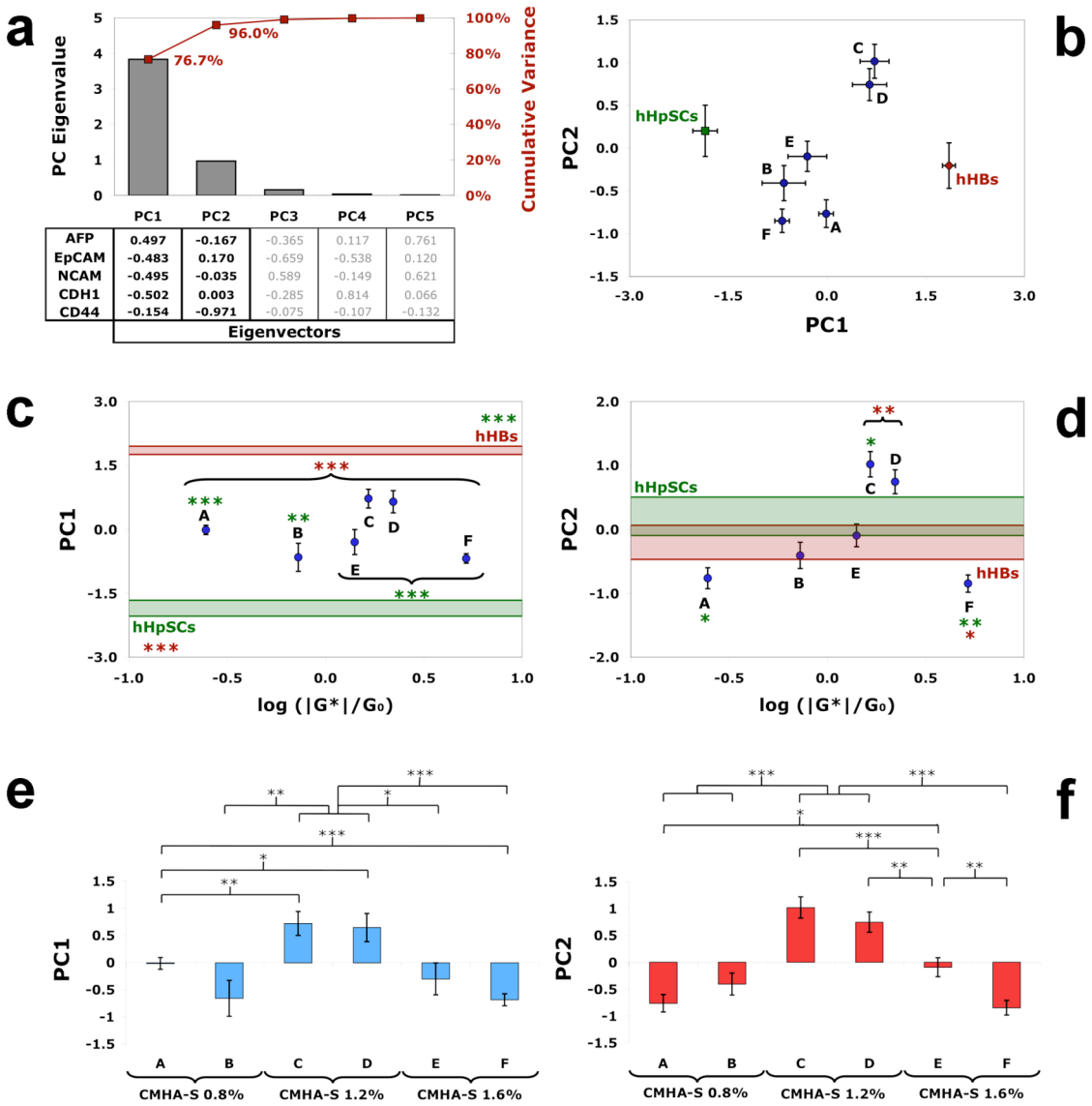

Figure 19. Principal Component Analysis (PCA) of gene expression profile (previous page). a) Two principal components (PCs) account for 96% of variance in gene expression profile between hHpSCs and hHBs with respect to hepatic progenitor markers (hepatic-specific AFP, EpCAM, NCAM, CD44 and CDH1); principal component 1 (PC1) describes differentiation and depends mostly on differences between hHpSCs and hHBs lineages with respect to differentiation markers (AFP, EpCAM, NCAM and CDH1) as shown by PC1 eigenvector; PC2 describes intra-phenotype variation and depends almost exclusively on CD44 expression. b) KM-HA-grown hHpSCs show an intermediate phenotype between hHpSCs and hHBs in PC space. Gene expression profiles in all KM-HA-grown hHpSCs exhibit significant differences from hHpSCs and hHBs c) in PC1, and d) in PC2. Expression trends in KM-HA-grown hHpSCs, as shown in c) and d), are not statistically significant with respect to KM-HA stiffness. The variation amongst KM-HA-grown hHpSCs is significantly largest between KM-HAs with different CMHA-S contents for both e) PC1 and f) PC2; highest significant differences amongst KM-HAs reside in intra-phenotype variation (PC2) that depends primarily on CD44 expression. Measurements in lettered KM-HA formulations (Table 4) compared to hHpSC colonies (green) and freshly isolated hHBs (red) for significance (Student's t-test). Expression profile scores in PC space (error bars: mean ± standard error) for lettered KM-HA formulations (Table 4) are plotted in c) and d) against normalized KM-HA hydrogel shear modulus $|G^*|/G_0$ (G_0 = 100 Pa) and compared to threshold ranges of expression in hHpSCs (green area, mean ± standard error) and freshly isolated hHBs (red area, mean ± standard error).

The intrahepatic maturational gradient starts in zone 1 (periportal) and ends in zone 3 (pericentral). At least 8 maturational lineage stages can be distinguished within the acinar zones [122]. The phenotypic properties of each stage are dictated by paracrine signaling between parenchymal and mesenchymal cell partners whose maturation is coordinate. Adjacent to the portal triad, the stem cell niche is occupied by human hepatic stem cells (hHpSCs) – partnered with angioblasts (ABs) – that transition to hepatoblasts (hHBs) – partnered with precursors of both endothelial and hepatic stellate cells (hHpSTCs). They mature outside the niche towards adult states into either hepatocytes – partnered with mature endothelia – or biliary epithelia – partnered with mature hHpSTCs and myofiboblasts [12, 16, 21].

Studies on fetal and adult human livers show that hHpSCs constitute ~0.5-2% of the hepatic parenchyma in all age donors, form colonies with differentiation potential [8, 136],

and can be identified by expression of epithelial cell adhesion molecule (EpCAM) and neural cell adhesion molecule (NCAM) but lack of expression of alpha-fetoprotein (AFP) [12]. The hepatoblasts (hHBs) constitute more than 95% of the parenchymal cells in fetal tissues; they decline in numbers to <0.01% of the parenchymal cells with age in postnatal livers, but can expand during regenerative processes [123, 125]. The phenotypic properties of the hHBs overlap extensively with that of hHpSCs but are distinct, among other features, in that they express AFP but not NCAM. Epithelial-mesenchymal interactions in hepatic tissue *in vivo* also dictate how to control expansion and differentiation of hepatic progenitors *ex vivo*. Self-replication of hHpSCs and hABs *ex vivo* requires KM [16, 20], occurs in culture on plastic, as long as the two subpopulations are associated [12], on substratum of type III collagen [31] or in uncross-linked HA [16]. Lineage restriction to hHBs occurs in KM and on type IV collagen or laminin or highly cross-linked HA hydrogels [16]. Using purified ECM components that replicate tissue-specific chemistries *ex vivo* can also mimic *in vivo* behavior [21].

In all tissues, the mechanical properties of the ECM have profound effects on signaling, transport, and on how cells respond to mechanical forces using mechanisms collectively known as mechanotransduction [137-139]. Mechanotransduction modulates cytoskeletal organization, cell cortex tension, cell adhesion, and shuttling of downstream targets between cell nuclei and cytoplasm by using different arrays of signals, for example the TGF-β superfamily [48, 50, 51, 140]. At higher scales, these cellular mechanisms influence tissue assembly through the roles of the cytoskeleton in cell migration, aggregation and proliferation [141], inducing cell aggregation on soft substrates and cell dispersion on stiff ones [142]. Mesenchymal stem cell (MSC) differentiation is also induced by substrate

stiffness [47]. However, information on how mechanical forces influence differentiation in soft tissues, such as liver, has remained limited despite our knowledge of matrix chemistry gradients across lineage stages. These matrix changes also have mechanical significance, depending in part on local sulfation levels of GAGs in the ECM that could yield varying mechanical properties across maturational gradients [107].

Hyaluronic acid (HA) is a key component in the ECM chemistry of the liver stem cell niche. HA belongs to the glycosaminoglycan (GAG) family, and is formed by disaccharide units linked with alternating β-1,4 and β-1,3 glycosidic bonds between glucosamine and glucuronic acid structures. It is found in ECM, on the cell surface and inside the cell [143]. HA is conserved across all species, is biocompatible and elicits no inflammatory, immunologic or toxic responses [127]. These properties, along with high water saturation, make it a useful building block for biomaterials for tissue engineering therapies. In addition, it can be easily modified, and is more cost effective than other ECM components [126-130]. HA is also abundant during cellular expansion events such as embryogenesis, wound repair, and organ regeneration. Neural crest cell migration, cardiac development and prostate duct formation involve HA function as a scaffold component [144-147]. Rapidly dividing epithelial cells show an increased binding activity towards HA, and it is possible that transition from epithelial to mesenchymal phenotypes takes place through interactions mediated by HA binding [148, 149]. HA in hepatic tissue interacts with liver cells through two HA receptors that mediate cell attachment of liver progenitors to ECM: hHpSCs are positive for CD44; ABs are positive for LYVE-1 [150-152]. In fact, in primary cultures and in liver injury, hepatic stellate cells produce HA, which increases in parallel with expression

of its receptor CD44, and the resulting increased levels of HA in the blood correlate with hepatic regeneration *in vivo* [153].

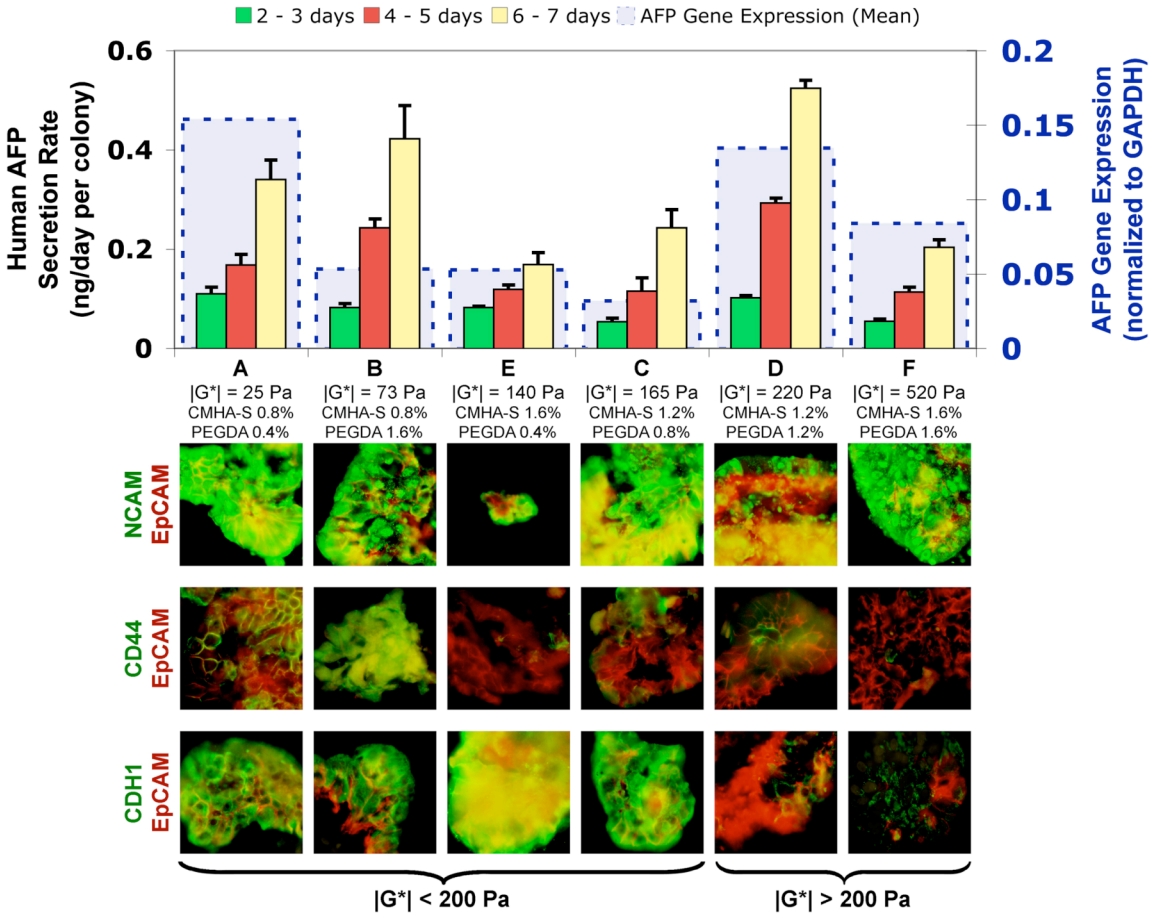

Figure 20. Protein expression of differentiation markers in KM-HA-seeded hHpSCs after 1 week of culture. Colonies of hHpSCs exhibit differential levels of expression for differentiation markers in hHpSCs at the translational level depending on KM-HA hydrogel characteristics. Metabolic secretion rates of human AFP correlate mRNA expression levels across KM-HA formulations. NCAM expression is positive for all KM-HA hydrogels, while CD44 expression is richest for KM-HA hydrogels with CMHA-S contents of 1.2% or less (lettered formulations A, B, C, D; Table 4). CDH1 expression is positive for KM-HA hydrogels with |G*| < 200 Pa and weak or negative for |G*| > 200 Pa. Data for human AFP secretion rate reported as mean ± standard error. Immunohistochemical staining for EpCAM, NCAM, CD44 and CDH1 performed on 15 – 20 µm section and imaged by fluorescence microscopy [image frames: 100 µm × 100 µm]. KM-HA formulations ordered with respect to increasing stiffness (|G*| = 25 Pa for A, |G*| = 73 Pa for B, |G*| = 140 Pa for E, |G*| = 165 Pa for C, |G*| = 220 Pa for D, and |G*| = 520 Pa for F).

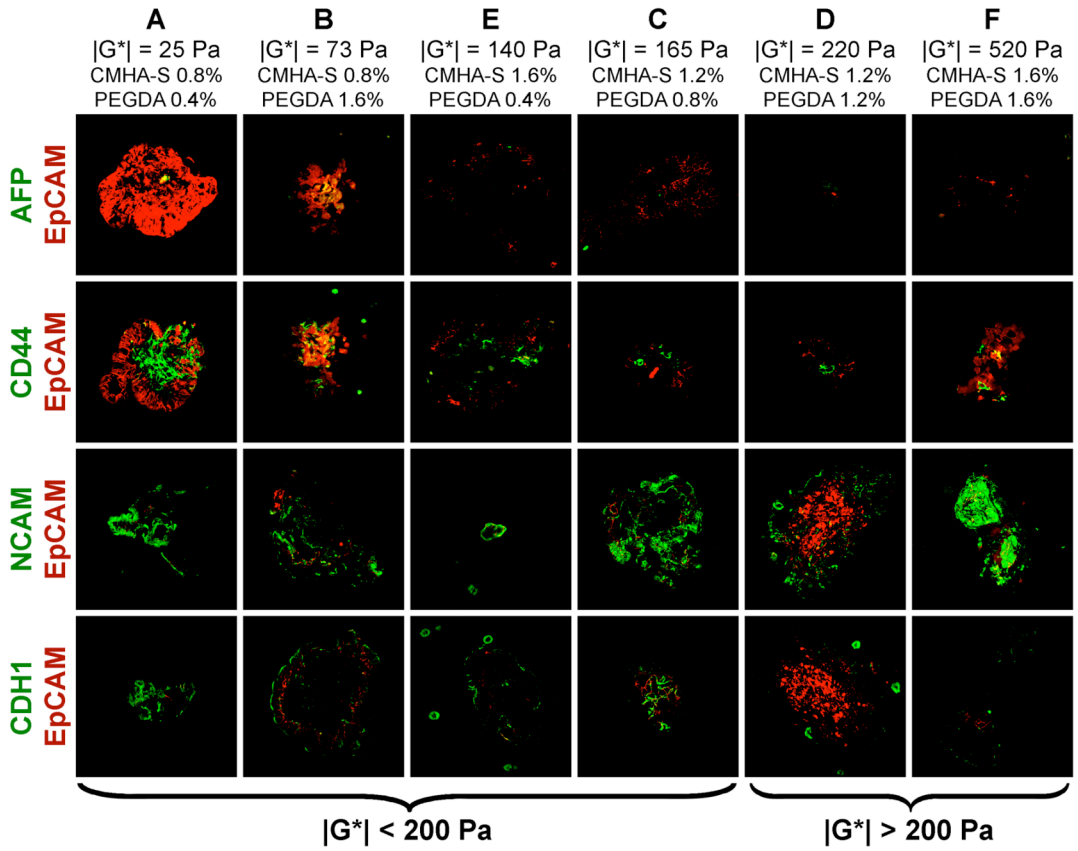

Figure 21. Co-localization of differentiation markers in KM-HA-seeded hHpSC colonies. Colonies of hHpSCs exhibit low expression levels of AFP by immunohistochemistry. Co-localization of EpCAM with other cell surface differentiation markers (NCAM, CD44, CDH1) is low or null across cells within KM-HA-seeded hHpSC colonies. Staining for AFP, EpCAM, NCAM, CD44 and CDH1 performed on 15 – 20 µm sections and imaged by laser confocal microscopy. Images depict average fluorescence collected across 11 confocal optical sections of 0.407 µm [mean filtering, total optical slice: 4.07 um; image frames: 300 µm × 300 µm]. KM-HA formulations sorted and displayed with respect to increasing shear modulus |G*|.

Replicating mechanical properties of the cell environment is relevant to tissue regeneration applications [154, 155]. We chose HA-based hydrogels in our experiment because HA is ubiquitous across stem cell niches. However, it is just as important to discriminate between biochemical and mechanical induction in order to understand lineage restriction phenomena. Tissues with normal physiology depend on cells living in environments with satisfactory mechanical properties because normal tissue assembly

requires successful signaling and mechanical sensitivity in cells [156-160]. We used tailored HA hydrogels in previous research [126-130] and found empirical evidence that human hepatic progenitors differentiated when seeded in mechanically rigid grafts [22, 26]. Therefore, we determined the mechanical properties of KM-HA hydrogels to understand the effect of the mechanical environment on differentiation and expansion of hHpSCs.

The HA hydrogels we used yield shear moduli ranging from 11 to 3500 Pa with different PEGDA and CMHA-S concentrations when mixed in buffered distilled water [130]. Dissolving these gel components in culture medium could change the absolute values of the hydrogel's mechanical properties. Therefore, measurements from water-mixed hydrogels could not quantitatively match KM-HA hydrogels since we use KM, a basal solution with different ionic properties. Our results showed that the type of basal media play a role on the mechanical properties of the HA-based hydrogels as an environment for embedded cells. Still, our measurements match the qualitative trends of water-based HA hydrogels (e.g. linear variation in stiffness with PEGDA concentration, lack of viscoelastic damping), which supports the accuracy of our measurements and shows that the hydrogel chemistry is robust and predictable for tissue engineering purposes [130]. In addition to their predictable stiffness (Figure 15a), the mechanical properties of KM-HA hydrogels offer substantial advantages for grafting technologies: we can deliver them by extrusion or syringe-driven techniques because of their shear-thinning properties, and can immediately transmit external forces to embedded cells in culture without force loss or damping because of their elastic behavior (Figure 14). All these features make KM-HA hydrogels an attractive culture model for mechanotransduction research as well, since researchers can directly control mechanical forces on KM-HA macroscopically that will be transduced equally to embedded cells.

Relevant molecular sizes for multiple paracrine signals in tissue development are in the order of 70 kDa or less [132]. For this reason, our FRAP experiments used molecules of fluorescein-labeled 70 kDa Dextran (D70) to calculate the lower limit on diffusion rates relevant to morphogenetic signals. Our measurements indicate that all tested KM-HA hydrogels have roughly equivalent diffusion rates that match ordinary cell suspension cultures, therefore providing a 3D environment for cell embedding with optimal diffusion properties (Figure 15b). In summary, our experiments permitted studies of mechanical properties of hydrogels and their effects on differentiation of hHpSCs by maintaining all other conditions (ECM molecular species, diffusivity and culture media) equivalent. Furthermore, the fact that several gels of varying rigidity had identical concentrations of either CMHA-S or PEGDA (Table 4) allowed us to distinguish between biochemical and mechanical regulation of gene expression.

Our viability measurements indicate that hHpSC colonies have distinct metabolic activities in accordance with the composition of KM-HA hydrogel hosting them. This analysis is complemented by our secretion assays. Absolute secretion is comparable across KM-HA formulations for indicators of hepatic function (AFP, albumin and urea) throughout culture; however, absolute secretion coupled with metabolic efficiency depicts a selection process that depends on the HA content. In this process, secretion rates increase under metabolic duress for KM-HA hydrogels with CMHA-S contents lower than 1.2%; in contrast, secretion rates are comparatively poor in KM-HA hydrogels with more CMHA-S (1.6%) and higher metabolic function – or even metabolic growth, as in fomulation E (Figure 16d). Because hHpSCs and hHBs exhibit different metabolic capabilities, our data suggests

that certain KM-HA hydrogels can select for expansion or differentiation of hepatic progenitors.

We also performed genetic expression analysis of differentiation markers in hepatic progenitors to determine formally whether and to what degree differentiation takes place within KM-HA hydrogels. EpCAM is a common marker of hHpSCs and hHBs at both gene and protein expression levels that is characteristically found in hHpSC colonies within regions of homotypic cell-to-cell interactions in monolayer cultures [12, 16, 21]. Our data shows increased overall expression of EpCAM beyond established levels for hHpSC colonies on plastic plates. However, we also know that these colonies acquire 3D structure within KM-HA hydrogels. A cohesive hHpSC colony in this environment would require additional homotypic cell-cell interactions amongst cells within the colony and, for that purpose, could lead to increased transcriptional levels of EpCAM expression. We believe these changes in EpCAM expression distinguish hHpSC function within a 3D environment.

NCAM, unlike EpCAM, is a unique marker of hHpSCs in hepatic parenchyma. Colonies of hHpSCs in monolayer cultures express NCAM at the edges to establish heterotypic cell-cell interactions with mesenchymal companions such as ABs [12, 16, 21]. Similarly, in our cultures, NCAM is expressed (Figure 20), heterogeneously across the colony towards the outer boundaries where heterotypic cell-cell interactions could take place (Figure 21). Consistent with this finding, NCAM is found on the apical surface of those external cells (Figure 22). The hyaluronan receptor molecule CD44 behaves similarly, even though it is common to both hHpSCs and hHBs at the mRNA expression level (Figure 18). CD44 differs from NCAM expression in that it exhibits higher enrichment levels for KM-HA hydrogels with CMHA-S contents of 1.2% or less (Figure 20). We surmise that the

localization of CD44 to cells in direct contact with HA and its heterogeneous distribution within or between colonies (Figure 21 and Figure 22) reflects its function as a HA receptor.

AFP and E-cadherin are two markers of interest for hHpSCs reflecting early cell function. A secretory protein similar to albumin [28], AFP is not expressed in hHpSCs at the transcriptional or translational levels and characterizes hHpSC differentiation to hHB [8, 12, 122, 133]. E-cadherin is a stem cell marker for germline stem cells, induced pluripotent stem cells [161-163] and, unlike AFP, it is expressed by hHpSCs and other cells at early embryonic stages [21]. In our experiment, we show that mRNA expression levels vary across KM-HA hydrogels (Figure 18) and that AFP protein expression correlates with mRNA expression (Figure 20). The effect is even more drastic for E-cadherin: protein expression is absent in KM-HAs with $|G^*| > 200$ Pa despite strong mRNA expression levels that match those of softer hydrogels, in which there is protein expression of E-cadherin (Figure 18 and Figure 20).

E-cadherin is a cell surface protein that establishes homophilic adhesions between cells for mechanosensation and induces mechanical responses through intracellular signaling cascades. E-cadherin is thought to coordinate collective cell responses to mechanical forcing by allowing cells to sense mechanical variations in their neighbors [164]. In our experiments, we observe heterogeneous E-cadherin distribution: it is expressed at apical surfaces of cells in the outer surfaces of colonies that are directly exposed to KM-HA hydrogels (Figure 22). The cells that are directly exposed to external mechanical forces are thus able to communicate the signal to adjacent cells at the external surface of the colony. Therefore, by showing that translational control of E-cadherin expression depends on environmental stiffness, we are linking signaling mechanisms in hHpSCs with their ability to

collectively adapt to the stiffness of their substrate. We conclude protein expression of E-cadherin is stiffness-dependent, even in hydrogels with equal concentrations of CMHA-S (formulations E and F; C and D), PEGDA (formulations A and E; B and F) or comparable mRNA expression levels (formulations A, B, E, D, F; Table 4, Figure 18 and Figure 20). Hence, the mechanical properties of the microenvironment can also dictate changes in hHpSC phenotype.

Changes in gene expression for hHpSC colonies cultured in KM-HA hydrogels suggest gradual differentiation occurs within these 3D environments. In our experiments, we assume differentiation takes place when mRNA expression of cells, originally in a hHpSC state, significantly shifts outside the statistical bounds of baseline hHpSC levels towards that of hHB for multiple differentiation markers – such as NCAM, AFP and E-cadherin – both individually and in a multivariate scheme, as shown by PCA. The main source of gene expression variability across KM-HA formulations is orthogonal to the differentiation phenomenon and resides in HA content of KM-HAs (Figure 19). Most importantly, the resulting genetic expression profiles fall within an intermediate state between purified populations of hHpSCs and hHBs.

Our gene expression results, both in an individual marker basis (Figure 18) and through multivariate marker analysis (Figure 19), can only evaluate the cumulative expression profile within the entire cell population in KM-HAs. In other words, our gene expression assays do not discriminate against expression heterogeneity because they average the expression profile across cells in populations that may be heterogeneous. In that respect, our gene expression results suggest that differentiation measurements intermediate between hHpSC colonies and hHB populations correspond to heterogeneous collections of hepatic progenitors. In other

words, this interpretation suggests that hHpSCs within colonies grown in KM-HAs differentiate into hHBs individually, and possibly in a stochastic fashion. By reporting the relative amount of genetic expression for differentiation markers, our data also depicts a rate of conversion of an initial hHpSC population towards a hHB lineage by single differentiation events. This conclusion is supported by heterogeneity in both cell morphology (Figure 16) and protein expression in KM-HA-grown hHpSC colonies (Figure 20 and Figure 21). Therefore, we conclude that differentiation is responsible for our genetic expression observations, that our measurements depict the pace at which it occurs within each KM-HA hydrogel formulation, and that his pace depends on the properties of KM-HA hydrogels.

We also show that, for some markers, protein expression does not correlate with mRNA expression and depends on KM-HA hydrogel properties, as happens with stiffness-dependent E-cadherin (Figure 20). These results suggest that the effects of KM-HA hydrogel properties on hHpSCs function operate at both transcriptional and translational levels. The resulting heterogeneity in cell population in KM-HA hydrogels might be preferable for tissue engineering applications, since tissues require heterogeneous populations to perform specialized functions *in vivo*.

Cell differentiation precedes cell determination. These mechanisms differ in that cell determination describes the degree to which cells acquire functions that their microenvironment requires, while complying with restrictions on gene expression imposed by their differentiated state. For example, the difference between genetic expression of AFP in hHpSCs and hHBs in our experiments is, on a first-impression basis, insurmountable through KM-HA hydrogel seeding alone. Even though our genetic expression assays for hHpSCs in KM-HA hydrogels suggest stochastic differentiation events within colonies, we

cannot predict how effectively differentiated hHpSCs acquire functional characteristics of hHBs with this information alone, even though they might have a gene expression profile able to comply with hHB function.

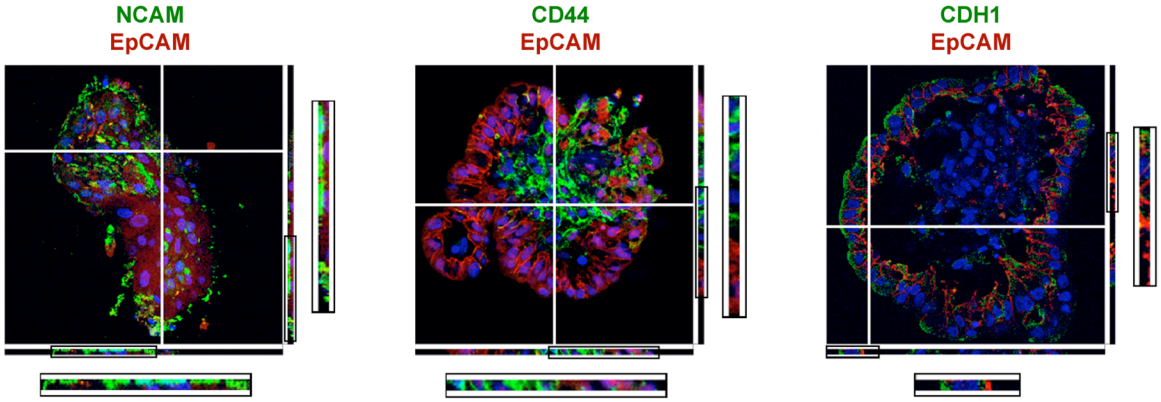

Figure 22. Cellular distribution of cell surface differentiation markers in hHpSCs seeded in KM-HA hydrogels. EpCAM is expressed in individual cells at "inner" surfaces of hHpSC colonies with homotypic cell-cell interactions. NCAM (left frame, KM-HA formulation F from Figure 21) and CDH1 (right frame, KM-HA formulation B from Figure 21) are expressed only in cells at "outer" surfaces of hHpSC colonies, in direct contact with KM-HA hydrogels, and exposed to heterotypic cell-cell interactions. CD44 (middle frame, KM-HA formulation A from Figure 21) is expressed in a subset of cells having the smallest cell sizes, poor co-localization with EpCAM expression, and in contact with KM-HA hydrogels (folded colony). Sagittal projections of full optical sections (Z-stack total optical slice: 4.07 um) show enriched EpCAM expression on the basal surfaces of individual cells; NCAM and CDH1 expression is exclusive to apical surfaces of individual cells. Staining for EpCAM, NCAM, CD44 and CDH1 performed on 15 – 20 µm sections and imaged by laser confocal microscopy. Images depict sagital projections (X and Y, through white crosshairs) of collected fluorescence across a Z-stack of 11 confocal optical sections of 0.407 µm [cell nuclei in blue from DAPI counterstaining; Z-view frames: 225 µm × 225 µm, confocal section 6 of 11].

Once a cell has differentiated to a specific fate, the process of determination starts and is subject to intracellular regulatory mechanisms that depend on ECM composition, paracrine signaling and culture conditions *ex vivo*. It also means that differences in protein expression and function between differentiated cells in culture with respect to their *in vivo* counterparts – for example, differentiated hHpSCs and freshly isolated hHBs – might arise from discrepancies between culture and *in vivo* conditions, not from the process of cell

differentiation itself. Hence, it is vital that we identify genetic markers, including novel ones, that can distinguish between hHpSC differentiation and hHB determination. Future differentiation studies with our KM-HA hydrogels should define factors involved in epigenetics whose mRNA expression in hHpSCs within 3D environments confirms lineage restriction to hHBs as early as possible, while correlating with acquisition of hHB function under the right culture conditions – a process that may occur at longer time scales than hHpSC differentiation as shown by AFP. These novel markers would allow rapid screening of hHpSC differentiation using gene expression assays alone.

In summary, our experiments show that both the chemical and mechanical properties of the microenvironemnt can influence phenotypic changes – and possibly lineage restriction – of adult stem cells from parenchymal tissues such as liver. To our knowledge, this is the first study effectively quantifying differentiation on a determined endodermal stem cell population by controlling the mechanical properties of the culture microenvironment. Most notably, differentiation in our culture model occurs in the absence of biochemical supplementation. These results indicated hHpSCs embedded in various KM-HA hydrogels exhibited differentiation to an intermediate hHB lineage within 1 week of static culture. In addition, there was stiffness-dependent regulation of CDH1 protein expression, a differentiation marker in hHpSCs, which was distinctive after 1 week of culture in KM-HAs.

The method presented for embedding hHpSCs in KM-HA hydrogels could be successfully translated to other cell culture applications, which would benefit from the inherent 3D structure, high diffusivity and the beneficial mechanical properties of the hydrogels for surgical grafting and delivery. With this information, added to control over the mechanical properties of KM-HA hydrogels, we have established an *ex vivo* model for

mechanotransduction research on hepatic progenitors. Our experimental model, which is based on hepatic stem cells, is also useful to stem cells from other soft organs because it reveals biological intricacies that are specific to stem cell function in 3D environments, unlike other culture methods currently available, and because assembling and controlling mechanical properties of KM-HA hydrogels is straightforward. Ultimately, our findings have an impact on parenchymal tissue engineering, cell-based therapies and development of bioreactors for drug discovery bioreactor because they elucidate a novel approach to control differentiation in progenitor cells from soft organs, such as hHpSCs, by mechanical methods alone.

CHAPTER 6. PRINCIPLES OF BIOMATHEMATICAL MODELING: FROM MECHANICAL PROPERTIES OF CELLS AND TISSUES TO COMPUTATIONAL MODELING OF TISSUE BIOLOGY

Biomathematical models of tissues can elucidate mechanical foundations that control multivariate biological systems. Constructing a model of tissue function is a process that integrates multiple components within a biological system and defines their interactions. One approach to this process starts with experiments quantifying how different input mechanisms, such as mechanical loading and biochemical processes, relate. Biomathematical models can implement this information to evaluate theoretical systems in cell function with respect to experimental observations. When successful, biomathematical models are powerful tools that can predict biological behavior in testable, specific and quantifiable experiments. Moreover, in certain cases, a simple biomathematical model can reveal complex phenomena that would be unexpected, or experimentally rare. This feature is a cornerstone of physics: we can dissect a mechanism into single phenomena to describe its modules, each individual module modeled faithfully to correlate with experimental evidence and ultimately assembled into a multivariate snapshot of a complex natural process.

One asset in unifying biomathematical models of tissue function is modularity in biological systems. Biological modularity refers to the functioning of living organisms by collecting and coordinating smaller units with individual function. In living organisms, those smaller units can be modular as well – for example, in the same way that organs consist of

collections of tissues, tissues consists of collections of cells and ECM, and those in turn can be analyzed with respect to smaller components or "modules". For the sake of parsimony, robustness, and efficiency in biomathematical models, building models of biological systems requires selecting an appropriate dimensional scale and justifying mechanistic assumptions that simplify models mathematically. Because of biological modularity, we do not need to include every detail of every module, but only the ones whose variability is significant at the scale of the biomathematical model. As a result, we can simplify biomathematical models by discriminating between those modules whose variability matters at the scale under study and those who do not. This balancing act is very important: an oversimplified model risks losing fidelity, while an overdefined model risks increasing complexity *without improving predictions that could be obtained from simpler models*.

Tissues respond to mechanical stimuli depending on the material properties of their cells and ECM that, one scale below, depend on cytoskeletal components and matrix molecules, respectively. The material properties of the components in all these scales work in conjunction to determine, for example, how tissues react to periodic mechanical stimuli (viscoelasticity), experience recoverable or permanent deformations (plasticity), adapt to forces immediately or gradually (creep and relaxation), or flow under the influence of pressure gradients (fluidity).

We can create a testable biomathematical model by introducing simplifying assumptions that average the effects of biological phenomena in different scales. Experimental research can enrich these biomathematical models by quantifying biological mechanisms under a common scale for parsimony. Some mechanical properties of tissues have transient variations that can be simplified in biomathematical models of tissue growth.

Other assumptions can simplify biomathematical models of tissue mechanics by analyzing the size scale of the model. In other words, the physical configuration of tissues dictates how mechanics affects them, but implementing tissue descriptions in models also depends on the mathematical vantage point: we can study a tissue as (1) a collection of individual cells, or cytoskeletal and extracellular fibers or linkages, or subcellular organelles or proteins (discrete mechanics); or as (2) a continuous structure with properties that may be averaged over the span of several of its components, which allow the structure to function as a single entity (continuum mechanics).

The biomathematical model presented in this thesis, like others before, studies tissue growth and roles of epithelial-mesenchymal interactions in tissue morphogenesis. In this model, we introduce a parsimonious assumption that describes the average behavior of developing tissues at the time scale of growth as a poroviscous fluid (as discussed later in Section 7.3.6). These studies have relevance to developmental biology, stem cell research and tissue engineering applications. Models of tissue growth address a mechanism that occurs throughout life and that is fundamental to medical applications. In summary, our model links tissue growth with intracellular activity – two tiers of biology research that are usually quantified independently – by inspecting the effect on spheroid growth of epithelial-mesenchymal interactions through signaling and proteolytic activity.

CHAPTER 7. MECHANICAL CONTROL OF SPHEROID GROWTH: DISTINCT MORPHOGENETIC REGIMES[19]

7.1. ABSTRACT

We develop a model of transport and growth in epithelio-mesenchymal interactions. Analysis of the growth of an avascular solid spheroid inside a passive mesenchyme or gel shows that sustained volumetric growth requires four generic mechanisms: (1) growth factor, (2) protease, (3) control of cellularity, and (4) swelling. The model reveals a bifurcation delineating two distinct morphogenetic regimes: (A) steady growth, (B) growth arrested by capsule formation in the mesenchyme. In both morphogenetic regimes, growth velocity is constant unless and until a complete capsule forms. Comprehensive exploration of the large parameter space reveals that the bifurcation is determined by just two ratios representing the relative strengths of growth and proteolytic activity. Growth velocity is determined only by the ratio governing growth, independent of proteolytic activity. There is a continuum of interior versus surface growth, with fastest growth at the surface. The model provides a theoretical basis for explaining observations of growth arrest despite proteolysis of surrounding tissue, and gives a quantitative framework for the design and interpretation of experiments involving spheroids, and tissues which are locally equivalent to spheroids.

[19] Lozoya OA, Lubkin SR. Mechanical control of spheroid growth: Distinct morphogenetic regimes. Submitted for publication; appears as this chapter with permission from the authors.

7.2. INTRODUCTION

The importance of growth regulation cannot be overstated. It marks the difference between simple organisms that can only change size, and complex organisms with complex morphology and differentiated tissues. It is vital in maintaining stem cell niches. It marks the difference between homeostasis and neoplasm. Growth regulation is so fundamental and universal that we would like to understand it from a fundamental level.

Growth regulation is not solely dependent on autonomous genetic control, but is governed by environmental cues, including the mechanics in the microenvironment. In this paper, we focus on the relationship between the chemical and mechanical growth regulatory mechanisms in as simple a system as possible: solid spheroids. Many tissue systems can be modeled as growing solid spheroids, including primitive non-lumened epithelia such as those in branching morphogenesis of salivary gland lobules [165] and mammary terminal end buds [166], stem cell niches [167], solid avascular carcinomas [168], and embryoid bodies (EB) [169], used in basic research as well as in tissue engineering such as bioprinting [170]. In the normal epithelio-mesenchymal relationship, there is continuous regulation of each tissue by the other and by their shared environment. In mesenchyme-free experiments *in vitro*, an extracellular scaffold is preferred, or the tissue deteriorates. We aim to understand the morphogenetic and regulatory phenomena in as general a context as possible, and ask what the commonalities are in native tissues and in the simplified systems studied *in vitro*, i.e. solid confluent spheroids raised in a gel.

Our approach in this paper is bottom-up, not top-down. We are not asking what happens in a specific organism at a specific stage. Rather, we are asking generically what is needed

and what is not to accomplish a certain task in development. With this bottom-up approach, we echo the evolutionary path from simple to complex.

The purpose of this study is to elucidate the mechanics of generalized epithelio-mesenchymal relationships in morphogenesis, and control of the mechanics by biochemical signals. To this purpose, we have developed a mathematical model of the mechanics and control of a growing avascular solid tissue in a passive mesenchyme or gel. The model focuses on regulation of growth by growth factors (GF), availability of raw materials, and availability of compliant space. Taking the simplest and most general approach possible, we focus on regulation of growth in a solid avascular spheroid. The mechanisms which regulate growth of a spheroid are some of the lower-level mechanisms that enable higher-level mechanisms to regulate morphogenesis of more complex structures - which may be locally spherical, such as the tip of a cylinder. These growth-regulating mechanisms in a mature organism can make the difference between a stable stem cell niche and a neoplasm. Our purpose in this paper is to ask and perhaps to answer the question, "What are minimal requirements for growing a solid spheroid and halting growth, given the physical world that growing tissues live in?"

7.3. THE MODEL

7.3.1. Model components

Our model tracks the conservation and transport of generic cells, extracellular matrix (ECM) components, interstitial fluid, growth factors, and proteases. The model further distinguishes between the inner tissue (which, for definiteness, we refer to as epithelium) and the tissue/material surrounding it, either mesenchyme or nonliving culture gel (which, for

definiteness, we refer to as mesenchyme). Model variables and parameters are described in Table 7 and Table 8.

7.3.2. Mixture framework

Because we track interstitial fluid flow and tissues of changing density, we use a mixture formulation [171]. We model a tissue as containing volume fractions of cells, ECM, and fluid. Because we do not track motion of cells relative to the ECM, we group cells and ECM components into a single phase of volume fraction (cellularity) θ and velocity $\mathbf{v}$. The interstitial fluid has volume fraction (porosity) $1-\theta$ and velocity $\mathbf{w}$.

Table 7. Model variables

Variable	Symbol	Units
time	t	s
cell velocity	$\mathbf{v}$	m/s
interstitial velocity	$\mathbf{w}$	m/s
cellularity	θ	-
porosity	$1-\theta$	-
epithelial identity	e	-
mesenchyme or gel identity	$1-e$	-
epithelial growth rate	R_{EG}	1/s
mesenchyme dissolution rate	R_{MR}	1/s
interphase pressure	P	Pa
hydraulic conductivity	K	Pa
swelling pressure	σ	Pa
effective unbound growth factor activity	G	-
effective substrated protease activity	N	-

7.3.3. Distinction between tissues

To track the epithelio-mesenchymal interface, we use a diffuse interface (phase field) method. The cell/ECM phase is divided into a growing epithelial fraction e and a mechanically passive mesenchymal fraction $1-e$. The tissue interface is represented by a

smooth but steep transition region between $e = 0$ (mesenchyme) and $e = 1$ (epithelium). For parsimony, any basal lumina is lumped with the mesenchyme. The conservation equations for epithelium and mesenchyme are

$$\frac{\partial(\theta e)}{\partial t} + \nabla \cdot (\theta e \mathbf{v}) = R_{EG}$$

$$\frac{\partial(\theta(1-e))}{\partial t} + \nabla \cdot (\theta(1-e)\mathbf{v}) = -R_{MR}$$

where R_{EG} is the epithelial growth rate and R_{MR} the rate of dissolution of mesenchyme by MMP. The conservation equations for cellularity and porosity are then

$$\frac{\partial \theta}{\partial t} + \nabla \cdot (\theta \mathbf{v}) = R_{EG} - R_{MR}$$

$$\frac{\partial(1-\theta)}{\partial t} + \nabla \cdot ((1-\theta)\mathbf{w}) = R_{MR} - R_{EG}$$

yielding conservation of volume:

$$\nabla \cdot (\theta \mathbf{v} + (1-\theta)\mathbf{w}) = 0.$$

7.3.4. Control

The system is controlled by interactions between generic growth factor, protease, and swelling. We track the transport and activity of a generic transmembrane protease, bound to the epithelial cell surface, that digests the mesenchyme. Rather than include all known proteases, such as MMPs and all their known regulators such as TIMPs, we lump all net activity of substrated protease into a single variable N. We account for protease activation in the epithelium upon its interaction with mesenchymal substrate; similarly, we also define a rate of unsubstrated (or latent) transmembrane protease internalization. We only allow proteolysis to occur at the epithelium-mesenchyme interface. By Michaelis-Menten kinetics

at quasi-steady state, the conservation equation for net content of active protease in the tissue is then

$$\frac{\partial}{\partial t}\left(N\theta e\right)+\nabla\cdot\left(N\theta e\,\mathbf{v}\right)=\frac{k_{cat}^{N}}{K_{M}^{N}}\cdot\left(C-N\right)\theta e\cdot F\,\theta\left(1-e\right)\cdot\Omega\left(N\right)-k_{H}^{N}\cdot\frac{K_{M}^{N}}{F}\cdot N\theta e$$

where C is the total concentration of protease at cellular steady state in the epithelium, F is ECM substrate concentration in the mesenchyme, $\Omega(\circ)$ is a Heaviside step function, and the other parameters are defined and estimated in Table 8. Mesenchyme is remodeled by proteolysis at a rate

$$R_{MR}=\frac{k_{cat}^{N}}{F}\cdot N\theta e\cdot\theta\left(1-e\right).$$

Proteolytic digestion of mesenchyme releases (by solubilization) and activates growth factor, which is then transported through the aqueous phase. The soluble growth factor in the aqueous phase is consumed by the epithelium via internalization of ligand-receptor complexes. We neglect endogenous GF synthesis. With quasi-steady state ligand-receptor dissociation kinetics, the conservation of unbound soluble growth factor in the tissue is then

$$\frac{\partial}{\partial t}\left[G\left(1-\theta\right)\right]+\nabla\cdot\left[G\left(1-\theta\right)\mathbf{w}\right]=D_{G}\nabla^{2}\left[G\left(1-\theta\right)\right]+k_{cat}^{N}\left(\frac{S}{F}\right)\cdot N\theta e\cdot\theta\left(1-e\right)-k_{I}^{B}\left(T\frac{G}{G+K_{D}^{R}}\right)\cdot\theta e$$

where $S = B + G$ is the total concentration of growth factor solubilized and activated by mesenchyme proteolysis, B and G are the concentrations of bound and unbound activated growth factor, and T is the concentration of ligand receptors at steady state in the epithelium.

Growth of a crystal or stony coral proceeds from the surface outwards, and is modeled as a surface phenomenon. Soft tissues, however, grow volumetrically – interior locations move apart from each other. The key physical difference between volumetric and surface growth is transport. Cells cannot grow and divide without an influx of raw materials,

including water. Conservation of mass requires that as a tissue expands, an equal mass of substrates must move into it. This requires a net flow into the tissue, which is achieved through a variety of mechanisms, including diffusion, vesiculation, pressure-driven flow (swelling) between cells and, at a larger scale, via ducts. Physical impediments to transport, e.g. a dense glycocalyx, will inhibit growth. Since inflow of materials is impossible at zero porosity, we assume that a growing tissue has a regulatory mechanism that maintains a small porosity $1-\theta_c$ to allow advection of raw materials (including water) and unbound soluble growth factor *G* into the tissue. That is, when porosity becomes too small (cellularity above confluence limit θ_c), growth stops. We model the local volumetric growth rate as proportional to the persistence level of bound cell receptors in the epithelium, as is recognized for the EGFR system [172-174]. Thus the ligand-dependent epithelial growth rate is modeled as

$$R_{EG} = k_l^B \left(\frac{B}{T}\right) \cdot \theta e \cdot \left(1 - \frac{\theta e}{\theta_C}\right).$$

We assume that the tissue also has a regulatory mechanism that draws fluid into a growing tissue. This appears in our model as the swelling pressure σ. The swelling pressure is modeled as an increasing function of cellularity, but is set to zero below a certain cellularity threshold θ_σ:

$$\sigma = h_0 \left(\frac{\theta e - \theta_\sigma}{\theta_C - \theta_\sigma}\right)^2 \Omega\left(\theta e - \theta_\sigma\right).$$

7.3.5. Initial conditions

For definiteness, we define an initial 50 μm radius sphere of "confluent" epithelium (cellularity $\theta = \theta_C = 90\%$) surrounded by mesenchyme (cellularity $\theta = 20\%$). Since we assume

that GF is mesenchyme-bound until released by protease activity, the model has $G = 0$ initially. Transmembrane protease activity is initially zero except in a thin band near the epithelial surface (Figure 23).

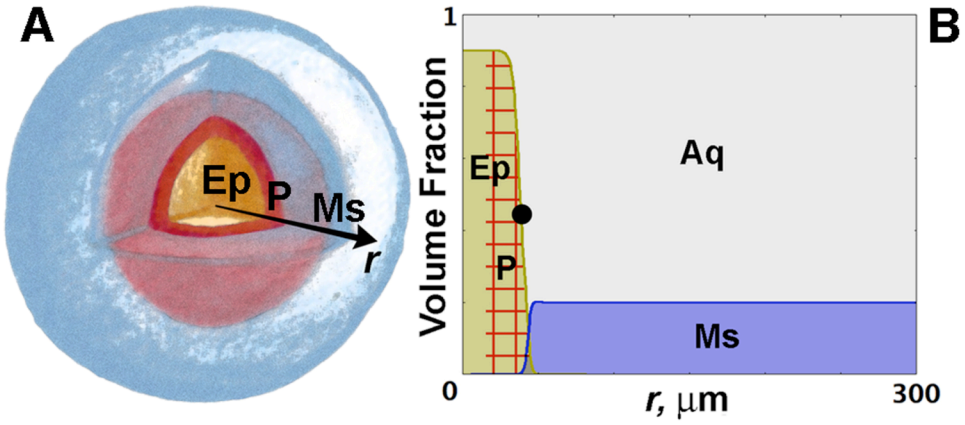

Figure 23. Geometry and initial conditions in one-dimensional model. (A) Schematic of model domain for epithelium spheroid surrounded by mesenchyme. (B) Radial distributions of initial epithelium (Ep), mesenchyme (Ms) and interstitial aqueous (Aq) phases; grid area highlights region of protease (P) activity. Dot (●) represents location of epithelial surface, $r_{\theta e}^{S}(t)$, defined as where $\theta e = \theta_c / 2 = 45\%$.

7.3.6. Mechanics

We must consider mechanical properties of developing tissues when modeling their morphogenesis. Soft tissues are viscoelastic, and their diverse behaviors are described by a variety of models. It is important to note that because they are living, tissues' mechanical behavior depends strongly on the time scale of interest.

Mature soft tissues are well described as poroelastic, i.e. as a mixture of a solid and a fluid [175], deforming under mechanical stresses and returning to an equilibrium configuration. The coupling of growth with poroelasticity can lead to residual stresses, as seen for example in the cardiovascular system, whose function is to confine flow under high pressure without failure. Residual stresses are observed when an incision springs open.

Table 8. Parameters reported in literature with ranges used in multivariate random sampling

Parameter	Symbol	Reported values	Model Values
Sampled Input Parameters			
Tissue shear modulus of viscosity [159, 176-178]	μ	$10^4 – 10^7$ kg/m-s	$10^4 – 10^7$ kg/m-s
Hydraulic conductivity [179]	K_0	$10^{-14} – 10^{-12}$ m^3-s/kg	$10^{-14} – 10^{-12}$ m^3-s/kg
Ligand diffusivity [174, 180-183]	D_G	0.1 – 100 μm^2/s	0.1 – 100 μm^2/s
Ligand supply from mesenchyme to aqueous phase [184][20]	S	10-50 pM	100 pM – 1 μM
Transmembrane protease density [185][21]	C	~ 50,000 receptors/cell	4.7 – 470 nM
Protease catalytic rate [186]	k_{cat}^N	16.2 hr^{-1} = 4.5 × 10^{-3} s^{-1}	4.5 × 10^{-4} – 4.5 × 10^{-2} s^{-1}
Latent protease endocytic rate [187, 188]	$k_H^N \approx k_I^B$	2.4 × 10^{-3} s^{-1}	2.4 × 10^{-4} – 2.4 × 10^{-2} s^{-1}
Ligand-receptor dissociation constant, steady state EGFR system [173, 189]	K_D^R	4.3 – 4.7 nM	450 pM – 45 nM
Fixed Input Parameters			
Ligand receptors density, steady state EGFR system [173] [22]	T	~ 30,000 receptors/cell	28 nM
Mesenchyme substrate content; collagen in early mesenchymal tissues [190]	F	< 5 mg/ml = 20 μM	10 μM
Protease Michaelis constant [186]	K_M^N	8.5 μM	8.5 μM
Bound receptor endocytic rate, steady state EGFR system [173]	k_I^B	2.4 × 10^{-3} s^{-1}	2.4 × 10^{-3} s^{-1}
Specific solvation stress or "swelling pressure" [191-195][23]	h_0	< 10^4 Pa	100 Pa
Epithelial target fraction	θ_C	N/A	90%
Swelling threshold	θ_σ	N/A	65%
Characteristic length	$L = 2R_0$	100 μm	100 μm
Characteristic time [173][24]	τ	4.7 × 10^4 s = 13 hours	4.7 × 10^4 s

In embryonic tissues [196], however, pressures are generally low, cell-cell adhesions are few and transient, and ECM turnover is rapid relative to the time scale of growth.

[20] 10-50 pM in media during signaling *in vivo;* Continuous supply at 270 pM *in vitro* induces 100% mitogenic response

[21] Assuming spherical 15-μm diameter cells at ~ 50,000 receptors/cell; 8.3 fmoles per 10^5 cells; ~ 47 nM

[22] Assuming spherical 15-μm diameter cells at ~ 30,000 receptors/cell; 5.0 fmoles per 10^5 cells; ~ 28 nM

[23] Up to ~10^4 Pa (75 mmHg) in neoplastic tissues; much higher than normal tissues

[24] Reference 9-hour doubling rate ≈ 69% of τ under exponential growth

Embryonic tissues exhibit phase ordering that parallels behavior in liquid mixtures [159, 160, 176-178, 190, 197, 198]: they can fuse, exhibit viscous behavior, and demonstrate incompressibility and surface tension [159, 176-178]. Their mechanical response to stress is viscoelastic with characteristic relaxation times of ~ 2 minutes and complex shear modulus G* of ~ 8 kPa. In other words, embryonic tissues behave more like Maxwell-class viscoelastic fluids – short-term elasticity with long-term viscosity – dissipating stress by making permanent cell rearrangements [159, 198, 199]. For example, stage 10 *Xenopus* chordamesoderm, ectoderm, and mesendoderm [200-202], and 5-day chick cardiac cushion [177] have a primarily viscous, rather than elastic, constitutive law. Fragments of these tissues do not spring open, but rather round up. Since we are interested here in the time scale of development that is much larger than the relaxation time of developing tissues (small Deborah number), we neglect the short-term elastic component of embryonic viscoelasticity, and model the passive mechanics of the tissues as a mixture of two *fluid* phases, i.e. poroviscous.

The level of cell-cell adhesion determines the viscosity of embryonic tissues, which is linear in cadherin levels [203]. It has been suggested that differences in mesenchymal viscosity may affect both the time course and the morphology seen in branching morphogenesis [158, 204, 205]. For simplicity, we assume a constant viscosity of both tissues.

Because we are interested in the time scale of growth, at which internal tissue stresses are dissipated, we take the viscous limit of the viscoelastic formulation. Since the viscosity of the aqueous phase is negligible relative to the cell-ECM phase the momentum conservation

for the aqueous phase reduces to a generalization of Darcy's law. The momentum balances for the cell-ECM phase and aqueous phase are written

$$\nabla\cdot\left(\theta\left(2\mu\mathbf{E}_c-\frac{2}{3}\mu\left(\nabla\cdot\mathbf{v}\right)\mathbf{I}\right)\right)-\frac{1}{\mathrm{K}}\left(\mathbf{v}-\mathbf{w}\right)=\theta\nabla P+\nabla\left(\theta\cdot\sigma\right)$$

$$\frac{1}{\mathrm{K}}\left(\mathbf{v}-\mathbf{w}\right)=\left(1-\theta\right)\nabla P+\nabla\left(\left(1-\theta\right)\cdot\sigma\right)$$

where $\mathbf{E}_c$ is the strain-rate tensor, μ is viscosity, P is interphase (capillary) pressure, K is hydraulic conductivity, and σ is swelling pressure. We assume constant μ but we model K as an increasing function of porosity, of the form $\mathrm{K}=\mathrm{K}_0\frac{1-\theta}{\theta}$. Swelling pressure σ is a key regulatory term in our model and is described in the Control section above.

7.3.7. Geometry and time

All simulations are in a spherically symmetric geometry of radius 300 μm, and were run to 1 day.

7.4. RESULTS

7.4.1. Requirements for volumetric growth

If epithelium is allowed to grow with zero swelling pressure, its cellular volume fraction increases locally up to saturation, after which growth is confined to the surface, as in a crystal. Volumetric growth requires both (a) epithelial target fraction θ_c below 100% and (b) nonzero swelling pressure σ. Without both of these features, new material cannot reach the interior of the epithelium, and growth is restricted to the surface. We refer to the equilibrium cellularity of an epithelium that can still sustain interstitial transport as the *confluence limit*.

7.4.2. Capsule formation and dissolution

When a tissue is growing volumetrically, it is pulling materials into itself, as discussed above. If there is no lumen or vasculature, new material can only come to an epithelium from

outside, from the interstitium of the surrounding mesenchyme (or gel). As interstitial fluid is drawn into a volumetrically growing epithelium, the neighboring mesenchyme (gel) becomes denser unless it is remodeled at a pace that matches epithelial growth. If the condensing tissue does not remodel itself, and is not dissolved by proteases, it will form a capsule around the growing tissue, as we have previously shown [206]. This capsule inhibits transport into the epithelium. If the capsule reaches 100% volume fraction, interstitial transport to the epithelium halts, and growth is arrested. Therefore sustained epithelial growth requires dissolution of the inevitable capsule formed as a byproduct of volumetric growth. The model uses variable protease activity to perform this function.

7.4.3. Distinct morphogenetic regimes

The model exhibits three distinct morphogenetic regimes (Figure 24). In *bulk growth* (BG), the densest tissue is at the center of the spheroid, cellularity remains below the confluence limit everywhere ($\theta e < \theta_c$), and growth is spatially distributed throughout the epithelium. In *surface growth* (SG), the epithelium is of uniform density, at the confluence limit ($\theta e = \theta_c$), and all growth is at the surface. In *capsule formation* (CF), the epithelium is above the confluence limit ($\theta e > \theta_c$), the capsule is densest at the surface and some of the tissue is pressed centripetally as its interstitial fluid is drawn centrifugally (Figure 28). When the capsule reaches 100% cellularity (zero porosity), transport is halted, and growth is arrested.

7.4.4. Bifurcation

In the parameter space tested, surface growth (SG) formed the bifurcation boundary between bulk growth (BG) and capsule formation (CF) (Figure 25). The subset of 8-dimensional parameter space corresponding to SG models was fitted by a compound-expon-

ential function $\Lambda = K_{EG} \exp\left[-\left(a + b \cdot \left(K_{MR}\right)^c\right)\right]$ (a = 1.2, b = 0.2, c = 0.7) where $\Lambda = 1$ for SG, $\Lambda < 1$ for BG, and $\Lambda > 1$ for CF. The bifurcation parameter Λ relates two nondimensional ratios, for epithelial growth $K_{EG} = \frac{k_I^B S \tau}{T}$ and mesenchyme removal $K_{MR} \equiv \frac{k_{cat}^N C \tau}{F}$. Several of the sampled parameters did *not* influence the bifurcation: tissue modulus of viscosity μ, hydraulic conductivity κ_0, ligand diffusivity D_G, latent protease endocytic rate k_H^N, and ligand-receptor dissociation constant K_D^R. Varying the initial cellularities (from 90% and 20%) did not qualitatively affect the results.

7.4.5. Surface vs. interior growth

In bulk growth (BG), the ratio Γ_{CS} of mitotic rates at the spheroid core and surface was always less than 1, and went to 0 as the tissue approached the confluence limit (SG) at $\Lambda = 1$ (Figure 25B and Figure 26B). Hence in BG much of the growth is at the surface, and in SG, all of the growth is at the surface (Figure 26). The more interstitial space in the epithelium, the higher the fraction of core growth (linear relationship) (Figure 25B).

7.4.6. Growth velocity

The epithelial spheroid expanded at a constant radial velocity (μm/day) in all cases except when capsule formation had arrested growth (Figure 24). The surface velocity $V_{\theta e}^S$ is linear in the nondimensional epithelial growth ratio K_{EG} (Figure 27A): $V_{\theta e}^S = p \cdot K_{EG}$ (p = 8.1 μm/day, R^2 = 0.93) during steady growth (BG, SG and CF models until capsular growth arrest). The total epithelium content E increases with epithelial surface velocity $V_{\theta e}^S$ with a relationship characteristic of a sphere dilating at a constant radial velocity $V_{\theta e}^S$ such that $\Delta E \equiv \left(E_f - E_0\right)/E_0 = 3\Psi + 3\Psi^2 + \Psi^3$ where $\Psi = V_{\theta e}^S \cdot \left(t_f - t_0\right)/R_0$ (R^2 = 0.998) (Figure 27B).

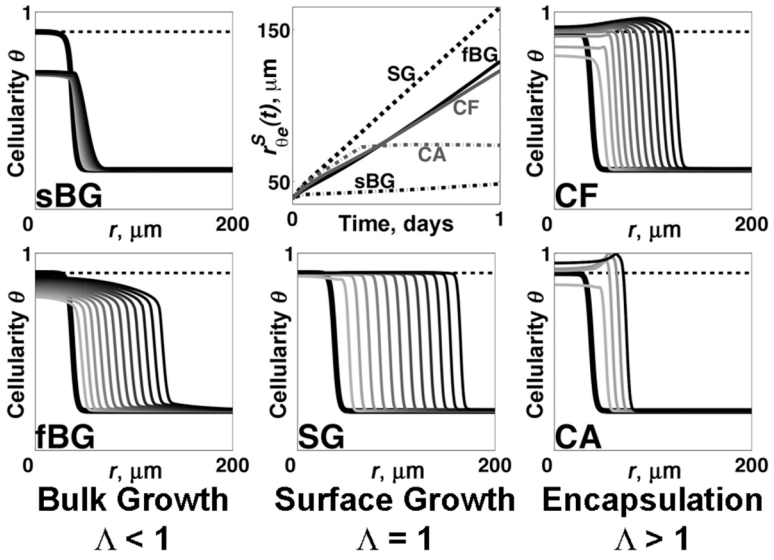

Figure 24. Time series of cellularity profile showing examples of fundamental morphogenetic outcomes: bulk growth (BG), which can be slow or fast (sBG, fBG); surface growth (SG); capsule formation (CF); and complete capsule with growth arrest (CA). BG is subconfluent ($\theta_{\max} < 90\%$); SG is constant at the confluence limit $\theta_{\max} = \theta_C = 90\%$; CF and CA are superconfluent ($\theta_{\max} > 90\%$). CF progresses to CA as it completes encapsulation ($\theta = 100\%$) at the surface. The surface, defined at $\theta e = \theta_c / 2 = 45\%$, exhibits radial displacement that is linear in time ($R^2 = 1$) and corresponds to a constant epithelial surface velocity $V^S_{\theta e}$. The exception is CA models: their overall velocity $V^S_{\theta e}$ is bilinear ($R^2 < 1$) with fast initial displacement followed by immediate stalling after complete encapsulation, thus exhibiting growth arrest. Data in time series plots: solid curve represents initial conditions (same for all models, as described in Figure 23); dashed line is the confluence limit $\theta = \theta_C = 90\%$; curve spacing every 2 hours; all plots correspond to 1 day except for CA displayed until time of arrest.

7.5. DISCUSSION

The simple bifurcation criterion provides a guide to the design and interpretation of experiments. For example, if the aim is to grow a spheroid without encapsulation, then ensuring that $\Lambda < 1$ ensures that the capsule will not form. That is achieved by reducing K_{EG}, but can also be achieved by increasing K_{MR} (Figure 25C). K_{EG} and K_{MR} can each be regulated independently by regulating several different factors. For example, K_{EG} can be halved experimentally by halving the ligand supply *S*, doubling the receptor density *T,* or

doubling the bound receptor endocytic rate k_l^B. Some of these manipulations may be substantially easier to perform than others; some are endogenous to the cells and some are external.

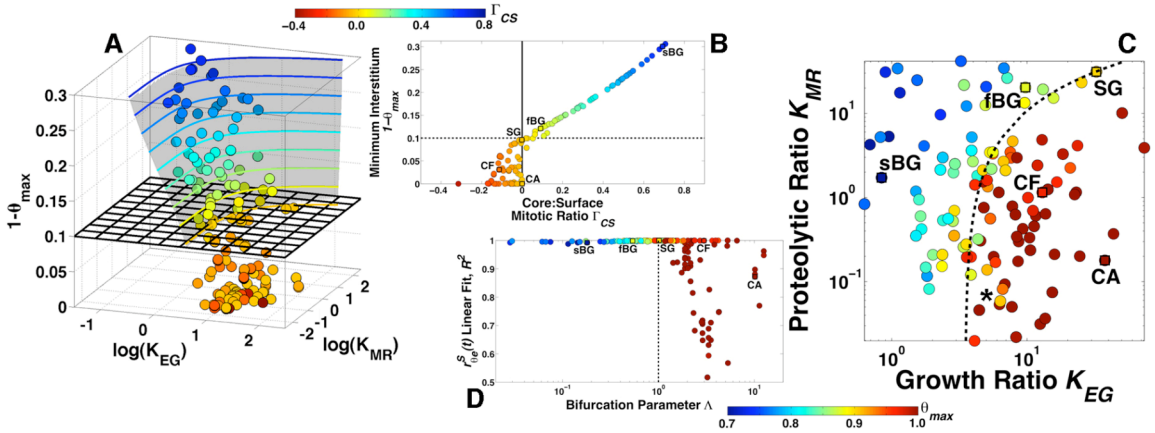

Figure 25. Morphogenetic bifurcation surface in parameter space. Data correspond to 1 day except for CA models that are displayed in A-C until time of encapsulation. (A) Smooth surface describes the relations among the non-dimensional ratios for epithelium growth and mesenchyme removal K_{EG} and K_{MR}, the core:surface mitotic ratio $\Gamma_{CS} \equiv R_{EG}^C / R_{EG}^S$ and the minimum observed interstitial fraction $1-\theta_{max}$. Bifurcation at $\theta_C = 90\%$ (equivalent to $1-\theta_{max} = 10\%$ and corresponding to SG models with $\Gamma_{CS} = 0$) demarcates between subconfluent models with $\Gamma_{CS} > 0$ (BG) and superconfluent models with $\Gamma_{CS} < 0$ (CF and CA). (B) The relationship between $1-\theta_{max}$ and Γ_{CS} for subconfluent models is linear ($R^2 = 0.98$). (C) The bifurcation in A is fitted by a smooth function $\Lambda = K_{EG} \Big/ \exp\left[a + b \cdot \left(K_{MR}\right)^c\right]$ in the projected $\left(K_{EG}, K_{MR}\right)$ plane ($a = 1.2$, $b = 0.2$, $c = 0.7$) where $\Lambda < 1$ for BG, $\Lambda = 1$ for SG, and $\Lambda > 1$ for CF and CA. Asterisk ($*$) shows a hypothetical encapsulating system; one could experimentally block its encapsulation by either dramatically increasing K_{MR} or slightly reducing K_{EG}. Square markers correspond to examples from Figure 24. (D) The bifurcation parameter Λ discriminates between subconfluent models with constant $V_{\theta e}^S$ (BG, $\Lambda < 1$, $\theta_{max} < \theta_C$, $R^2 = 1$ for $r_{\theta e}^S(t)$ linear in time) and superconfluent encapsulation models with bilinear spheroid radius $r_{\theta e}^S(t)$ (CF and CA, $\Lambda > 1$, $\theta_{max} > \theta_C$, $R^2 < 1$ for $r_{\theta e}^S(t)$ nonlinear in time) as depicted in Figure 24. Colors shown for subconfluent models in A (colormap: Γ_{CS}) and C (colormap: θ_{max}) are equivalent as a result of the linear correspondence shown in B between Γ_{CS} and θ_{max}.

We previously showed how swelling pressure creates capsules around a growing epithelium [206]. In this paper we see how proteases can prevent encapsulation. Note that the mere presence of proteases is not sufficient. The protease activity K_{MR} must be sufficiently large relative to the epithelial growth K_{EG}. It is also worth noting that crossing the bifurcation – going from steady growth to capsule formation or vice-versa – may be easier or harder depending on where in parameter space a system begins. For example, the hypothetical system represented by the * in Figure 25C will form a capsule because it has $\Lambda > 1$. A 50% reduction in K_{EG} will prevent capsule formation, yet even a 10-fold increase in K_{MR} would not suffice to prevent encapsulation. The slope of the bifurcation curve implies that inducing a qualitative change in the system – crossing the bifurcation – is experimentally harder to achieve by changing growth factor or protease kinetics alone. We see this in experiments in which either (a) GF signaling mechanisms or (b) protease activity levels are modified (by gene knock-out, silencing or amplification), but typically not both (a) and (b). Single-variable manipulations mostly modulate the rates of morphogenesis but rarely change the fundamental morphogenetic outcomes.

Specificity and relative importance of model components. The model is constructed from a simplified perspective, with the aim of constructing a minimal mechanism of growth regulation by transport. Tissue mechanical properties do vary over lineage and time, but we focus on a short enough time scale to ignore such changes. The numerous regulatory molecules are lumped into generic "growth factor" and "protease" activities. Real systems are more complex at the cellular level but can for practical purposes be considered in the simplified context of *net* effects. For example, if multiple growth factors are at work, doubling the *effective* "growth factor activity" may require more than doubling a *specific*

growth factor. It is well established that MMPs (matrix metalloproteinases) and their regulators regulate epithelial growth. MMPs are regulated by GF and TIMP (tissue inhibitors of metalloproteinases). Timp-1-reduced mammary epithelia, with greater MMP activity, grew 55% faster than control, and rTimp-1 elevation inhibited growth [207]. Our simplified (parsimonious) model allows a quantitative interpretation of these experiments and the effect of the experimental factors on the net mesenchyme removal rate K_{MR}.

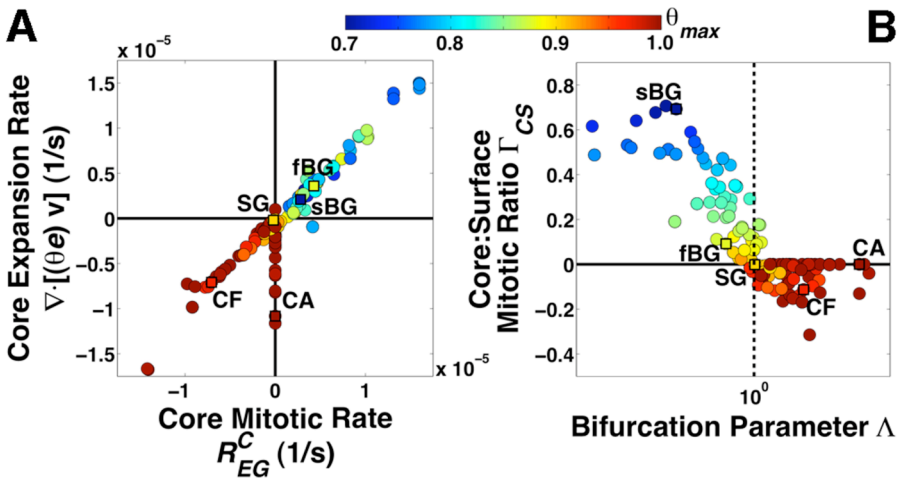

Figure 26. Growth and expansion of a spheroid distinguish between steady growth and encapsulation mechanics. Square markers correspond to examples from Figure 24. (A) Measured at the core, epithelium expansion $\nabla\cdot(\theta e\mathbf{v})$ matches the mitotic rate R_{EG}^{C} during steady bulk growth (BG); surface growth (SG) models show no growth or epithelium flux at the core; capsule formation (CF) both breaks down and compresses core until encapsulation halts transport and growth, when θ reaches 100% (CA). Superconfluent models (CF, CA) have $R_{EG}^{C} \le 0$ as a result of the logistic form of growth (carrying capacity defined as the confluence limit $\theta_c = 90\%$). (B) The core:surface mitotic ratio $\Gamma_{CS} \equiv R_{EG}^{C} / R_{EG}^{S}$ discriminates between BG and SG. The transition between BG and SG corresponds to decreasing growth rate at the spheroid core. All observations from SG models result exclusively from maximal growth at the surface ($\Gamma_{CS} = 0$, $R_{EG}^{S} > 0$). All data corresponds to 1 day, except for CA models halted at time of encapsulation.

It is not an essential assumption of our model that the growth factor be bound, released by protease, and subsequently diffuse and advect. A variety of mechanisms can lead to the same morphogenetic gradients [208]. Insoluble growth factors external to the epithelium can

be transported into the tissue by being solubilized, vesiculated, probed by filopodia, transported on a motile cell, or induced in a relay [183].

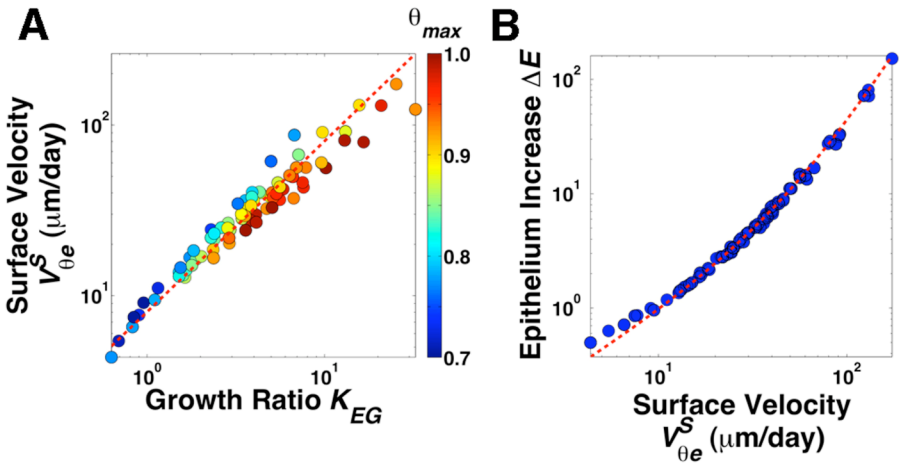

Figure 27. Surface velocity and volumetric change during steady spheroid growth. (A) The surface velocity is linear in the growth ratio $V^S_{\theta e} = p \cdot K_{EG}$ (p = 8.1 μm/day, R^2 = 0.93) during steady growth (BG, SG and CF models). CA models yield piecewise $V^S_{\theta e}$ (Figure 24 and Figure 25D) that halt at complete encapsulation ($\theta_{\max} = 100\%$). (B) The total cellular content of a growing spheroid, represented in terms of the volumetric change ΔE, increases with a relationship characteristic of a sphere dilating at constant epithelial surface velocity $V^S_{\theta e}$ (dotted red line, R^2 = 0.99). All data corresponds to 1 day.

The proteases promote growth in three ways. First, the GF cannot stimulate the epithelium until the protease releases them from the ECM. Second, dissolution of the ECM creates more interstitial material, which is then available for conversion to cells. Third, dissolution of the ECM raises the hydraulic conductivity and enhances transport of raw materials into the growing tissue.

The epithelial swelling pressure is critical to growth in two ways. First, a tissue cannot grow volumetrically without transport of new material into its interior; this requires the swelling pressure. Second, transport of soluble growth factors into the epithelium is by advection and diffusion. In this context, diffusion is a much slower process than advection, which is why the ligand diffusion coefficient D_G, varied over 4 orders of magnitude in the

model, does not affect either the speed of growth or the tendency to encapsulate. The fluid flow is the product of the hydraulic conductivity and the pressure gradient; the epithelial swelling pressure regulates the latter.

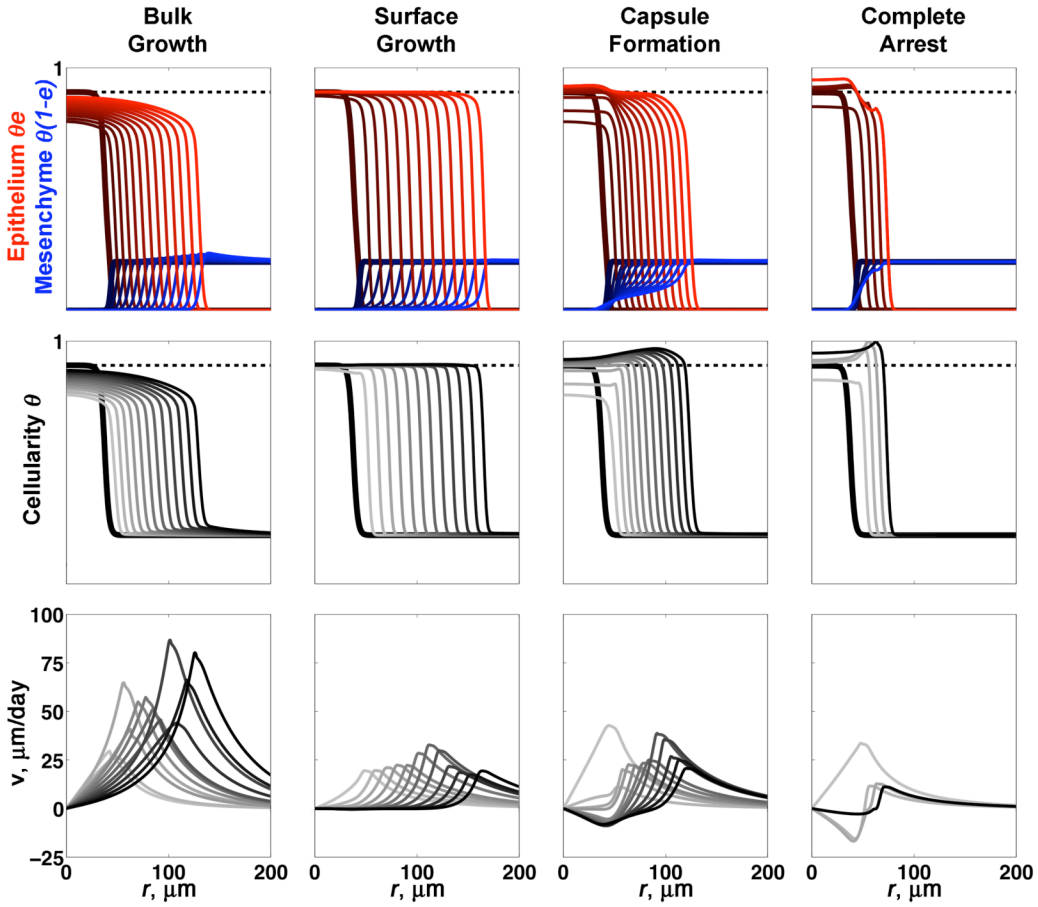

Figure 28. Expanded outputs of model examples from Figure 24. Epithelium (top, red), mesenchyme (top, blue), cellularity (middle) and cell phase velocity v (bottom). In Surface Growth regime, epithelila growth matches mesenchyme proteolysis. Capsule Formation and subsequent Complete Arrest regimes have epithelium growth overriding mesenchyme proteolysis, leading to localized densification at the interface. This densification imposes physical constraints on the epithelium, which in turn exhibits backward motion (v<0) and further condensation, driving cellularity above the epithelium confluence limit. Since backward cell motion requires forward aqueous transport (w>0) this encapsulation mechanism is irreversible; Capsule Formation leads to Complete Arrest. Solid curve: initial conditions (same for all models, as described in Figure 23); dashed reference line: confluence limit $\theta = \theta_C = 90\%$. Curve spacing 2 hours; all plots show 1 day except CA halted at arrest (thick curve).

Systems that are at the bifurcation grow only at their surface, even if their interior has some interstitial space. Because a bifurcation marks a curve in a larger space, a system at a bifurcation will be rare, unless it has been specifically control-engineered to be there. Therefore, spheroids exhibiting steady surface growth and no encapsulation must have some feature not included in our model. For example, we make the point that volumetric growth cannot occur unless there is both interstitial space to permit transport and a swelling pressure to drive it. Systems lacking these features can only grow at the surface, like an evolutionarily primitive stromatolite.

7.6. CONCLUSIONS

The major finding of this study is the surprisingly simple bifurcation criterion that distinguishes between steady bulk volumetric epithelial growth and capsule-limited growth. Our bifurcation parameter Λ determines whether a spheroid grows indefinitely or halts when capsule completion blocks transport. Although the model was constructed with a large number of parameters (Table 8), the bifurcation parameter Λ delineates regions of a 2-dimensional subset of the 8-dimensional sampled parameter space. The two key parameters are the nondimensional ratios $K_{EG} \equiv \frac{k_l^B S \tau}{T}$ and $K_{MR} \equiv \frac{k_{cat}^N C \tau}{F}$ governing epithelial growth and mesenchyme removal. Other factors that we examined were unimportant in distinguishing bulk growth from capsule formation; for example, tissue permeability and viscosity were each varied over 2-3 orders of magnitude without affecting the bifurcation.

In many contexts such as tissue engineering, spheroid growth rate is important [209]. The speed of growth in our model spheroids was found to be dependent only on K_{EG}, and is linear in K_{EG}. The implications for tissue engineering are clear: to grow tissue rapidly, increase any factor that increases K_{EG}. However, if K_{EG} is above the bifurcation criterion, the

growth will be rapid only until encapsulation, when it will cease. Sustainable rapid growth requires not just large K_{EG} but sufficiently large K_{MR} to prevent encapsulation. Thus our study reveals an interesting paradox: increasing growth factor supply speeds up growth, but too much can *arrest* growth, by outrunning mesenchyme removal. Our results provide quantitative criteria for these regulatory mechanisms.

7.7. APPENDIX: MODEL DETAILS

7.7.1. Boundary conditions

The core of the spheroid has symmetry BC, with hydrostatic pressure set to 0. The outside of the mesenchyme is considered to be sufficiently far away from the area of growth that we set its BC to zero normal transport.

7.7.2. Numerical methods

PDE were solved by the finite element method using Comsol 3.5. Because of instabilities inherent in the diffuse interface method, we used a minimal numerical isotropic diffusion to stabilize the algorithm. MATLAB was used for parameter space sampling, postprocessing, graphics, and statistics.

7.7.3. Nondimensional model

The complete model describes an equation system for volume continuity, force balance and conservation of transmembrane proteases, active soluble ligands and tissue phases. A nondimensional version allows us to probe multidimensional parameter space effectively. Using characteristic length L, time τ and viscosity μ, with $\bar{P} = P \cdot \tau / \mu$ and $\bar{\mathbf{v}} = \mathbf{v} \cdot \tau / L$, the nondimensional system is

$$\bar{\nabla} \cdot \left(\theta \bar{\mathbf{v}} + \left(1 - \theta\right) \bar{\mathbf{w}} \right) = 0$$

$$\bar{\nabla}\cdot\left(\theta\left(2\bar{\mathbf{E}}_c-\frac{2}{3}\left(\bar{\nabla}\cdot\bar{\mathbf{v}}\right)\mathbf{I}\right)\right)-\alpha\left(\frac{\theta}{1-\theta}\right)\left(\bar{\mathbf{v}}-\bar{\mathbf{w}}\right)=\theta\bar{\nabla}\bar{P}+\beta\,\bar{\nabla}\left(\theta\cdot\left(\frac{\theta e-\theta_\sigma}{\theta_C-\theta_\sigma}\right)^2\cdot\Omega\left(\theta e-\theta_\sigma\right)\right)$$

$$\alpha\left(\frac{\theta}{1-\theta}\right)\left(\bar{\mathbf{v}}-\bar{\mathbf{w}}\right)=\left(1-\theta\right)\bar{\nabla}\bar{P}+\beta\,\bar{\nabla}\left(\left(1-\theta\right)\cdot\left(\frac{\theta e-\theta_\sigma}{\theta_C-\theta_\sigma}\right)^2\cdot\Omega\left(\theta e-\theta_\sigma\right)\right)$$

$$\frac{\partial}{\partial\bar{t}}m+\bar{\nabla}\cdot\left(m\bar{\mathbf{v}}\right)=K_{A,m}\cdot\left(\theta e-m\right)\cdot\theta\left(1-e\right)\cdot\Omega\left(m\right)-K_{I,m}\cdot m$$

$$\frac{\partial}{\partial\bar{t}}g+\bar{\nabla}\cdot\left(g\bar{\mathbf{w}}\right)=\xi\,\bar{\nabla}^2 g+K_{A,g}\cdot m\cdot\theta\left(1-e\right)-K_{I,g}\left(\frac{g}{\left(S/K_D^R\right)\cdot g+\left(1-\theta\right)}\right)\cdot\theta e$$

$$\frac{\partial}{\partial\bar{t}}\theta+\bar{\nabla}\cdot\left(\theta\bar{\mathbf{v}}\right)=K_{EG}\left(\left(1-\theta\right)-g\right)\cdot\left(\frac{\theta e}{1-\theta}\right)\cdot\left(1-\frac{\theta e}{\theta_C}\right)-K_{MR}\cdot m\cdot\theta\left(1-e\right)$$

$$\frac{\partial}{\partial\bar{t}}\theta e+\bar{\nabla}\cdot\left(\theta e\bar{\mathbf{v}}\right)=K_{EG}\left(\left(1-\theta\right)-g\right)\cdot\left(\frac{\theta e}{1-\theta}\right)\cdot\left(1-\frac{\theta e}{\theta_C}\right)$$

using normalized active ligand $g=\left(G/S\right)\cdot\left(1-\theta\right)$ for $0\le G\le S$ and normalized active protease $m=\left(N/C\right)\cdot\theta e$ for $0\le N\le C$. Nondimensional parameters α, β, ξ, $K_{A,m}$, $K_{I,m}$, $K_{I,g}$, K_{EG} and $K_{MR}=K_{A,g}$ are as defined in Table 9.

7.7.4. Parameter ranges and sampling

Multivariate studies relate model results to the parameters that describe the model. Parameter values must lie within ranges justified by experimental data. The study should also minimize bias in the choice of these values. Random sampling reduces bias in parameter value selection. There are eight characteristic nondimensional ratios describing the equation system: α, β, ξ, $K_{A,m}$, $K_{I,m}$, $K_{I,g}$, K_{EG} and K_{MR} (Table 3). We selected six dimensional parameters for sampling that allow unique and independent sampling of six of these nondimensional ratios; we chose two additional dimensional parameters that sample each of the remaining ratios α and K_{MR} separately in exclusive combination with only one of the

other sampling parameters. We used simple random sampling without repetition for each and all of these eight parameters independently to define multiple unique models with respect to the nondimensionalized system. Molecular kinetics were considered to vary logarithmically, e.g. ligand diffusivity D_G spans 0.1 – 100 $\mu m^2/s$ [174, 180, 183].

Fixed model parameters used values in agreement with experimental measurements (Table 8). Values for parameters sampled in the multivariate study stay within a few orders of magnitude of their reported measurements.

- Hydraulic conductivity of various tissues has been measured (reviewed in [179]), and can range from 10^{-4} - 1 mm^2/Pa-s, depending on tissue type [179, 192, 206]. It is established that hydraulic conductivity is generally higher in neoplastic than in normal tissues [192]. We have no relevant estimates for specific embryonic tissues, other than to surmise that embryonic tissues, like neoplastic tissues that are also rapidly growing, likely have higher hydraulic conductivity than mature tissues.
- Many embryonic tissues have viscosity in the range 10^5-10^7 Poise [159, 176-178, 210]; 5- and 6-day chick liver, heart, and retina aggregates relax at 0.1 MPoise [159]; embryonic limb bud [159] and pigmented epithelial tissue [176] at 1 MPoise; and 5-day chick cardiac cushion at 10 MPoise [177].
- Interstitial pressure h_0 has been measured in tumors to be in the range ~ 0 - 10 kPa [191]; subcutaneous swelling pressure in mammals and birds has been measured at ~10 kPa [193]; inflammatory swelling pressure ranges from 0.1 - 18 kPa [195]; blood plasma has an oncotic pressure of about 3 kPa. Swelling pressure has not been measured in embryonic tissues; we assume it to be at the lower end of these ranges.

- A pressure of 1 kPa with a viscosity of 1 MPoise gives a relaxation time scale of 1-2 minutes. Since the morphogenetic time scale is 8-72 hours (see above), the Deborah number is 10^{-2} - 10^{-1}, and we are justified in using the approximation of a viscous fluid.

7.7.5. Derived quantities

We calculated the total volume occupied by the epithelial fraction by integrating over the model domain. By tracking the epithelial surface $r_{\theta e}^{S}(t)$ as the location of the reference fraction $\theta_c/2$ in the epithelial front over time, we determined the growth velocity $V_{\theta e}^{S}$.

Table 9. Representative nondimensional ratios

Definition	Nondimensional ratio	Sampled input parameter(s)
Mechanics and Transport		
interphase drag	$\alpha = \frac{L^2}{\mu \mathrm{K}_0}$	μ, K_0
swelling pressure	$\beta = \frac{h_0 \tau}{\mu}$	μ
diffusivity	$\xi = \frac{D_G \tau}{L^2}$	D_G
Dynamics		
protease activation (substrate binding)	$K_{A,m} = k_{cat}^N \frac{F\tau}{K_M^N}$	k_{cat}^N
protease internalization (half-life in latency)	$K_{I,m} = k_H^N \frac{K_M^N \tau}{F}$	k_H^N
mesenchyme removal, ligand activation[25]	$K_{MR} = K_{A,g} = k_{cat}^N \frac{C\tau}{F}$	k_{cat}^N, C
bound ligand internalization (ligand-receptor complex)	$K_{I,g} = k_I^B \frac{T\tau}{K_D^R}$	K_D^R
epithelium growth	$K_{EG} = k_I^B \frac{S\tau}{T}$	S

[25] Nondimensionalization shows that K_{MR} and $K_{A,g}$ are equivalent; i.e. these events are simultaneous. This is because in the model both mesenchyme removal and ligand activation are driven by the same proteolytic reaction.

7.7.6. Statistical regression

Radial growth velocity was fitted to a linear function with $R^2 = 0.98$ except for models that ran past complete encapsulation (Figure 24 and Figure 25D). The bifurcation surface (Figure 25A and Figure 25C) was fitted using a nonlinear least squares regression of an exponential function of transformed data for $Y = a_\theta + b \cdot X^c$ ($Y = \log K_{EG}$, $X = \log K_{MR}$). The value of a_θ is dependent on the level of $\theta_{\max} = \theta$ with constant *b* and *c* for all values of $\theta_{\max}$. The bifurcation parameter Λ defines the bifurcation surface at $\theta_{\max} = 90\%$, which corresponds to SG.

CHAPTER 8. DISCUSSION

8.1. ORIGIN OF MECHANICAL STIMULUS IN LIVER

We can deduce the types of forces a tissue experiences *in vivo* from the anatomical placement of the tissue. It is important to identify these forces because their effects on tissues can influence differentiation and physiology. We can understand which types of mechanical forces influence cells by understanding the origin of these mechanical forces and their relationship with tissue physiology.

The adult human liver is a soft intraperitoneal organ. It is lined by peritoneum on multiple surfaces. The peritoneal lining helps fix the liver in place within the abdominal cavity while false ligaments – made of peritoneum folds – attach the liver to the diaphragm, the anterior abdominal wall and the muscular walls of abdominal viscera that maintain continuous contractile tone [116]. During development (3 to 4 weeks after fertilization in humans), liver arises as a hollow diverticulum from the ventral region of the endodermal foregut that grows underneath the septum transversum. Interactions between the hepatic diverticulum and splanchnopleural mesenchyme at the inferior surface of the septum transversum give rise to the mature liver stroma and parenchyma, respectively [211].

Liver experiences compression from the diaphragm during the breathing cycle [212-214]. These cyclic deformations are one element of normal physiological function that introduces mechanical forces to liver cells. Also, liver is a secretory organ with fenestrated microvascularity (or endothelial sinusoids), which implies that shear effects, pressure

gradients and other effects of fluid flow could participate in liver function. One hypothetical outcome of changing ECM chemistries across the hepatic maturational gradient is microenvironments with varying rigidities; this variation in local mechanics is biologically relevant – e.g. matrix rigidity is a mechanical property that induces lineage specification in mesenchymal stem cells [47]. In sum, we can surmise that differentiation in hepatic progenitors depends on at least two mechanical influences: gradients in ECM composition within the maturational gradient that establish gradients in tissue mechanics, and shear effects on cells from fluid flow across hepatic tissues.

Liver arises during development as an early endodermal derivative. It has vital functions that regulate homeostasis, including bile secretion and toxin removal. Homeostatic balance in liver is a physiological consequence of maturational biology, which controls tissue formation, regeneration and epithelial-mesenchymal interactions across lineages [1, 114]. Cell lineages are concomitant with characteristic matrix compositions and each maturational stage must contain specific epithelial and mesenchymal cell lineages in an appropriate environment for normal function. In fact, epithelial metaplasias originate from toxic insults or diseases that disturb local signaling profiles in epithelial organs [114]. Moreover, cell survival and proliferation improve with ectopic cell scaffolding in decellularized biomatrices in which lineage specification agrees with biomatrix chemistry [23, 215-217].

8.2. TRENDS IN TISSUE MECHANICS RESEARCH ON DEVELOPING TISSUES

Research on embryonic mechanics has become increasingly important to developmental biologists and the field of stem cell biology because embryonic mechanisms occur through biochemical activity in controlled physical environments [157]. On the one hand, developmental biology studies processes by which cells and tissues, originating from the

embryo, evolve towards adult function. These processes are complex, strictly controlled in time and space and, most notably, conserved across multiple species as a result of evolution. In other words, the role of developmental biology is to identify physiological factors directing biochemical responses that control embryonic mechanisms. On the other hand, the role of tissue mechanics is both to determine how forces modulate the physical context in which physiological factors perform biological functions, and also to actuate those forces. These two types of mechanisms, biochemical signaling and tissue mechanics, act in coordination at all stages of development – including the developing embryo – and determine how tissues mature and acquire specialized function.

We can use lineage specification processes in strategies for tissue regeneration in adult organs if we understand the mechanisms underlying differentiation control, including mechanotransduction, from the onset of development and throughout their homeostatic control in postnatal function and disease. In order to analyze lineage specification under a mechanotransduction viewpoint, we first need to recognize that cells, including embryonic stem cells, are mechanically sensitive in all stages of development because they possess mechanosensitive organelles such as primary cilia and gated ionic channels [218]. In the blastocyst, nodal cilia produce asymmetric flow across the ventral node, which is responsible for establishing left-right asymmetry during early body plan establishment. Other non-motile primary cilia localize along the paths of the nodal flow and sense it, which results in differential expression patterns of early morphogens from, among others, the Hh signaling pathway [219]. All these events lead to lineage specification mechanisms poorly understood under mechanical terms. Therefore, we need to outline differentiation principles within mechanical frameworks in order to understand maturation mechanisms in terms of tissue

mechanics. This is especially pressing for endodermal tissues, whose function is not traditionally interpreted in terms of mechanical action.

Research on embryonic tissue mechanics advances in parallel with the advent of technologies able to test at appropriate scales of cellular and tissue function. Research on tissue mechanics of embryos and stem cells has revealed, for example, that differentiation is a stiffness-dependent mechanism [47] accompanied by loss of mechanical compliance in cells [196], and that embryos exhibit phase ordering that parallels behavior in liquid mixtures [159, 160, 176-178, 190, 197, 198]. Differentiation patterns during embryonic development arise, in part, from induction of active flow by mechanical organelles like cilia [219]. In addition, we also know tissue formation and maintenance depends on controlled mechanisms of interstitial flow throughout life [179].

In the recent past, research on human developmental biomechanics had limited access to embryonic tissues. In fact, most developmental biology research has been performed in model species, which includes non-mammalian species (e.g zebrafish) and invertebrates (e.g. roundworm *C. elegans*). Induced pluripotent stem (iPS) cells provide an alternate source for human embryonic-like cells that can be used to advance this type of research. Since their invention, iPS cells have redefined our understanding of differentiation as a unidirectional process by showing, for example, that a handful of genes suffice to reconstitute pluripotency in somatic cells. This process, usually performed in human foreskin fibroblasts and also possible with other primary cells, consists of retroviral transfection of Oct3/4, Sox2 and either Nanog and Lin28 [220] or c-Myc and Klf4. The current belief is that transfecting these genes in somatic cells induces pluripotency because they participate in global demethylation of the chromatin, which propels the genome into a pluripotent de-

differentiated state. Transfected somatic cells, when fully developed into iPS cells, exhibit trademark characteristics of ES cells such as teratoma formation, asymmetric division and differentiation into all germlines [221]. These characteristics help developmental biologists because iPS cells are more accessible than ES cells as experimental models.

Although many of the biochemical mechanisms in ES and iPS cells match with remarkable precision, there are some differences between them. First of all, iPS cells originate from retroviral transfection of pluripotency genes, thus inducing genomic alterations in iPS cells that ES cells do not share. In addition, homogeneity within iPS populations depends not only on successful transfection of all pluripotency genes in all cells, but also on cells successfully rescuing a functional pluripotent state beyond gene expression. Therefore, variations in pluripotency potential of iPS cells indicate that the process requires further optimization, including improved iPS cell isolation in terms of functional requirements like EpCAM and E-cadherin expression, and shows that degrees of global demethylation could vary across iPS cell preparations [161]. In comparison, cells from a single ES cell source are defined by their homogeneous pluripotency and equivalent genomic characteristics [221].

As long as we recognize functional differences between iPS cells and ES cells *a priori*, the iPS model can enhance our understanding of embryonic development with respect to mechanotransduction. To our knowledge, there is only a handful of electrophysiological studies on iPS cell function that explicitly search for differences in mechanical and physiological mechanisms between ES cells and iPS cells. Those studies found only minimal distinctions in electrophysiological activity [222, 223]. For that reason alone, and without further evidence, we can only assume that iPS cells model ES cell responses to mechanical

stimuli that replicate mechanotransduction mechanisms in embryonic stages with acceptable homology.

8.3. ALTERNATIVE MECHANOTRANSDUCTION AMPLIFICATION SYSTEMS

Mechanotransduction signaling pathways in cells operate as amplification systems. By definition, an amplification system requires transduction mechanisms that relay small stimuli for interpretation with high efficiency and fidelity. In the context of cellular signaling, mechanotransduction complies with three amplification requirements: first, transduction traverses along interconnected "paths" using adaptable and networked stable structures; second, transduction modes are highly specific to avoid loss of fidelity; and third, conversion of physical stimuli into biological activity generates global responses as a result of networking.

Cells from soft organs interpret small changes in their mechanical state through mechanotransduction in organelles with sensorial amplification machinery [111]. For example, cells can transduce local shear effects into dense signaling with primary cilia that increase flow sensitivity. When primary cilia are stimulated, they use polarized signal transduction pathways residing within them to transmit signals down the cytoskeleton and into the nucleus, triggering gene expression in cells. To ensure amplification of shear effects, cells enrich mechanotransduction signaling machinery (such as gated channels and cell receptors) within primary cilia; in addition, primary cilia machinery uses shuttling mechanisms with motor proteins that ensure non-diffusible signal trafficking to the nucleus, which confers specificity, fidelity and efficiency to signal transduction in primary cilia [53]. The signaling mechanisms in primary cilia have physiological relevance, as defective cilia characterize a large array of diseases known as ciliopathies [224].

The determining feature of primary cilia function is the molecular ultrastructure at their base, which consists of the axoneme, the centriole and the alar shields. These elements only allow passage of cytoplasmic proteins under 10 kDa in size when assembled in to primary cilia. That space restriction eliminates the possibility of protein synthesis within cilia [53]. To operate, primary cilia acquire proteins and molecular machinery with an intraflagellar transport (IFT) mechanism that uses molecular rafts (called IFT proteins). IFT proteins move along the axoneme using motor proteins such as kinesin II and cytoplasmic dyneins. Kinesin II moves in the minus-to-plus (anterograde) direction with respect to the basal body of the centriole, while cytoplasmic dyneins move in the opposite (retrograde) direction [225-227]. This transport machinery of kinesin II and cytoplasmic dyneins effectively cargoes proteins along primary cilia at speeds of 2 to 4 μm/s, which are fast at the intracellular scale since ordinary lengths of primary cilia are between 5 μm *in vivo* up to 30 μm in culture [53].

Cells project primary cilia into luminal spaces in tissues. Upon bending, primary cilia trigger mechanosensing responses that respond to cilia deformation in the presence of flow. In cultured Madin-Darby canine kidney (MDCK) cells, internal Ca^{2+} concentration increases by both deforming cilia with micropipette aspiration or increasing perfusate flow rate, a response absent from cells without primary cilia after chloral hydrate treatment [228, 229]. Mechanosensation in hepatic cholangiocytes results from bending by activation of polycystin-1 (PC-1, a cell surface receptor) and polycystin-2 (PC-2, a Ca^{2+} channel) during Ca^{2+} signaling, which leads to cAMP signaling suppression through Ca^{2+}-dependent adenylyl cyclase 6 (AC6) inhibition [230].

Research on cholangiocytes from intrahepatic biliary ducts reveals that the proteins enriched in cilia also allow primary cilia to operate as osmosensors and chemosensors.

Osmosensation in cholangiocytes results from hypotonic activation of TRPV4 in anisosmotic conditions. TRPV4 is a Ca^{2+}-permeable channel expressed in cilia that induces ATP release and bicarbonate secretion, thus increasing bile flow [231]. For chemosensation, primary cilia use purinergic receptors, mainly ciliary P2Y12, that detect biliary nucleotides and inhibit cAMP signaling in a cilia-dependent fashion [232].

Nodal cilia are an intermediate specialized version of primary cilia found in the blastocyst that do not possess the central microtubule pair but conserve the remaining motile components [53]. This alternate conformation results in propeller motion that induces leftward fluid flow from the ventral node (thus the name nodal flow), distributes secreted and vesiculated morphogens preferentially, and determines left-right body asymmetry during development [219].

Cilia respond to flow, but this function is not exclusive of cilia. In fact, normal arterial flow can disassemble cilia in endothelial cells [233]. In this case, response to flow is a result of drastic cytoskeletal rearrangements and microfilament reorganization in cells. These structural reorganization in cells parallels observations during the formation of mitotic spindles that are ordinarily preceded by ciliary resorption [234]. Another cellular component involved in mechanotransduction is the plasma membrane. Flow forces on the plasma membrane induce purinergic signaling through P2 receptors in cells without primary cilia [45]. These cells can still maintain purinergic tone because flow forces deform their plasma membrane and activate ionic exchange through mechanically gated ion channels. Ionic channels opened by straining the plasma membrane explain how cAMP signaling responds to mechanical forces to initiate secretory functions and regulate the cell cycle through protein kinase A (PKA). Under these mechanical conditions, other secondary messengers like Ca^{2+}

can respond to mechanical stimuli and initiate signaling cascades equivalent to those induced by neurotransmitters or hormones [235, 236].

Effects of mechanical forces in stem cells also include electrophysiological responses. Ion gated channels exist in cells at all stages of development. Recent evidence suggests that the profile of ionic channels that cells use varies across lineage specification. Comparisons between embryonic (ES), induced pluripotent (iPS), mesenchymal stem cells (MSCs) and somatic cells show that ES and iPS cells act exclusively through K+ channels, without voltage-gated Na+ or Ca2+ currents, and with marked preference for proliferation over metabolic effects [222, 223].

Matrix gradients in tissues provide, in addition to a specialized mechanical context, a physical indicator for orderly maturational progression that cells establish during development and follow thereafter. In addition to matrix gradients within tissues, cross-talk between cells at different lineage stages maintains pluripotency of progenitors *in vivo* through feedback loops. Cells can monitor these feedback loops along specific histological routes in healthy conditions. Conversely, diseases that perturb the integrity of these feedback loops activate differentiation and expansion of determined stem cells. Because maturational gradients span across tissues, homeostatic signals must reach all cells that communicate through feedback loops using transport mechanisms besides diffusion. Bile is an example of a physiological carrier of homeostatic signals in adult liver [1].

Broadly speaking, cells require specific machinery to sustain forces. Cells can regulate their functions through soluble signaling, but cell attachment and compliance to external forces also affect their survival. Mechanical adaptation of cells includes cytoskeletal reorganization and ionic exchange that respond to forces via stress-sensitive organelles.

Some of these organelles include integrin receptors and gated ionic channels that are directly activated by distensions in the plasma membrane and tension on focal complexes [49, 111]. Some cells, under external forces, reorganize their intracellular function to acquire mechanical competence. If we accept that these intracellular changes could manifest as lineage specification towards more mechanically resistant cell types, then we can interpret differentiation as a cellular mechanism aimed towards adaptation of cells to their microenvironment. In fact, cell mechanosensors can regulate secondary signaling pathways with roles in differentiation, such as specific Ca^{2+} concentrations that dictate growth or differentiation in epithelial cells [1].

Mechanical competency of cells would suggest that their mechanical compliance matches rigidity gradients in tissues and correlates with lineage specification. In other words, cells could acquire more rigid configurations as they differentiate. This is true in ES cells – differentiation plasticity matches mechanical plasticity – in which cyclic mechanical stress leads to differentiation. Cyclic mechanical stress promotes spreading, downregulates Oct3/4 expression and induces a ten-fold increase in ES cell rigidity through pathways controlling cell shape and proliferation [196]. Other experiments show that embryonic cell sorting obeys differential adhesion properties that correlate with the cell-cortex tension of germline cells [48]. These results imply that stem cells might be exquisitely susceptible to mechanical induction. Hence, mechanical forces can bias lineage specification to preferential fates, in combination with signaling, by preparing stem cells to comply with mechanical functions that their differentiated state requires [112, 237].

Mechanical plasticity of stem cells suggests that deviations from canonical forcing can alter morphogenesis and differentiation, whether through mechanotransduction or through

perturbations in transport. This happens with Twist, a powerful morphogen that participates in β-catenin signaling in fruit flies, which regulates mesoderm invagination during gastrulation and midgut differentiation. Stomodeal cells in fruit fly gastrula, after ablation of the neighboring cells that compress them *in vivo*, recover Twist expression with controlled deformations induced by indentation or magnetic forcing [238, 239]. In another remarkable example, experiments that reverse nodal flow in mouse embryos perturb endogenous expression patterns of signals during body axis planning, such as Shh and retinoic acid, which leads to *situs inversus* [219, 240].

8.4. SIGNALING WITH MECHANICAL BASIS IN STEM CELL BIOLOGY

Mechanical interpretation of signaling during organ development links endoderm differentiation with maintenance and homeostatic control of its derivatives in adult stages. This approach to stem cell biology could help control cell differentiation in tissue engineering applications through reproducible mechanical stimuli. Successful translational medicine strategies using stem cell biology will depend on biochemical signaling in appropriate physical environments, which underlines the role of tissue mechanics in therapeutic applications. We can surmise which developmental mechanisms also respond to mechanical effects on cells by inspecting which mechanisms use signaling involved in mechanotransduction. The analysis below focuses on endoderm progression because, in comparison to ectodermal and mesodermal derivatives, there have been few efforts to study endodermal derivatives under mechanical perspectives.

An obvious mechanical process during development – and the signature step at the beginning of gastrulation – is formation of the primitive streak on the posterior surface of the epiblast. Within the primitive streak, mesendoderm regulates genetic expression of Foxa2,

Sox17 and PDGFRα, among others [60]. Progression of the definitive endoderm and its derivatives requires Sox17, which has important roles in soft organ development [241]. At this point in development, a delicate concert of endogenous signals demarcates regions along the endodermal gut that generate each of the organs in the gastrointestinal tract. Activin/Nodal signaling in ES cells regulates Nanog expression that competes for RSmads with Smad4. FGF2 signals also target RSmads, which makes Activin/Nodal signaling a mechanism that modulates endodermal progression through competition [242]. Later in endodermal progression, FGF2 (but also FGF4) induces proliferation of anterior definitive endoderm (ADE) cells that express Hex and Cxcr4; FGF signaling also increases expression of Foxa2 and Sox17 in ADE cells. This expression profile in ADE cells suggests that they are differentiated endodermal progenitors for hepatic and pancreatic fates. These signaling mechanisms, in conjunction, determine differentiation fates in the anterior-posterior direction within the definitive endoderm [243]. These types of competition mechanisms in signaling are prominent in neuroectoderm, namely the notochord, and help tissues adjacent to endoderm in regulating endodermal differentiation [60].

Developing gut endoderm expresses Shh, suggesting that Shh participates in activation of the Activin-FGF signaling concert within the notochord. After gastrulation, definitive endoderm with differential Shh expression flanks the notochord and interacts with the surrounding neuroectoderm. The regions with positive Shh expression eventually develop into duodenum and stomach in a cranio-caudal orientation [60]. Because some of the most important genetic targets of Hh signaling are ligands of the TGF-β family that participate in Activin/Nodal signaling [57], we surmise that Hh signaling also determines ADE anterior-

posterior orientation, in addition to establishing left-right asymmetry and cranio-caudal differential expression [219].

Hh signaling participates in body plan establishment by regulating differentiation and morphogenesis of endodermal tissues [211]. The Hh cellular machinery is enriched in primary cilia, which suggests that they are an element of mechanotransduction in endodermal development [54-56]. This has significant implications, because it supports the notion that embryonic development is a mechanism that involves mechanical forces from fluid flow, cellular deformation and ionic exchange.

Some of the most important genetic targets of Hh signaling are signals from the TGF-β family, which regulate responses to mechanical stimuli in liver development. It has been reported that primary cilia in postnatal liver tissues are exclusive of intrahepatic biliary ducts – one per cholangiocyte – and primary cilia length correlates with the dimensions of the bile duct [244]. These reports disagree with Hh expression in hepatic progenitors (hHpSCs and hHBs) around the periportal area [8, 12, 21, 133, 245]. In either case, distribution of primary cilia in hepatic tissues unveils a feedback mechanism that operates by monitoring bile tonicity, flow or viscosity with primary cilia to regulate biliary function [45]. This would define bile as both a carrier of homeostatic signals and a mechanical probe for liver function within the hepatic maturational gradient.

8.5. MATHEMATICAL DESCRIPTIONS OF DEVELOPING TISSUE MECHANICS

Tissue mechanics modeling requires understanding the mechanical properties of tissues. We can start by assuming that tissues are made of at least two fundamental phases: cells (with or without ECM) and interstitial fluids. Also, to understand the mechanics of tissues, we must consider how tissues respond to stress. Viscoelasticity describes how a material

responds to forces in time and whether material deformation exhibits a delay with respect to applied stress. The scale of this delay is a measure of viscoelasticity. This information helps determine the constitutive law, which defines the mechanical behavior of materials mathematically.

During development, permanent tissue deformations define morphogenesis. With that respect, there are three time scales to consider when implementing mathematical models of developing tissues. We can account for viscoelastic responses of ECM and cellular materials in a rapid time scale. In a slower time scale, tissues can be modeled as elastic since they return to a rest state after forces are removed, which defines a poroelastic model characteristic of mature tissues that store residual stresses. On an even longer time scale accounting for cell rearrangements, motility, mitosis and ECM remodeling, the poroelastic description can be substituted for a poroviscous one to express the mechanobiological active remodeling at the scale of tissue growth. This last time scale is especially suited for stem cell niches and embryoid bodies that do not store residual stresses comparable to those in mature tissues. In fact, early embryonic tissues exhibit behavior that parallels liquid mixtures (as discussed in Section 7.3.6). By using a poroviscous description in mathematical models of early embryonic morphogenesis, we can track permanent tissue deformations at the scale of growth, which is multiple orders of magnitude larger than the characteristic relaxation time of cells under stress in developing tissues [196]. In other words, for parsimony we can implement mechanics of developing tissues using a poroviscous description, since deformation stresses in developing tissues are dissipated over time scales of tissue growth.

The length scale of tissue development is also important. If we decide to model cells in tissues as part of purely viscous fluid continuum, we must qualify the characteristics of flow

in the dimensional scale of tissues. Force balance equations for fluid flow, the Navier-Stokes equations, determine that the qualitative behavior of viscous flow can be evaluated in terms of a nondimensional ratio between inertial and viscous forces, the Reynolds number $\mathrm{Re} = \rho VL/\eta$. This ratio is defined in terms of the density ρ, flow velocity V, length scale L and dynamic viscosity η of the flowing fluid. We can estimate $\mathrm{Re} < 1\times10^{-3}$ in the physiological context of tissue development with the density and viscosity of water (ρ=1000 kg/m3; η=0.001 Pa-s) in conjunction with length scales (~100 μm) and velocities for cell rearrangements and growth during embryonic development, which are slower than developmental fluid flow – e.g. 10 to 20 μm/s for embryonic nodal flow [240]. Deformations in embryonic tissues, when described in terms of viscous flow, also have higher viscosities than fluid flow in embryonic development, giving even lower Re.

Fluids with constant viscosity and flowing with $\mathrm{Re} << 1$ are known as Stokes fluids, in which flow is laminar, does not exhibit vorticity and primarily depends on viscous forces. These features simplify equations of motion. The Navier-Stokes equations dictate that this type of flow is time-invariant, which means that fluids with rate-dependent viscosities do not qualify under Stokes flow. In fluid mechanics terms, Stokes flow applies exclusively to Newtonian (rate-independent) fluids and, only under specific conditions, can approximate the behavior of non-Newtonian (rate-dependent) fluids.

When modeled as viscous fluids, the small length scales and flow velocities associated with developmental tissues are representative of Stokes flow. For example, the fluid properties of nodal flow suggest that fluids interacting with the embryo can be modeled as Stokes fluids. The same has been proposed for bile, since luminal flow is also low Reynolds

flow in secretory organs like liver [62]. We can use this information to define parsimonious descriptions of force balance equations for developing tissues in biomathematical models.

8.6. KM-HA HYDROGELS AS MODELS FOR TISSUE MECHANICS RESEARCH

One of the main characteristics of KM-HA hydrogels is that they exhibit no viscoelastic damping. Chemical modifications performed in HA for these hydrogels yield a high density of cross-linking sites. These modifications result in constant shear modulus G across a wide range of frequencies (0.05 – 5 Hz) that differs from the behavior of native hyaluronans [246]. High water content of KM-HA hydrogels (over 98%) results in mechanical incompressibility and effective diffusion that matches culture media. In addition, it is apparent that KM-HA hydrogels exhibit creeping response under fixed loads at time scales of hours, although we are not certain whether there is recovery after load removal or whether this response is exclusively due to water expulsion under compression (Appendix C.2, Figure 29). All this mechanical characterization advances our understanding of the behavior of KM-HAs, but is yet insufficient in formalizing a constitutive law description of their mechanical behavior. Hence, future experiments in KM-HA mechanics should be aimed towards establishing a constitutive law description for KM-HA hydrogels for their implementation in biomathematical models.

One advantage of using KM-HA hydrogels with determined stem cell populations, such as hHpSCs, is that KM-HA hydrogels provide a mechanical environment with predictable properties. In the specific case of our experimental research, our approach provides a successful model to quantify differentiation directed by mechanical stimuli in determined stem cell populations. However, this experimental *in vitro* model has a broader impact: by using a cell source from fetal origin and surveying lineage specification between a stem cell

stage (hHpSCs) and a transit amplifying cell stage with high proliferation capabilities (hHBs), our experimental approach studies cell types from developmental tissues within a predictable mechanical environment that could be implemented in biomathematical models. Currently, we can only hypothesize that this mechanical environment behaves as a polymeric solution at the time scale of differentiation *as a first-order approximation*, while we continue to model stem cell populations as developing tissues with purely viscous behavior.

In order to bridge between the experimental and computational models presented in this thesis in the future, it is fundamental that we understand the constitutive mechanical behavior of KM-HA hydrogels from experimental evidence. These efforts would not only describe how hHpSCs behave in established 3D environments, but also which types of forces can be applied onto these hydrogels sustainably for tissue engineering purposes. Furthermore, bridging between both models provides two exciting opportunities: first, it could be possible to investigate novel modes of mechanotransduction at the cellular level and expand them to broader tissue assembly mathematical schemes with our experimental approach; and second, we can either test experimental hypotheses computationally or design experiments, optimized using mathematical criteria expressed in terms of cellular function, that control variables at the tissue level.

8.7. CONCLUSION

The work presented in this thesis is relevant because it demonstrates two distinct approaches for surveying how mechanics affects developing tissues and the cells that assemble them. In one approach, by using a computational approach that models biological systems in developing tissues, we not only acquire understanding of the biology of growth regulation, but also provide a generic tool that describes quantitative requirements to expand

stem cell populations. Following a different approach, our experimental model explores how a mechanical variable, the stiffness of the microenvironment, can influence phenotypic properties of hepatic stem cells, which are isolated from liver tissue that does not have obvious mechanical roles. In that regard, the knowledge acquired from our experimental model does not improve our current biomathematical models of tissue growth, but does represent a step in that direction. In the end, by evaluating stem cell biology from two distinct perspectives – with justifiable individual merits – the work presented here explores both empirical and predictive aspects of tissue engineering, brings these aspects closer to each other and, in doing so, creates two useful models – one *in vivo* and one *in silico* – to close the gap.

APPENDIX A. COMSOL SOFTWARE NOTATION

Implementation of models in COMSOL is achieved by means of two fundamental equation forms: PDE general form and PDE coefficient form. All application modes in the COMSOL Multiphysics environment are properly arranged to follow either one of these two input forms because the numerical solver is designed to operate using equation structures of either one of these modes. Additionally, COMSOL translates PDE input into a variational calculus (or weak form) expression that can be analyzed and enriched by the user to add customized numerical solver features. These numerical features can help enhance stabilization and convergence, include mixed or higher order derivative terms than those allowed by the PDE general or coefficient forms, and other customized improvements to the numerical solver.

When an equation-based model that is not covered by available pre-defined modes needs to be analyzed (e.g. pre-determined PDE modes for conduction, convection, diffusion, heat and mass transport, etc.), both the PDE General Form and PDE Coefficient Form can be used. The PDE General Form is defined by the following description for a scalar variable u, flux vector Γ and coefficients R, G and F:

$$\begin{cases} e_a \dfrac{\partial^2 u}{\partial t^2} + d_a \dfrac{\partial u}{\partial t} + \nabla \cdot \Gamma = F & in\ \Omega \\ -\mathbf{n} \cdot \Gamma = G + \left(\dfrac{\partial R}{\partial u} \right)^T \mu & on\ \partial\Omega \\ 0 = R & on\ \partial_2\Omega \end{cases}$$

On the other hand, the PDE Coefficient Form, which represents a mathematical expansion of the PDE General Form, is defined as follows:

$$\begin{cases} e_a \dfrac{\partial^2 u}{\partial t^2} + d_a \dfrac{\partial u}{\partial t} + \nabla \cdot \left(-c\nabla u - \alpha u + \gamma\right) + \beta \cdot \nabla u + au = f & in\ \Omega \\ \mathbf{n} \cdot \left(c\nabla u + \alpha u - \gamma\right) + qu = g - h^T \mu & on\ \partial\Omega \\ hu = r & on\ \partial_2\Omega \end{cases}$$

In both cases, the first equation is the PDE, while the Neumann and Dirichlet boundary conditions are represented by the second and third equations, respectively. In all cases, the parameter μ represents a Lagrange multiplier. All coefficients in both forms can be functions of the solution u, space and time derivatives of u, or any of the spatial coordinates.

Choosing a PDE form for the equation-based model in COMSOL is rarely sufficient in accurately representing a desired system. In addition to knowing how to properly use the COMSOL Multiphysics software, it is necessary to understand an important principle of model implementation in COMSOL Multiphysics regarding mathematical orthodoxy: notation of fundamental vector and tensor operations in the COMSOL Multiphysics software environment exclusively obeys a fundamental Cartesian geometry. Due to this feature, vector and tensor operations in different coordinate systems requiring geometric transformations are not implicitly defined by COMSOL and need to be explicitly defined in the model by the user following a fixed orthonormal coordinate system scheme – unless a pre-defined application mode is used.

In COMSOL, performing a divergence operation on a vector $\overline{\mathbf{A}}$ in a Cartesian (fixed orthonormal) coordinate system recapitulates the mathematical meaning of this operation, since

$$\nabla \cdot \overline{\mathbf{A}} = \frac{\partial}{\partial x_1} A_1 + \frac{\partial}{\partial x_2} A_2 + \frac{\partial}{\partial x_3} A_3$$

where the coordinate system basis and the vector are defined as follows:

$$\langle x_1, x_2, x_3 \rangle \Leftrightarrow \langle x, y, z \rangle$$

$$\overline{\mathbf{A}} = A_1\mathbf{e}_1 + A_2\mathbf{e}_2 + A_3\mathbf{e}_3 = A_x\mathbf{e}_x + A_y\mathbf{e}_y + A_z\mathbf{e}_z$$

As it is evident from this example, COMSOL performs vector and tensor operations following differentiation rules of Cartesian coordinate systems. The same Cartesian rules apply to other tensor operations, such as gradients, covariant derivatives and tensor divergence for a scalar function F, a vector $\overline{\mathbf{A}}$ and a second-degree tensor $\tilde{\mathbf{T}}$:

$$\nabla F = \frac{\partial F}{\partial x_1}\mathbf{e}_1 + \frac{\partial F}{\partial x_2}\mathbf{e}_2 + \frac{\partial F}{\partial x_3}\mathbf{e}_3 = \frac{\partial F}{\partial x}\mathbf{e}_x + \frac{\partial F}{\partial y}\mathbf{e}_y + \frac{\partial F}{\partial z}\mathbf{e}_z$$

$$\nabla^2 F = \frac{\partial^2 F}{\partial x_1^2} + \frac{\partial^2 F}{\partial x_2^2} + \frac{\partial^2 F}{\partial x_3^2} = \frac{\partial^2 F}{\partial x^2} + \frac{\partial^2 F}{\partial y^2} + \frac{\partial^2 F}{\partial z^2}$$

$$\nabla\overline{\mathbf{A}} = \begin{bmatrix} \frac{\partial}{\partial x_1}A_1 & \frac{\partial}{\partial x_2}A_1 & \frac{\partial}{\partial x_3}A_1 \\ \frac{\partial}{\partial x_1}A_2 & \frac{\partial}{\partial x_2}A_2 & \frac{\partial}{\partial x_3}A_2 \\ \frac{\partial}{\partial x_1}A_3 & \frac{\partial}{\partial x_2}A_3 & \frac{\partial}{\partial x_3}A_3 \end{bmatrix} = \begin{bmatrix} \frac{\partial}{\partial x}A_x & \frac{\partial}{\partial y}A_x & \frac{\partial}{\partial z}A_x \\ \frac{\partial}{\partial x}A_y & \frac{\partial}{\partial y}A_y & \frac{\partial}{\partial z}A_y \\ \frac{\partial}{\partial x}A_z & \frac{\partial}{\partial y}A_z & \frac{\partial}{\partial z}A_z \end{bmatrix}$$

$$\nabla \cdot \tilde{\mathbf{T}} = \begin{matrix} \left[\frac{\partial}{\partial x_1}T_{11} + \frac{\partial}{\partial x_2}T_{12} + \frac{\partial}{\partial x_3}T_{13}\right]\mathbf{e}_1 + \\ \left[\frac{\partial}{\partial x_1}T_{21} + \frac{\partial}{\partial x_2}T_{22} + \frac{\partial}{\partial x_3}T_{23}\right]\mathbf{e}_2 + \\ \left[\frac{\partial}{\partial x_1}T_{31} + \frac{\partial}{\partial x_2}T_{32} + \frac{\partial}{\partial x_3}T_{33}\right]\mathbf{e}_3 \end{matrix} = \begin{matrix} \left[\frac{\partial}{\partial x}T_{xx} + \frac{\partial}{\partial y}T_{xy} + \frac{\partial}{\partial z}T_{xz}\right]\mathbf{e}_x + \\ \left[\frac{\partial}{\partial x}T_{yx} + \frac{\partial}{\partial y}T_{yy} + \frac{\partial}{\partial z}T_{yz}\right]\mathbf{e}_y + \\ \left[\frac{\partial}{\partial x}T_{zx} + \frac{\partial}{\partial y}T_{zy} + \frac{\partial}{\partial z}T_{zz}\right]\mathbf{e}_z \end{matrix}$$

Other coordinate systems such as cylindrical and spherical coordinate systems are better suited for certain geometries. In such cases, however, COMSOL allows users to redefine the nomenclature of the independent variables in accordance with the coordinate system in use,

but only goes as far as renaming the independent variables and does not impose any required geometric transformations of its vector and tensor operations. In order to distinguish between them, let ${}^{M}_{r,\vartheta,z}\nabla$ and ${}^{M}_{r,\vartheta,\psi}\nabla$ represent the vector differential *del* operator with orthodox mathematical interpretations in cylindrical and spherical coordinate systems, respectively, while ${}^{S}_{r,\vartheta,z}\nabla$ and ${}^{S}_{r,\vartheta,\psi}\nabla$ represent their counterparts as interpreted by the software architecture (i.e. COMSOL). In such cases, the following vector and (symmetric) tensor operations are mathematically true in a cylindrical coordinate system for a scalar function F, a vector $\overline{\mathbf{A}}$ and a second-degree tensor $\tilde{\mathbf{T}}$:

$$ {}^{M}_{r,\vartheta,z}\nabla F = \frac{\partial F}{\partial r}\mathbf{e}_r + \frac{1}{r}\frac{\partial F}{\partial \vartheta}\mathbf{e}_\vartheta + \frac{\partial F}{\partial z}\mathbf{e}_z $$

$$ {}^{M}_{r,\vartheta,z}\nabla \cdot \overline{\mathbf{A}} = \left(\frac{\partial}{\partial r} + \frac{1}{r}\right)A_r + \frac{1}{r}\frac{\partial}{\partial \vartheta}A_\vartheta + \frac{\partial}{\partial z}A_z $$

$$ {}^{M}_{r,\vartheta,z}\nabla^2 F = \frac{\partial^2 F}{\partial r^2} + \frac{1}{r}\frac{\partial F}{\partial r} + \frac{1}{r^2}\frac{\partial^2 F}{\partial \vartheta^2} + \frac{\partial^2 F}{\partial z^2} $$

$$ {}^{M}_{r,\vartheta,z}\nabla\overline{\mathbf{A}} = \begin{bmatrix} \frac{\partial}{\partial r}A_r & \frac{1}{r}\left(\frac{\partial}{\partial \vartheta}A_r - A_\vartheta\right) & \frac{\partial}{\partial z}A_r \\ \frac{\partial}{\partial r}A_\vartheta & \frac{1}{r}\left(\frac{\partial}{\partial \vartheta}A_\vartheta + A_r\right) & \frac{\partial}{\partial z}A_\vartheta \\ \frac{\partial}{\partial r}A_z & \frac{1}{r}\frac{\partial}{\partial \vartheta}A_z & \frac{\partial}{\partial z}A_z \end{bmatrix} $$

$$ {}^{M}_{r,\vartheta,z}\nabla\cdot\tilde{\mathbf{T}} = \begin{aligned} &\left[\frac{\partial}{\partial r}T_{rr} + \frac{1}{r}\frac{\partial}{\partial \vartheta}T_{r\vartheta} + \frac{\partial}{\partial z}T_{rz} + \frac{1}{r}\left(T_{rr} - T_{\vartheta\vartheta}\right)\right]\mathbf{e}_r + \\ &\left[\frac{\partial}{\partial r}T_{r\vartheta} + \frac{1}{r}\frac{\partial}{\partial \vartheta}T_{\vartheta\vartheta} + \frac{\partial}{\partial z}T_{\vartheta z} + \frac{1}{r}\left(2T_{r\vartheta}\right)\right]\mathbf{e}_\vartheta + \\ &\left[\frac{\partial}{\partial r}T_{rz} + \frac{1}{r}\frac{\partial}{\partial \vartheta}T_{\vartheta z} + \frac{\partial}{\partial z}T_{zz} + \frac{1}{r}\left(T_{rz}\right)\right]\mathbf{e}_z \end{aligned} $$

In the case of a spherical coordinate system these vector and (symmetric) tensor operations are mathematically true as follows:

$$\overset{M}{}_{r,\vartheta,\psi}\nabla F = \frac{\partial F}{\partial r}\mathbf{e}_r + \frac{1}{r}\frac{\partial F}{\partial \vartheta}\mathbf{e}_\vartheta + \frac{1}{r\sin\vartheta}\frac{\partial F}{\partial \psi}\mathbf{e}_\psi$$

$$\overset{M}{}_{r,\vartheta,\psi}\nabla\cdot\overline{\mathbf{A}} = \left(\frac{\partial}{\partial r}+\frac{2}{r}\right)A_r + \left(\frac{1}{r}\frac{\partial}{\partial \vartheta}+\frac{\cot\vartheta}{r}\right)A_\vartheta + \frac{1}{r\sin\vartheta}\frac{\partial}{\partial\psi}A_\psi$$

$$\overset{M}{}_{r,\vartheta,\psi}\nabla^2 F = \frac{\partial^2 F}{\partial r^2}+\frac{2}{r}\frac{\partial F}{\partial r}+\frac{1}{r^2\sin^2\psi}\frac{\partial^2 F}{\partial\vartheta^2}+\frac{1}{r^2}\cot\psi\frac{\partial F}{\partial\psi}+\frac{1}{r^2}\frac{\partial^2 F}{\partial\psi^2}$$

$$\overset{M}{}_{r,\vartheta,\psi}\nabla\overline{\mathbf{A}} = \begin{bmatrix} \frac{\partial}{\partial r}A_r & \frac{1}{r}\left(\frac{\partial}{\partial\vartheta}A_r - A_\vartheta\right) & \frac{1}{r}\left(\frac{1}{\sin\vartheta}\frac{\partial}{\partial\psi}A_r - A_\psi\right) \\ \frac{\partial}{\partial r}A_\vartheta & \frac{1}{r}\left(\frac{\partial}{\partial\vartheta}A_\vartheta + A_r\right) & \frac{1}{r}\left(\frac{1}{\sin\vartheta}\frac{\partial}{\partial\psi}A_\vartheta - A_\psi\cot\vartheta\right) \\ \frac{\partial}{\partial r}A_\psi & \frac{1}{r}\frac{\partial}{\partial\vartheta}A_\psi & \frac{1}{r}\left(\frac{\partial}{\partial\psi}A_\psi + A_\vartheta\cot\vartheta + A_r\right) \end{bmatrix}$$

$$\overset{M}{}_{r,\vartheta,\psi}\nabla\cdot\tilde{\mathbf{T}} = \begin{aligned} &\left[\frac{\partial}{\partial r}T_{rr}+\frac{1}{r}\frac{\partial}{\partial\vartheta}T_{r\vartheta}+\frac{1}{r\sin\vartheta}\frac{\partial}{\partial\psi}T_{r\psi}+\frac{1}{r}\left\{2T_{rr}+T_{r\vartheta}\cot\vartheta-\left(T_{\vartheta\vartheta}+T_{\psi\psi}\right)\right\}\right]\mathbf{e}_r + \\ &\left[\frac{\partial}{\partial r}T_{r\vartheta}+\frac{1}{r}\frac{\partial}{\partial\vartheta}T_{\vartheta\vartheta}+\frac{1}{r\sin\vartheta}\frac{\partial}{\partial\psi}T_{\vartheta\psi}+\frac{1}{r}\left\{3T_{r\vartheta}+\left(T_{\vartheta\vartheta}-T_{\psi\psi}\right)\cot\vartheta\right\}\right]\mathbf{e}_\vartheta + \\ &\left[\frac{\partial}{\partial r}T_{r\psi}+\frac{1}{r}\frac{\partial}{\partial\vartheta}T_{\vartheta\psi}+\frac{1}{r\sin\vartheta}\frac{\partial}{\partial\psi}T_{\psi\psi}+\frac{1}{r}\left\{3T_{r\psi}+2T_{\vartheta\psi}\cot\vartheta\right\}\right]\mathbf{e}_\psi \end{aligned}$$

Nonetheless, interpretation of these operations in COMSOL is limited to independent variable name substitution. This particular feature ensures that, at all times, in a Cartesian coordinate system,

$$\overset{S}{}_{x,y,z}\nabla \equiv \overset{M}{}_{x,y,z}\nabla$$

as we have shown before. However, this same property introduces significant issues when a model in a different coordinate system is preferred; i.e. vectorial rules are mathematically unorthodox in COMSOL because the software is not suited to perform geometric

transformations when coordinate systems are changed. For example, the gradient operation for a scalar function F, once the independent variables have been changed to a basis relevant to cylindrical coordinate systems,

$$\langle x_1, x_2, x_3 \rangle \Leftrightarrow \langle r, \vartheta, z \rangle$$

is interpreted by COMSOL as

$$\overset{S}{\nabla}_{r,\vartheta,z} F = \frac{\partial F}{\partial x_1}\mathbf{e_1} + \frac{\partial F}{\partial x_2}\mathbf{e}_2 + \frac{\partial F}{\partial x_3}\mathbf{e}_3 = \frac{\partial F}{\partial r}\mathbf{e}_r + \frac{\partial F}{\partial \vartheta}\mathbf{e}_\vartheta + \frac{\partial F}{\partial z}\mathbf{e}_z$$

or in the case of spherical coordinate systems, with a coordinate system basis such that

$$\langle x_1, x_2, x_3 \rangle \Leftrightarrow \langle r, \vartheta, \psi \rangle$$

the gradient operation for a scalar function F is interpreted by COMSOL as

$$\overset{S}{\nabla}_{r,\vartheta,\psi} F = \frac{\partial F}{\partial x_1}\mathbf{e_1} + \frac{\partial F}{\partial x_2}\mathbf{e}_2 + \frac{\partial F}{\partial x_3}\mathbf{e}_3 = \frac{\partial F}{\partial r}\mathbf{e}_r + \frac{\partial F}{\partial \vartheta}\mathbf{e}_\vartheta + \frac{\partial F}{\partial \psi}\mathbf{e}_\psi$$

These interpretations are mathematically incorrect, but as long as we can recognize the software-specific interpretation of these vector and tensor operations it is possible to translate cylindrical and spherical models to a suitable interpretation through COMSOL.

The same rules apply to boundary conditions. Any vectorial operations that define boundary conditions (e.g. Cauchy, Neumann, Dirichlet, Robin) must be explicitly expanded into each of their (orthodox) vectorial components. Once the components are fully expressed, they can be reassembled following the Cartesian-exclusive COMSOL vectorial rules.

APPENDIX B. COMSOL IMPLEMENTATION OF SPHERICAL SYMMETRY EQUATIONS

B.1. FORCE BALANCE EQUATION

The simplified force balance expression for spherically symmetric geometry

$$\frac{\partial}{\partial r}\left[(\lambda+2\mu)r^2\theta\frac{\partial}{\partial r}v_r\right]+\left[2\lambda r\frac{\partial\theta}{\partial r}-2(\lambda+2\mu)\theta\right]v_r=r^2\frac{\partial}{\partial r}(P+\mathrm{Y})$$

can be implemented in COMSOL using its fixed orthonormal basis by means of the PDE coefficient form where

$$\frac{\partial v_r}{\partial\vartheta}=\frac{\partial v_r}{\partial\psi}=\frac{\partial^2 v_r}{\partial\vartheta^2}=\frac{\partial^2 v_r}{\partial\psi^2}=0$$

$$\overset{C}{\nabla}_{r,\vartheta,\psi}=\underset{C}{\nabla}=\frac{\partial}{\partial r}\mathbf{e}_r+\frac{\partial}{\partial\vartheta}\mathbf{e}_\vartheta+\frac{\partial}{\partial\psi}\mathbf{e}_\psi=\frac{\partial}{\partial r}\mathbf{e}_r$$

$$e_a\frac{\partial^2 u}{\partial t^2}+d_a\frac{\partial u}{\partial t}+\underset{C}{\nabla}\cdot\left(-c\underset{C}{\nabla}u-\alpha u+\gamma\right)+\beta\cdot\underset{C}{\nabla}u+au=f$$

by defining the following coefficients with respect to the radial velocity v_r:

$$e_a=d_a=\alpha=\gamma=\beta=0$$

$$c=-(\lambda+2\mu)r^2\theta$$

$$a=2\lambda r\frac{\partial\theta}{\partial r}-2(\lambda+2\mu)\theta$$

$$f=r^2\frac{\partial}{\partial r}(P+\mathrm{Y})$$

for the implementation in COMSOL of the force balance equation

$$\underset{C}{\nabla}\cdot\left[(\lambda+2\mu)r^2\theta\underset{C}{\nabla}v_r\right]+\left[2\lambda r\frac{\partial\theta}{\partial r}-2(\lambda+2\mu)\theta\right]v_r=r^2\underset{C}{\nabla}(P+\mathrm{Y})$$

B.2. GROUP INCOMPRESSIBILITY CONDITION EQUATION

The group incompressibility condition equation

$$\frac{\partial}{\partial r}\left[r^2\left(\frac{1-\theta}{\varphi\theta}\right)(1-\theta)^2\frac{\partial}{\partial r}P\right]+\frac{\partial}{\partial r}\left\langle r^2\left\{\left(\frac{1-\theta}{\varphi\theta}\right)(1-\theta)\frac{\partial}{\partial r}\left[(1-\theta)\mathrm{Y}\right]-v_r\right\}\right\rangle=0$$

can be implemented in COMSOL using its fixed orthonormal basis by means of the PDE coefficient form where

$$\frac{\partial P}{\partial\vartheta}=\frac{\partial P}{\partial\psi}=\frac{\partial^2 P}{\partial\vartheta^2}=\frac{\partial^2 P}{\partial\psi^2}=0$$

$$\underset{r,\vartheta,\psi}{\overset{C}{\nabla}}=\underset{C}{\nabla}=\frac{\partial}{\partial r}\mathbf{e}_r+\frac{\partial}{\partial\vartheta}\mathbf{e}_\vartheta+\frac{\partial}{\partial\psi}\mathbf{e}_\psi=\frac{\partial}{\partial r}\mathbf{e}_r$$

$$e_a\frac{\partial^2 u}{\partial t^2}+d_a\frac{\partial u}{\partial t}+\underset{C}{\nabla}\cdot\left(-c\underset{C}{\nabla}u-\alpha u+\gamma\right)+\beta\cdot\underset{C}{\nabla}u+au=f$$

by defining the following coefficients with respect to the interstitial pressure P:

$$e_a=d_a=\alpha=\beta=a=f=0$$

$$c=-r^2\left(\frac{1-\theta}{\varphi\theta}\right)(1-\theta)^2$$

$$\gamma=r^2\left\{\left(\frac{1-\theta}{\varphi\theta}\right)(1-\theta)\frac{\partial}{\partial r}\left[(1-\theta)\mathrm{Y}\right]-v_r\right\}$$

for the group incompressibility condition implemented in COMSOL as follows:

$$\underset{C}{\nabla}\cdot\left\langle r^2\left(\frac{1-\theta}{\varphi\theta}\right)(1-\theta)^2\underset{C}{\nabla}P+r^2\left\{\left(\frac{1-\theta}{\varphi\theta}\right)(1-\theta)\frac{\partial}{\partial r}\left[(1-\theta)\mathrm{Y}\right]-v_r\right\}\right\rangle=0$$

B.3. GENERAL CONSERVATION EQUATIONS

In order to implement general conservation equations into COMSOL for spherically symmetric geometries:

$$r^2\frac{\partial u}{\partial t}+\frac{\partial}{\partial r}\left(r^2uv_r^u\right)=D_u\frac{\partial}{\partial r}\left(r^2\frac{\partial u}{\partial r}\right)+r^2R_u$$

we must recall that the interpretation of the vector differential *del* operator in COMSOL for a scalar gradient and Laplacian in the spherical coordinate system still follows a fixed orthonormal basis:

$$\underset{r,\vartheta,\psi}{\overset{C}{\nabla}}=\underset{C}{\nabla}=\frac{\partial}{\partial r}\mathbf{e}_r+\frac{\partial}{\partial\vartheta}\mathbf{e}_\vartheta+\frac{\partial}{\partial\psi}\mathbf{e}_\psi$$

$$\underset{r,\vartheta,\psi}{\overset{C}{\nabla}}{}^2=\underset{C}{\nabla}=\frac{\partial^2}{\partial r^2}+\frac{\partial^2}{\partial\vartheta^2}+\frac{\partial^2}{\partial\psi^2}$$

Therefore, the relevant representation of the equation for u in COMSOL using a fixed orthonormal description is as shown below:

$$r^2\frac{\partial u}{\partial t}+\underset{C}{\nabla}\cdot\left(r^2u\mathbf{v}^u\right)=\underset{C}{\nabla}\cdot\left(r^2D_u\underset{C}{\nabla}u\right)+r^2R_u$$

which corresponds to the mathematically orthodox equation

$$\frac{\partial u}{\partial t}+\underset{M}{\nabla}\cdot\left(u\mathbf{v}^u\right)=D_u\underset{M}{\nabla}^2u+R_u$$

where $\underset{r,\vartheta,\psi}{\overset{M}{\nabla}}\equiv\underset{M}{\nabla}$ is the vector differential *del* operator subject to geometric transformations into a spherical coordinate system.

It is possible to implement this equation through the Convection and Diffusion Application Mode in COMSOL such that

$$\delta_{ts}\frac{\partial u}{\partial t}+\nabla\cdot\left(-D\nabla u+u\mathbf{v}\right)=R$$

with the corresponding coefficients in COMSOL

$$\delta_{ts}=r^2$$

$$D = r^2 D_u$$

$$\mathbf{v} = r^2 \mathbf{v}^u$$

$$R = r^2 R_u$$

by rewriting the fixed orthonormal model description as

$$r^2 \frac{\partial u}{\partial t} + \underset{C}{\nabla} \cdot \left[-\left(r^2 D_u \right) \underset{C}{\nabla} u + u\left(r^2 \mathbf{v}^u \right) \right] = r^2 R_u$$

On the other hand, by using the PDE coefficient form, we can define the PDE in COMSOL for implementation as follows:

$$e_a \frac{\partial^2 u}{\partial t^2} + d_a \frac{\partial u}{\partial t} + \nabla \cdot \left(-c \nabla u - \alpha u + \gamma \right) + \beta \cdot \nabla u + a u = f$$

where

$$e_a = \gamma = \beta = a = 0$$

$$d_a = r^2$$

$$c = r^2 D_u$$

$$\alpha = -r^2 \mathbf{v}^u$$

$$f = r^2 R_u$$

One advantage of using a pre-defined application mode such as the Convection and Diffusion application mode is that solver stabilization techniques are also included and available for user implementation. Therefore, using proper mathematical care with regards to vector differential rules, numerical stabilization is easily added to the model by defining a coefficient as opposed to implementing the stabilization technique in the context of the full PDE definition, especially for mathematically intricate stabilization techniques.

APPENDIX C. SUPPLEMENTARY EXPERIMENTAL DATA

C.1. ANALYSIS OF STATISTICAL SIGNIFICANCE OF GENE EXPRESSION DATA FOR HEPATIC STEM CELLS IN KM-HA HYDROGELS

Quantitative Real Time PCR assays for differentiation markers in KM-HA-grown hHpSCs was analyzed for significance, both for each individual marker and with respect to their multivariate PCA scores. We previously reported the statistical significance of mRNA expression levels of hHpSCs in KM-HA after 1 week of culture with respect to 2D-grown hHpSC colonies and freshly isolated hHBs (Figure 18). Analyses for statistical significance also included comparisons amongst conditions, not only for variation around the mean (two-tailed Student's t-test), but also for equality of variances (two-tailed F-test). In conjunction, these statistical routines measure two statistical properties of mRNA expression levels in each gene of interest: first, whether the levels measured in each hHpSC seeding condition – i.e. each KM-HA hydrogel formulation – differs from the levels measured in each of the remaining seeding conditions; and second, whether we can confirm that the data spread for mRNA expression level in each condition is different from the rest. Simply put, both tests in combination confirm whether the average mRNA expression levels of two conditions are statistically different (Student's t-test), and whether this significance arises from two distinct outcomes or a random bias between two separate measurements of a single outcome (F-test).

Full inspection of mRNA expression levels for all genes of interest confirms that all data from KM-HA-grown hHpSCs are statistically distinct from either hHpSCs or hHBs. In general, on an individual marker basis, there are no significant differences across formulations, and any resulting trends in mRNA expression levels across the experimental

range of KM-HA hydrogel with respect to KM-HA hydrogels stiffness are not statistically significant. The highest statistical significance levels acquired arise from CD44 expression (Table 10). These significance levels agree with evaluation of gene expression profile by PCA, where the main source of variation across formulations corresponds to PC2 (Table 11), which measures intra-phenotype variation and is mostly dictated by CD44 expression as well (Figure 19).

Table 10. Full statistical significance analysis (two-tailed Student's t-test and two-tailed F-test) of gene expression levels for differentiation markers in KM-HA-grown hHpSCs.

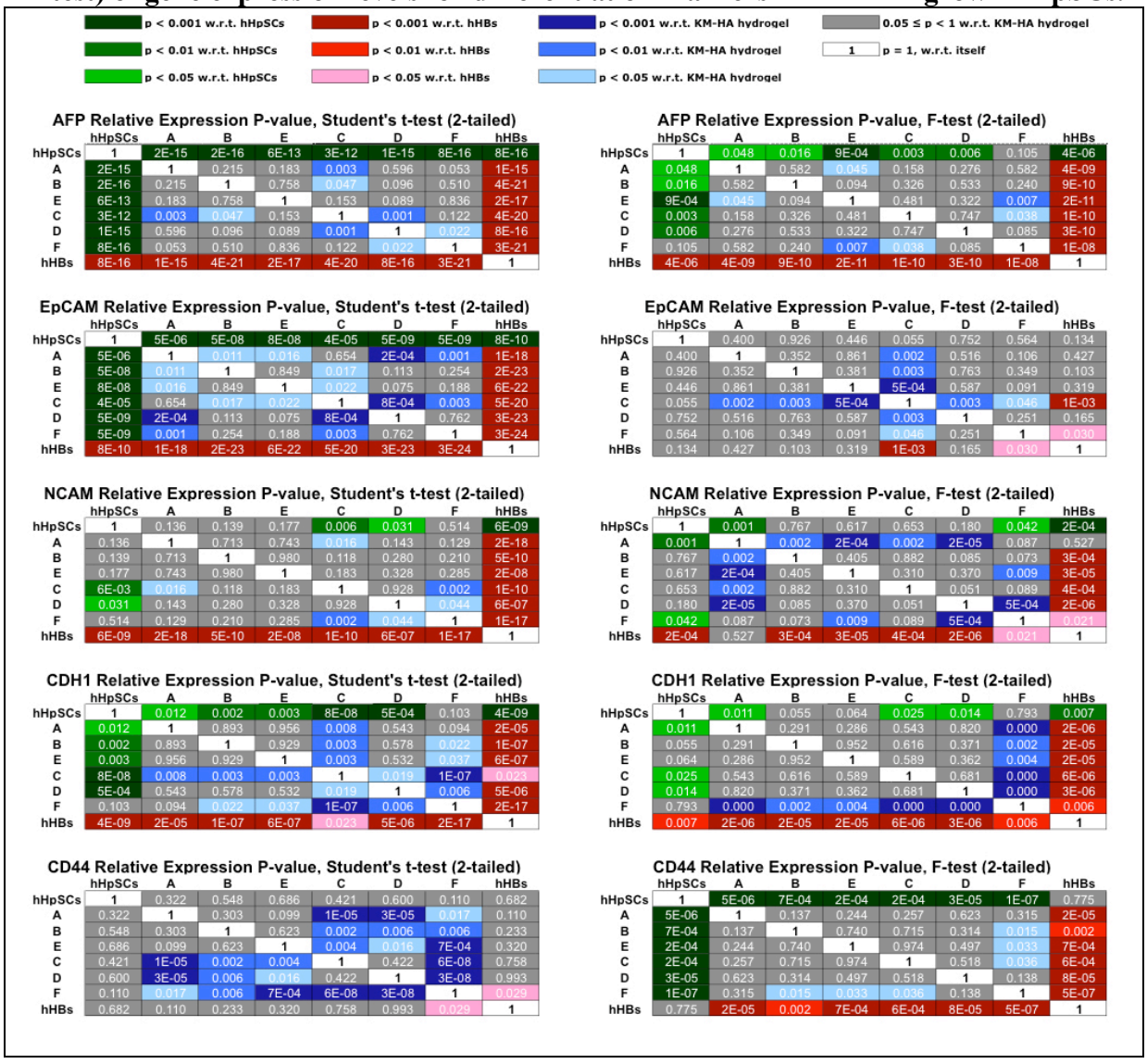

Table 11. Full statistical significance analysis (two-tailed Student's t-test and two-tailed F-test) of multivariate principal component (PC) scores of gene expression for differentiation markers in KM-HA-grown hHpSCs.

p < 0.001 w.r.t. hHpSCs | p < 0.001 w.r.t. hHBs | p < 0.001 w.r.t. KM-HA hydrogel | 0.05 ≤ p < 1 w.r.t. KM-HA hydrogel
p < 0.01 w.r.t. hHpSCs | p < 0.01 w.r.t. hHBs | p < 0.01 w.r.t. KM-HA hydrogel | 1 p = 1, w.r.t. itself
p < 0.05 w.r.t. hHpSCs | p < 0.05 w.r.t. hHBs | p < 0.05 w.r.t. KM-HA hydrogel

PC1 Score P-value, Student's t-test (2-tailed)

	hHpSCs	A	B	E	C	D	F	hHBs
hHpSCs	1	1E-07	0.007	2E-04	2E-09	3E-08	4E-05	4E-12
A	1E-07	1	0.091	0.376	0.007	0.030	2E-04	2E-11
B	0.007	0.091	1	0.428	0.003	0.006	0.940	2E-05
E	2E-04	0.376	0.428	1	0.010	0.023	0.239	4E-06
C	2E-09	0.007	0.003	0.010	1	0.824	9E-06	1E-04
D	3E-08	0.030	0.006	0.023	0.824	1	1E-04	3E-04
F	4E-05	2E-04	0.940	0.239	9E-06	1E-04	1	1E-15
hHBs	4E-12	2E-11	2E-05	4E-06	1E-04	3E-04	1E-15	1

PC1 Score P-value, F-test (2-tailed)

	hHpSCs	A	B	E	C	D	F	hHBs
hHpSCs	1	0.091	0.139	0.086	0.310	0.117	0.183	0.042
A	0.091	1	0.003	0.001	0.008	0.002	0.595	0.708
B	0.139	0.003	1	0.892	0.536	0.955	0.004	1E-03
E	0.086	0.001	0.892	1	0.401	0.827	0.001	4E-04
C	0.310	0.008	0.536	0.401	1	0.520	0.013	0.003
D	0.117	0.002	0.955	0.827	0.520	1	0.002	6E-04
F	0.183	0.595	0.004	0.001	0.013	0.002	1	0.356
hHBs	0.042	0.708	1E-03	4E-04	0.003	6E-04	0.356	1

PC2 Score P-value, Student's t-test (2-tailed)

	hHpSCs	A	B	E	C	D	F	hHBs
hHpSCs	1	0.011	0.109	0.401	0.035	0.142	0.006	0.321
A	0.011	1	0.188	0.010	2E-07	2E-06	0.697	0.088
B	0.109	0.188	1	0.262	5E-05	4E-04	0.091	0.550
E	0.401	0.010	0.262	1	3E-04	0.003	0.002	0.739
C	0.035	2E-07	5E-05	3E-04	1	0.325	3E-08	0.001
D	0.142	2E-06	4E-04	0.003	0.325	1	2E-07	0.008
F	0.006	0.697	0.091	0.002	3E-08	2E-07	1	0.046
hHBs	0.321	0.088	0.550	0.739	0.001	0.008	0.046	1

PC2 Score P-value, F-test (2-tailed)

	hHpSCs	A	B	E	C	D	F	hHBs
hHpSCs	1	0.053	0.167	0.125	0.329	0.238	0.023	0.702
A	0.053	1	0.649	0.596	0.253	0.342	0.893	0.116
B	0.167	0.649	1	0.976	0.546	0.675	0.536	0.298
E	0.125	0.596	0.976	1	0.517	0.661	0.471	0.254
C	0.329	0.253	0.546	0.517	1	0.825	0.158	0.577
D	0.238	0.342	0.675	0.661	0.825	1	0.232	0.445
F	0.023	0.893	0.536	0.471	0.158	0.232	1	0.061
hHBs	0.702	0.116	0.298	0.254	0.577	0.445	0.061	1

C.2. CREEP BEHAVIOR OF KM-HA HYDROGELS UNDER CONFINED COMPRESSION

One of our preliminary efforts to characterize the mechanical properties of KM-HA hydrogels was to use confined compression testing, which determines two mechanical properties of hydrated porous materials in a single test: the aggregate stiffness modulus H_A and the hydraulic permeability k [247]. The mechanical response of the hydrogels, which exhibited no equilibration under initial setup loading, influenced the decision to change our characterization method to a rheometrical approach (Figure 14). Raw data from confined compression tests showed that KM-HA hydrogels exhibit a creep response under fixed compression at time scales of hours (Figure 29). However, this experimental setup did not distinguish whether this creep response reflected expulsion of media under compression or true aggregate deformation, since we could not measure deformation recovery.

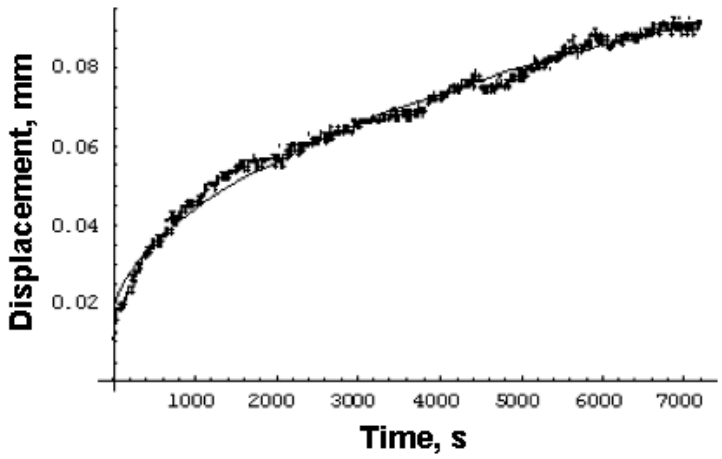

Figure 29. KM-HA hydrogels exhibit a creep response under fixed compressive load with a porous platen. Raw data from confined compression testing on a sample of KM-HA hydrogels (formulation C, Table 4) illustrates how these hydrogels do not to reach strain equilibrium under a fixed compressive load for hours and exhibit a creep response characteristic of fluid-like behavior. The confined compression uses a fixed setup load of 5 grams. Testing is performed with the experimental sample setup submerged in Kubota's medium (KM) throughout testing, which prevents loss of fluid from samples and ensures that samples maintain isotonic balance. The geometry of the sample, obtained with a circular biopsy punch from a KM-HA hydrogel cast in a 35-mm Petri culture plate, was a cylindrical plug approximately 6 mm in diameter and 2 mm thick. Points in plot correspond to data acquired from experimental setup at regular intervals; solid curve is the analytical solution to the confined compression problem, fitted by optimized least-squares regression to experimental data (R^2 = 0.989). Optimized regression for this sample determined aggregate modulus H_A = 3.22 kPa and hydraulic permeability $k = 5.84 \times 10^{-15}$ m^4/N-s.

REFERENCES

[1] Reid LM. Stem cell-fed maturational lineages and gradients in signals: relevance to differentiation of epithelia. Molecular biology reports. 1996;23:21-33.

[2] Reid LM, Fiorino AS, Sigal SH, Brill S, Holst PA. Extracellular matrix gradients in the space of Disse: relevance to liver biology. Hepatology. 1992;15:1198-203.

[3] Sigal SH, Brill S, Fiorino AS, Reid LM. The liver as a stem cell and lineage system. Am J Physiol. 1992;263:G139-48.

[4] Taipale J, Keski-Oja J. Growth factors in the extracellular matrix. FASEB J. 1997;11:51-9.

[5] Liu H, Di Cunto F, Imarisio S, Reid LM. Citron kinase is a cell cycle-dependent, nuclear protein required for G2/M transition of hepatocytes. J Biol Chem. 2003;278:2541-8.

[6] Okabe M, Tsukahara Y, Tanaka M, Suzuki K, Saito S, Kamiya Y, et al. Potential hepatic stem cells reside in EpCAM+ cells of normal and injured mouse liver. Development (Cambridge, England). 2009;136:1951-60.

[7] Tanaka M, Okabe M, Suzuki K, Kamiya Y, Tsukahara Y, Saito S, et al. Mouse hepatoblasts at distinct developmental stages are characterized by expression of EpCAM and DLK1: drastic change of EpCAM expression during liver development. Mech Dev. 2009;126:665-76.

[8] Schmelzer E, Wauthier E, Reid LM. The phenotypes of pluripotent human hepatic progenitors. Stem Cells. 2006;24:1852-8.

[9] Sicklick JK, Li YX, Melhem A, Schmelzer E, Zdanowicz M, Huang J, et al. Hedgehog signaling maintains resident hepatic progenitors throughout life. Am J Physiol Gastrointest Liver Physiol. 2005;290:G859-70. Epub Dec 1, 2005.

[10] Kuwahara R, Kofman AV, Landis CS, Swenson ES, Barendswaard E, Theise ND. The hepatic stem cell niche: identification by label-retaining cell assay. Hepatology. 2008;47:1994-2002.

[11] Saxena R, Theise N. Canals of Hering: recent insights and current knowledge. Seminars in Liver Disease. 2004;24:43-8.

[12] Schmelzer E, Zhang L, Bruce A, Wauthier E, Ludlow J, Yao HL, et al. Human hepatic stem cells from fetal and postnatal donors. J Exp Med. 2007;204:1973-87.

[13] Stachelscheid H, Urbaniak T, Ring A, Spengler B, Gerlach JC, Zeilinger K. Isolation and characterization of adult human liver progenitors from ischemic liver tissue derived from therapeutic hepatectomies. Tissue Engineering, Part A. 2009;15:1633-43.

[14] Zhang L, Theise N, Chua M, Reid LM. The stem cell niche of human livers: symmetry between development and regeneration. Hepatology. 2008;48:1598-607.

[15] Zhou H, Rogler LE, Teperman L, Morgan G, Rogler CE. Identification of hepatocytic and bile ductular cell lineages and candidate stem cells in bipolar ductular reactions in cirrhotic human liver. Hepatology. 2007;45:716-24.

[16] Wang Y, Yao H-L, Cui C-B, Wauthier E, Barbier C, Costello MJ, et al. Paracrine signals from mesenchymal cell populations govern the expansion and differentiation of human hepatic stem cells to adult liver fates. Hepatology. 2010;52:1443-54.

[17] Crosby HA, Kelly DA, Strain AJ. Human hepatic stem-like cells isolated using c-kit or CD34 can differentiate into biliary epithelium. Gastroenterology. 2001;120:534-44.

[18] Theise ND, Saxena R, Portmann BC, Thung SN, Yee H, Chiriboga L, et al. The canals of Hering and hepatic stem cells in humans. Hepatology. 1999;30:1425-33.

[19] McClelland R, Wauthier E, Uronis J, Reid L. Gradients in the liver's extracellular matrix chemistry from periportal to pericentral zones: influence on human hepatic progenitors. Tissue Eng Part A. 2008;14:59-70.

[20] Kubota H, Reid LM. Clonogenic hepatoblasts, common precursors for hepatocytic and biliary lineages, are lacking classical major histocompatibility complex class I antigen. PNAS. 2000;97:12132-7.

[21] Wauthier E, Schmelzer E, Turner W, Zhang L, Lecluyse E, Ruiz J, et al. Hepatic stem cells and hepatoblasts: identification, isolation, and ex vivo maintenance. Methods Cell Biol. 2008;86:137-225.

[22] Turner WS, Seagle C, Galanko JA, Favorov O, Prestwich GD, Macdonald JM, et al. Nuclear magnetic resonance metabolomic footprinting of human hepatic stem cells and hepatoblasts cultured in hyaluronan-matrix hydrogels. Stem Cells. 2008;26:1547-55.

[23] Wang Y, Cui C-B, Yamauchi M, Miguez P, Roach M, Malavarca R, et al. Lineage restriction of human hepatic stem cells to mature fates is made efficient by tissue-specific biomatrix scaffolds. Hepatology. 2011;53:293-305.

[24] Roskams TA, Theise ND, Balabaud C, Bhagat G, Bhathal PS, Bioulac-Sage P, et al. Nomenclature of the Finer Branches of the biliary Tree: Canals, Ductules, and Ductular Reactions in Human Livers. Hepatology. 2004;39:1739-45.

[25] Kubota H, Yao HL, Reid LM. Identification and characterization of vitamin A-storing cells in fetal liver: implications for functional importance of hepatic stellate cells in liver development and hematopoiesis. Stem Cells. 2007;25:2339-49.

[26] Turner WS, Schmelzer E, McClelland R, Wauthier E, Chen W, Reid LM. Human hepatoblast phenotype maintained by hyaluronan hydrogels. J Biomed Mater Res B Appl Biomater. 2007;82:156-68.

[27] Haruna Y, Saito K, Spaulding S, Nalesnik MA, Gerber MA. Identification of bipotential progenitor cells in human liver development. Hepatology. 1996;23:476-81.

[28] Kubota H, Storms RW, Reid LM. Variant forms of alpha-fetoprotein transcripts expressed in human hematopoietic progenitors. Implications for their developmental potential towards endoderm. Journal of Biological Chemistry. 2002;277:27629-35.

[29] Schmelzer E, Reid LM. Telomerase activity in human hepatic stem cells , hepatoblasts and hepatocytes from neonatal, pediatric, adult and geriatric donors. European Journal of Hepatology and Gastroenterology. 2009;21:1191-8.

[30] Tan J, Hytiroglou P, Wieczorek R, Park YN, Thung SN, Arias B, et al. Immunohistochemical evidence for hepatic progenitor cells in liver diseases. Liver. 2002;22:365-73.

[31] McClelland R, Wauthier E, Zhang L, Barbier C, Melhem A, Schmelzer E, et al. *Ex vivo* conditions for self-replication of human hepatic stem cells Tissue Eng. 2008;14:1-11.

[32] Alvaro D, Mancino MG, Glaser S, Gaudio E, Marzioni M, Francis H, et al. Proliferating cholangiocytes: a neuroendocrine compartment in the diseased liver. Gastroenterology. 2007;132:415-31.

[33] Glaser S, Francis H, DeMorrow S, LeSage G, Fava G, Marzioni M, et al. Heterogeneity of the intrahepatic biliary epithelium. World Journal of Gastroenterology. 2006;12:3523-36.

[34] Alpini G, Ulrich C, Roberts S, Phillips JO, Ueno Y, Podila PV, et al. Molecular and functional heterogeneity of cholangiocytes from rat liver after bile duct ligation. Am J Physiol. 1997;272:G289-97.

[35] Alpini G, Ueno Y, Glaser SS, Marzioni M, Phinizy JL, Francis H, et al. Bile acid feeding increased proliferative activity and apical bile acid transporter expression in both small and large rat cholangiocytes. Hepatology. 2001;34:868-76.

[36] Duncan A, Hickey RD, Paulk NK, Culberson AJ, Olson SB, Finegold MJ, et al. Ploidy Reductions in Murine Fusion-derived Hepatocytes. PLoS Genetics. 2009;5:e1000385.

[37] Rhim JA, Sandgren EP, Degen JL, Palmiter RD, Brinster RL. Replacement of diseased mouse liver by hepatic cell transplantation. Science. 1994;263:1149-52.

[38] Alvaro D, Alpini G, Jezequel AM, Bassotti C, Francia C, Fraioli F, et al. Role and mechanisms of action of acetylcholine in the regulation of rat cholangiocyte secretory functions. J Clin Invest. 1997;100:1349-62.

[39] Ueno Y, Alpini G, Yahagi K, Kanno N, Moritoki Y, Fukushima K, et al. Evaluation of differential gene expression by microarray analysis in small and large cholangiocytes isolated from normal mice. Liver International. 2003;23:449-59.

[40] Terada T, Kato M, Horie S, Endo K, Kitamura Y. Expression of pancreatic alpha-amylase protein and messenger RNA in hilar primitive bile ducts and hepatocytes during human fetal liver organogenesis: an immunohistochemical and in situ hybridization study. Liver. 1998;18:313-9.

[41] LeSage GD, Glaser SS, Marucci L, Benedetti A, Phinizy JL, Rodgers R, et al. Acute carbon tetrachloride feeding induces damage of large but not small cholangiocytes from BDL rat liver. Am J Physiol. 1999;276:G1289-G301.

[42] Mancinelli R, Franchitto A, Gaudio E, Onori P, Glaser S, Francis H, et al. After Damage of Large Bile Ducts by Gamma-Aminobutyric Acid, Small Ducts Replenish the Biliary Tree by Amplification of Calcium-Dependent Signaling and de Novo Acquisition of Large Cholangiocyte Phenotypes. The American Journal of Pathology. 2010;176:1790-800.

[43] Bishop JR, Schuksz M, Esko JD. Heparan sulphate proteoglycans fine-tune mammalian physiology. Nature. 2007;446:1030-7.

[44] Jhandier MN, Kruglov EA, Lavoie EG, Sevigny J, Dranoff JA. Portal fibroblasts regulate the proliferation of bile duct epithelia via expression of NTPDase2. J Biol Chem. 2005;280:22986-92.

[45] Woo K, Dutta AK, Patel V, Kresge C, Feranchak AP. Fluid flow induces mechanosensitive ATP release, calcium signalling and Cl- transport in biliary epithelial cells through a PKCzeta-dependent pathway. The Journal of physiology. 2008;586:2779-98.

[46] Cassiman D, Libbrecht L, Sinelli N, Desmet V, Denef C, Roskams T. The vagal nerve stimulates activation of the hepatic progenitor cell compartment via muscarinic acetylcholine receptor type 3. Am J Pathol. 2002;161:521-30.

[47] Engler AJ, Sen S, Sweeney HL, Discher DE. Matrix elasticity directs stem cell lineage specification. Cell. 2006;126:677-89.

[48] Krieg M, Arboleda-Estudillo Y, Puech PH, Kafer J, Graner F, Muller DJ, et al. Tensile forces govern germ-layer organization in zebrafish. Nat Cell Biol. 2008;10:429-36.

[49] Schwartz MA, DeSimone DW. Cell adhesion receptors in mechanotransduction. Curr Opin Cell Biol. 2008;20:551-6.

[50] Sakata R, Ueno T, Nakamura T, Ueno H, Sata M. Mechanical stretch induces TGF-beta synthesis in hepatic stellate cells. Eur J Clin Invest. 2004;34:129-36.

[51] Batut J, Howell M, Hill CS. Kinesin-mediated transport of Smad2 is required for signaling in response to TGF-beta ligands. Dev Cell. 2007;12:261-74.

[52] Massague J, Seoane J, Wotton D. Smad transcription factors. Genes & development. 2005;19:2783-810.

[53] Praetorius HA, Spring KR. A physiological view of the primary cilium. Annual review of physiology. 2005;67:515-29.

[54] Eggenschwiler JT, Anderson KV. Cilia and developmental signaling. Annual review of cell and developmental biology. 2007;23:345-73.

[55] King PJ, Guasti L, Laufer E. Hedgehog signalling in endocrine development and disease. The Journal of endocrinology. 2008;198:439-50.

[56] Kim J, Kato M, Beachy PA. Gli2 trafficking links Hedgehog-dependent activation of Smoothened in the primary cilium to transcriptional activation in the nucleus. PNAS. 2009;106:21666-71.

[57] Cohen MM, Jr. The hedgehog signaling network. American journal of medical genetics. 2003;123A:5-28.

[58] McLin VA, Rankin SA, Zorn AM. Repression of Wnt/beta-catenin signaling in the anterior endoderm is essential for liver and pancreas development. Development (Cambridge, England). 2007;134:2207-17.

[59] Ober EA, Field HA, Stainier DY. From endoderm formation to liver and pancreas development in zebrafish. Mech Dev. 2003;120:5-18.

[60] Rivas-Carrillo JD, Okitsu T, Tanaka N, Kobayashi N. Pancreas development and beta-cell differentiation of embryonic stem cells. Current medicinal chemistry. 2007;14:1573-8.

[61] Sangeetha NM, Bhat S, Choudhury AR, Maitra U, Terech P. Properties of Hydrogels Derived from Cationic Analogues of Bile Acid: Remarkably Distinct Flowing Characteristics. The Journal of Physical Chemistry B. 2004;108:16056-63.

[62] Luo X, Li W, Bird N, Chin SB, Hill NA, Johnson AG. On the mechanical behavior of the human biliary system. World J Gastroenterol. 2007;13:1384-92.

[63] Sigal SH, Rajvanshi P, Gorla GR, Sokhi RP, Saxena R, Gebhard DR, Jr., et al. Partial hepatectomy-induced polyploidy attenuates hepatocyte replication and activates cell aging events. American Journal of Physiology - Gastrointestinal and Liver Physiology. 1999;276:G1260-G72.

[64] Roskams T. Liver stem cells and their implication in hepatocellular and cholangiocarcinoma. Oncogene. 2006;25:3818-22.

[65] Turner R, Gerber D, Reid L. The future of cell transplant therapies: a need for tissue grafting. Transplantation. 2010;90:807-10.

[66] Potter VR. The present status of the blocked ontogeny hypothesis of neoplasia: the thalassemia connection. Oncodevelopmental Biology & Medicine. 1981;2:243-66.

[67] Sell S. On the stem cell origin of Cancer. American Journal of Pathology. 2010;176:1-11.

[68] Yamashita T, Ji J, Budhu A, Forgues M, Yang W, Wang HY, et al. EpCAM-positive hepatocellular carcinoma cells are tumor-initiating cells with stem/progenitor cell features. Gastroenterology. 2009;136:1012-24.

[69] Yamashita T, Forgues M, Wang W, Kim JW, Ye Q, Jia H, et al. EpCAM and alpha-fetoprotein expression defines novel prognostic subtypes of hepatocellular carcinoma. Cancer Res. 2008;68:1451-61.

[70] Fausto N, Campbell JS. The role of hepatocytes and oval cells in liver regeneration and repopulation. Mech Dev. 2003;120:117-30.

[71] Grisham JW, Thorgeirsson SS, Potten CS. Liver stem cells. Stem Cells. London: Academic Press; 1997. p. 233-82.

[72] Guest I, Ilic Z, Sell S. Age dependence of oval cell responses and bile duct carcinomas in male fischer 344 rats fed a cyclic choline-deficient, ethionine-supplemented diet. Hepatology. 2010;52:1750-7.

[73] Hixson DC, Allison JP. Monoclonal antibodies recognizing oval cells induced in the liver of rats by N-2-fluorenylacetamide or ethionine in a choline-deficient diet. Cancer Res. 1985;45:3750-60.

[74] Oh BK, Lee CH, Park C, Park YN. Telomerase regulation and progressive telomere shortening of rat hepatic stem-like epithelial cells during in vitro aging. Exp Cell Res. 2004;298:445-54.

[75] Roskams TA, Libbrecht L, Desmet VJ. Progenitor cells in diseased human liver. Semin Liver Dis. 2003;23:385-96.

[76] Sobaniec-Lotowska ME, Lotowska JM, Lebensztejn DM. Ultrastructure of oval cells in children with chronic hepatitis B, with special emphasis on the stage of liver fibrosis: The first pediatric study. World Journal of Gastroenterology. 2007;13:2918-22.

[77] Thorgeirsson SS, Factor, Valentina M., and Grisham, Joe W. . Stem Cells. 1 ed. London: Elsevier; 2004.

[78] Lanza R, Gearhart J, Hogan B, Melton D, Pedersen R, Thomson J, et al. Handbook of Stem Cells. New York City: Elsevier Academic Press; 2004.

[79] Feldmann G. Liver ploidy. J Hepatol. 1992;16:7-10.

[80] Gerlyng P, Abyholm A, Grotmol T, Erikstein B, Huitfeldt HS, Stokke T, et al. Binucleation and polyploidization patterns in developmental and regenerative rat liver growth. Cell Proliferation. 1993;26:557-65.

[81] Kudriavtsev BN, Kudriatseva MV, Sakuta GA, Shtein GI. [The kinetics of the cell population of human liver parenchyma at different periods of life]. Tsitologiia. 1991;33:96-109.

[82] Watanabe T, Tanaka Y. Age-related alterations in the size of human hepatocytes. A study of mononuclear and binucleate cells. Virchows Archiv B, Cell Pathology Including Molecular Pathology. 1982;39:9-20.

[83] Deschenes J, Valet JP, Marceau N. The relationship between cell volume, ploidy. and functional activity in differentiating hepatocytes. Cell Biophysics. 1981;3:321-34.

[84] Cardinale V, Wang Y, Carpino G, Alvaro D, Reid LM, Gaudio E. Multipotent stem cells in the biliary tree. Italian Journal of Anatomy and Embryology. 2010;115:85-90.

[85] Cardinale V, Wang Y, Mendel G, Gaudio E, Reid LM, Alvaro D. The Biliary Tree: a Reservoir of Multipotent Stem Cells. In press. 2011.

[86] Fujita M, Spray DC, Choi H, Saez JC, Watanabe T, Rosenberg LC, et al. Glycosaminoglycans and proteoglycans induce gap junction expression and restore transcription of tissue-specific mRNAs in primary liver cultures. Hepatology. 1987;7:1-9.

[87] Spray DC, Fujita M, Saez JC, Choi H, Watanabe T, Hertzberg E, et al. Proteoglycans and glycosaminoglycans induce gap junction synthesis and function in primary liver cultures. J Cell Biol. 1987;105:541-51.

[88] Zvibel I, Halay E, Reid LM. Heparin and hormonal regulation of mRNA synthesis and abundance of autocrine growth factors: relevance to clonal growth of tumors. Mol Cell Biol. 1991;11:108-16.

[89] Gebhardt R. Different proliferative activity in vitro of periportal and perivenous hepatocytes. Scandinavian Journal of Gastroenterology - Supplement. 1988;151:8-18.

[90] Gebhardt R, Ebert A, Bauer G. Heterogeneous expression of glutamine synthetase mRNA in rat liver parenchyma revealed by in situ hybridization and Northern blot analysis of RNA from periportal and perivenous hepatocytes. FEBS Lett. 1988;241:89-93.

[91] Gumucio JJ. Hepatocyte heterogeneity and liver function. Madrid: Springer International; 1989.

[92] Lindros KO. Zonation of cytochrome P450 expression, drug metabolism and toxicity in liver. General Pharmacology: The Vascular System. 1997;28:191-6.

[93] Lindros KO, Oinonen T, Issakainen J, Nagy P, Thorgeirsson SS. Zonal distribution of transcripts of four hepatic transcription factors in the mature rat liver. Cell Biol Toxicol. 1997;13:257-62.

[94] Traber PG, Chianale J, Gumucio JJ. Physiologic significance and regulation of hepatocellular heterogeneity [see comments]. Gastroenterology. 1988;95:1130-43.

[95] Jungermann K, Kietzmann T. Zonation of parenchymal and nonparenchymal metabolism in liver. [Review] [70 refs]. Annual Review of Nutrition. 1996;16:179-203.

[96] Jungermann K. Zonal liver cell heterogeneity. [Review] [6 refs]. Enzyme. 1992;46:5-7.

[97] Lyon M, Gallagher JT. Purification and partial characterization of the major cell-associated heparan sulphate proteoglycan of rat liver. Biochemical Journal. 1991;273:415-22.

[98] Gupta S. Hepatic polyploidy and liver growth control Seminars in Cancer Biology. 2000;10:161-71.

[99] Overturf K, al-Dhalimy M, Ou CN, Finegold M, Grompe M. Serial transplantation reveals the stem-cell-like regenerative potential of adult mouse hepatocytes. Am J Pathol. 1997;151:1273-80.

[100] Zaret KS, Grompe M. Generation and regeneration of cells of the liver and pancreas. Science. 2008;322:1490-4.

[101] Danial NN, Korsmeyer SJ. Cell death: critical control points. Cell. 2004;116:205-19.

[102] Fesik SW, Shi Y. Structural biology. Controlling the caspases. Science. 2001;294:1477-8.

[103] Mattson MP, Chan SL. Calcium orchestrates apoptosis. Nat Cell Biol. 2003;5:1041-3.

[104] Susin SA, Daugas E, Ravagnan L, Samejima K, Zamzami N, Loeffler M, et al. Two Distinct Pathways Leading to Nuclear Apoptosis. The Journal of Experimental Medicine. 2000;192:571-80.

[105] Wajant H. The Fas signaling pathway: more than a paradigm. Science. 2002;296:1635-6.

[106] Gebhardt R. Metabolic zonation of the liver: regulation and implications for liver function. Pharmacology and Therapeutics. 1992;53:275-354.

[107] Hayes AJ, Tudor D, Nowell MA, Caterson B, Hughes CE. Chondroitin sulfate sulfation motifs as putative biomarkers for isolation of articular cartilage progenitor cells. J Histochem Cytochem. 2008;56:125-38.

[108] Vongchan P, Warda M, Toyoda H, Toida T, Marks RM, Linhardt RJ. Structural characterization of human liver heparan sulfate. Biochimica et biophysica acta. 2005;1721:1-8.

[109] Lu P, Werb Z. Patterning mechanisms of branched organs. Science. 2008;322:1506-9.

[110] Montell DJ. Morphogenetic cell movements: diversity from modular mechanical properties. Science. 2008;322:1502-5.

[111] Ingber DE. Mechanobiology and diseases of mechanotransduction. Annals of medicine. 2003;35:564-77.

[112] Cohen DM, Chen CS. Mechanical control of stem cell differentiation. In: Bhatia SN, Polak J, editors. StemBook: The Stem Cell Research Community; 2008.

[113] Guilak F, Cohen DM, Estes BT, Gimble JM, Liedtke W, Chen CS. Control of stem cell fate by physical interactions with the extracellular matrix. Cell stem cell. 2009;5:17-26.

[114] Slack JM. Stem cells in epithelial tissues. Science. 2000;287:1431-3.

[115] Zertal-Zidani S, Bounacer A, Scharfmann R. Regulation of pancreatic endocrine cell differentiation by sulphated proteoglycans. Diabetologia. 2007;50:585-95.

[116] Gray H, Clemente CD. Anatomy of the human body. 30th American ed. Philadelphia: Lea & Febiger; 1985.

[117] Jungermann K, Katz N. Functional specialization of different hepatocyte populations. Physiol Rev. 1989;69:708-64.

[118] Martinez-Hernandez A, Amenta PS. The hepatic extracellular matrix. II. Ontogenesis, regeneration and cirrhosis. Virchows Arch A Pathol Anat Histopathol. 1993;423:77-84.

[119] Martinez-Hernandez A, Amenta PS. The hepatic extracellular matrix. I. Components and distribution in normal liver. Virchows Arch A Pathol Anat Histopathol. 1993;423:1-11.

[120] Martinez-Hernandez A, Amenta PS. The extracellular matrix in hepatic regeneration. FASEB J. 1995;9:1401-10.

[121] Martinez-Hernandez A, Delgado FM, Amenta PS. The extracellular matrix in hepatic regeneration. Localization of collagen types I, III, IV, laminin, and fibronectin. Lab Invest. 1991;64:157-66.

[122] Turner R, Lozoya O, Wang Y, Cardinale V, Gaudio E, Alpini G, et al. Human hepatic stem cell and maturational liver lineage biology. Hepatology. 2011;53:1035-45.

[123] Anatskaya OV, Vinogradov AE, Kudryavtsev BN. Hepatocyte polyploidy and metabolism/life-history traits: hypotheses testing. J Theor Biol. 1994;168:191-9.

[124] Duncan SA. Transcriptional regulation of liver development. Dev Dyn. 2000;219:131-42.

[125] Reid LM, Jefferson DM. Culturing hepatocytes and other differentiated cells. Hepatology. 1984;4:548-59.

[126] Shu XZ, Ahmad S, Liu Y, Prestwich GD. Synthesis and evaluation of injectable, in situ crosslinkable synthetic extracellular matrices for tissue engineering. J Biomed Mater Res A. 2006;79:902-12.

[127] Shu XZ, Liu Y, Luo Y, Roberts MC, Prestwich GD. Disulfide cross-linked hyaluronan hydrogels. Biomacromolecules. 2002;3:1304-11.

[128] Shu XZ, Liu Y, Palumbo F, Luo Y, Prestwich GD. In situ crosslinkable glycosaminoglycan hydrogels for tissue engineering. Biomaterials. 2004;25:1339-48.

[129] Shu XZ, Prestwich GD. Therapeutic biomaterials from chemically modified hyaluronan. In: Garg H, Hales C, editors. Chemistry and Biology of Hyaluronan. Amsterdam: Elsevier Press; 2004. p. 475-504.

[130] Vanderhooft JL, Alcoutlabi M, Magda JJ, Prestwich GD. Rheological properties of cross-linked hyaluronan-gelatin hydrogels for tissue engineering. Macromol Biosci. 2009;9:20-8.

[131] Menard KP. Dynamic mechanical analysis : a practical introduction. Boca Raton, FL: CRC Press; 2008.

[132] Leddy HA, Guilak F. Site-specific molecular diffusion in articular cartilage measured using fluorescence recovery after photobleaching. Ann Biomed Eng. 2003;31:753-60.

[133] Schmelzer E, McClelland R, Melhem A, Zhang L, Yao H, Wauthier E, et al. Hepatic Stem Cells and the Liver's Maturational Stages: Implications for Liver Biology, Gene Expression, and Cell Therapies. In: Potten C, Clarke R, Wilson J, Renehan A, editors. Tissue Stem Cells. New York: Taylor & Francis, Inc.; 2006. p. 161-214.

[134] Pfaffl MW. A new mathematical model for relative quantification in real-time RT-PCR. Nucleic acids research. 2001;29:e45.

[135] Schmittgen TD, Livak KJ. Analyzing real-time PCR data by the comparative C(T) method. Nature protocols. 2008;3:1101-8.

[136] Jefferson DM, Clayton DF, Darnell JE, Jr., Reid LM. Posttranscriptional modulation of gene expression in cultured rat hepatocytes. Mol Cell Biol. 1984;4:1929-34.

[137] Chen Y, Dong XJ, Zhang GR, Shao JZ, Xiang LX. In vitro differentiation of mouse bone marrow stromal stem cells into hepatocytes induced by conditioned culture medium of hepatocytes. J Cell Biochem. 2007;102:52-63.

[138] Purps O, Lahme B, Gressner AM, Meindl-Beinker NM, Dooley S. Loss of TGF-beta dependent growth control during HSC transdifferentiation. Biochem Biophys Res Commun. 2007;353:841-7.

[139] Kaimori A, Potter J, Kaimori JY, Wang C, Mezey E, Koteish A. Transforming growth factor-beta1 induces an epithelial-to-mesenchymal transition state in mouse hepatocytes in vitro. J Biol Chem. 2007;282:22089-101.

[140] Moore KA, Polte T, Huang S, Shi B, Alsberg E, Sunday ME, et al. Control of basement membrane remodeling and epithelial branching morphogenesis in embryonic lung by Rho and cytoskeletal tension. Dev Dyn. 2005;232:268-81.

[141] Discher DE, Janmey P, Wang YL. Tissue cells feel and respond to the stiffness of their substrate. Science. 2005;310:1139-43.

[142] Guo WH, Frey MT, Burnham NA, Wang YL. Substrate rigidity regulates the formation and maintenance of tissues. Biophys J. 2006;90:2213-20.

[143] Tammi MI, Day AJ, Turley EA. Hyaluronan and homeostasis: a balancing act. J Biol Chem. 2002;277:4581-4.

[144] Luo Y, Kirker KR, Prestwich GD. Cross-linked hyaluronic acid hydrogel films: new biomaterials for drug delivery. J Control Release. 2000;69:169-84.

[145] Pouyani T, Prestwich GD. Functionalized derivatives of hyaluronic acid oligosaccharides: drug carriers and novel biomaterials. Bioconjug Chem. 1994;5:339-47.

[146] Shepard S, Becker H, Hartmann JX. Using hyaluronic acid to create a fetal-like environment in vitro. Ann Plast Surg. 1996;36:65-9.

[147] Vrochides D, Papanikolaou V, Pertoft H, Antoniades AA, Heldin P. Biosynthesis and degradation of hyaluronan by nonparenchymal liver cells during liver regeneration. Hepatology. 1996;23:1650-5.

[148] Toole BP, Wight TN, Tammi MI. Hyaluronan-cell interactions in cancer and vascular disease. J Biol Chem. 2002;277:4593-6.

[149] Brown TJ, Laurent UB, Fraser JR. Turnover of hyaluronan in synovial joints: elimination of labelled hyaluronan from the knee joint of the rabbit. Exp Physiol. 1991;76:125-34.

[150] Hu M, Sabelman EE, Lai S, Timek EK, Zhang F, Hentz VR, et al. Polypeptide resurfacing method improves fibroblast's adhesion to hyaluronan strands. J Biomed Mater Res. 1999;47:79-84.

[151] Aruffo A, Stamenkovic I, Melnick M, Underhill CB, Seed B. CD44 is the principal cell surface receptor for hyaluronate. Cell. 1990;61:1303-13.

[152] Wilting J, Buttler K, Schulte I, Papoutsi M, Schweigerer L, Manner J. The proepicardium delivers hemangioblasts but not lymphangioblasts to the developing heart. Dev Biol. 2007;305:451-9.

[153] Ogata T, Okuda K, Ueno T, Saito N, Aoyagi S. Serum hyaluronan as a predictor of hepatic regeneration after hepatectomy in humans. Eur J Clin Invest. 1999;29:780-5.

[154] Ravi N, Wan KT, Swindle K, Hamilton PD, Duan G. Development of techniques to compare mechanical properties of reversible hydrogels with spherical, square columnar and ocular lens geometry. Polymer. 2006;47:4203.

[155] Timmer MD, Ambrose CG, Mikos AG. Evaluation of thermal- and photo-crosslinked biodegradable poly(propylene fumarate)-based networks. J Biomed Mater Res A. 2003;66:811-8.

[156] Loboa EG, Wren TA, Beaupre GS, Carter DR. Mechanobiology of soft skeletal tissue differentiation--a computational approach of a fiber-reinforced poroelastic model based on homogeneous and isotropic simplifications. Biomech Model Mechanobiol. 2003;2:83-96.

[157] Forgacs G, Newman, S.A. Biological Physics of the Developing Embryo: Cambridge University Press; 2005.

[158] Lubkin SR, Murray JD. A mechanism for early branching in lung morphogenesis. J Math Biol. 1995;34:77-94.

[159] Forgacs G, Foty RA, Shafrir Y, Steinberg MS. Viscoelastic properties of living embryonic tissues: a quantitative study. Biophys J. 1998;74:2227-34.

[160] Foty RA, Forgacs G, Pfleger CM, Steinberg MS. Liquid properties of embryonic tissues: Measurement of interfacial tensions. Phys Rev Lett. 1994;72:2298-301.

[161] Chen HF, Chuang CY, Lee WC, Huang HP, Wu HC, Ho HN, et al. Surface Marker Epithelial Cell Adhesion Molecule and E-cadherin Facilitate the Identification and Selection of Induced Pluripotent Stem Cells. Stem cell reviews. 2011.

[162] Chen T, Yuan D, Wei B, Jiang J, Kang J, Ling K, et al. E-cadherin-mediated cell-cell contact is critical for induced pluripotent stem cell generation. Stem Cells. 2010;28:1315-25.

[163] Inaba M, Yuan H, Salzmann V, Fuller MT, Yamashita YM. E-cadherin is required for centrosome and spindle orientation in Drosophila male germline stem cells. PloS one. 2010;5:e12473.

[164] Smutny M, Yap AS. Neighborly relations: cadherins and mechanotransduction. J Cell Biol. 2010;189:1075-7.

[165] Patel VN, Rebustini IT, Hoffman MP. Salivary gland branching morphogenesis. Differentiation. 2006;74:349-64.

[166] Ewald AJ, Brenot A, Duong M, Chan BS, Werb Z. Collective epithelial migration and cell rearrangements drive mammary branching morphogenesis. Dev Cell. 2008;14:570-81.

[167] Watt FM, Hogan BLM. Out of Eden: stem cells and their niches. Science. 2000;287:1427.

[168] Bissell MJ, Radisky DC, Rizki A, Weaver VM, Petersen OW. The organizing principle: microenvironmental influences in the normal and malignant breast. Differentiation. 2002;70:537-46.

[169] Kurosawa H. Methods for inducing embryoid body formation: in vitro differentiation system of embryonic stem cells. Journal of bioscience and bioengineering. 2007;103:389-98.

[170] Jakab K, Norotte C, Damon B, Marga F, Neagu A, Besch-Williford CL, et al. Tissue engineering by self-assembly of cells printed into topologically defined structures. Tissue Engineering Part A. 2008;14:413-21.

[171] Truesdell C, Noll W. The Nonlinear Field Theories of Mechanics: Springer; 1965.

[172] Dong J, Wiley HS. Trafficking and proteolytic release of epidermal growth factor receptor ligands are modulated by their membrane-anchoring domains. J Biol Chem. 2000;275:557-64.

[173] Knauer DJ, Wiley HS, Cunningham DD. Relationship between epidermal growth factor receptor occupancy and mitogenic response. Quantitative analysis using a steady state model system. J Biol Chem. 1984;259:5623-31.

[174] Wiley HS, Shvartsman SY, Lauffenburger DA. Computational modeling of the EGF-receptor system: a paradigm for systems biology. Trends Cell Biol. 2003;13:43-50.

[175] Mow VC, Kuei SC, Lai WM, Armstrong CG. Biphasic Creep and Stress-Relaxation of Articular-Cartilage in Compression - Theory and Experiments. J Biomech Eng-T Asme. 1980;102:73-84.

[176] Beysens DA, Forgacs G, Glazier JA. Cell sorting is analogous to phase ordering in fluids. PNAS. 2000;97:9467-71.

[177] Jakab K, Damon B, Marga F, Doaga O, Mironov V, Kosztin I, et al. Relating cell and tissue mechanics: implications and applications. Dev Dyn. 2008;237:2438-49.

[178] Norotte C, Marga F, Neagu A, Kosztin I, Forgacs G. Experimental evaluation of apparent tissue surface tension based on the exact solution of the Laplace equation. EPL (Europhysics Letters). 2008:46003.

[179] Swartz MA, Fleury ME. Interstitial flow and its effects in soft tissues. Annual review of biomedical engineering. 2007;9:229-56.

[180] Chen Y, Schier AF. The zebrafish Nodal signal Squint functions as a morphogen. Nature. 2001;411:607-10.

[181] Francis K, Palsson BO. Effective intercellular communication distances are determined by the relative time constants for cyto/chemokine secretion and diffusion. PNAS. 1997;94:12258-62.

[182] McDowell N, Zorn AM, Crease DJ, Gurdon JB. Activin has direct long-range signalling activity and can form a concentration gradient by diffusion. Curr Biol. 1997;7:671-81.

[183] Reilly KM, Melton DA. Short-range signaling by candidate morphogens of the TGF beta family and evidence for a relay mechanism of induction. Cell. 1996;86:743-54.

[184] Savinell JM, Lee GM, Palsson BO. On the orders of magnitude of epigenic dynamics and monoclonal antibody production. Bioprocess and Biosystems Engineering. 1989;4:231-4.

[185] Olson MW, Toth M, Gervasi DC, Sado Y, Ninomiya Y, Fridman R. High affinity binding of latent matrix metalloproteinase-9 to the alpha2(IV) chain of collagen IV. J Biol Chem. 1998;273:10672-81.

[186] Aimes RT, Quigley JP. Matrix metalloproteinase-2 is an interstitial collagenase. Inhibitor-free enzyme catalyzes the cleavage of collagen fibrils and soluble native type I collagen generating the specific 3/4- and 1/4-length fragments. J Biol Chem. 1995;270:5872-6.

[187] Jiang A, Lehti K, Wang X, Weiss SJ, Keski-Oja J, Pei D. Regulation of membrane-type matrix metalloproteinase 1 activity by dynamin-mediated endocytosis. PNAS. 2001;98:13693-8.

[188] Remacle A, Murphy G, Roghi C. Membrane type I-matrix metalloproteinase (MT1-MMP) is internalised by two different pathways and is recycled to the cell surface. J Cell Sci. 2003;116:3905-16.

[189] Starbuck C, Lauffenburger DA. Mathematical model for the effects of epidermal growth factor receptor trafficking dynamics on fibroblast proliferation responses. Biotechnol Prog. 1992;8:132-43.

[190] Newman SA, Forgacs G, Hinner B, Maier CW, Sackmann E. Phase transformations in a model mesenchymal tissue. Phys Biol. 2004;1:100-9.

[191] Jain RK. 1995 Whitaker Lecture: delivery of molecules, particles, and cells to solid tumors. Ann Biomed Eng. 1996;24:457-73.

[192] Jain RK. Transport of Molecules, Particles, and Cells in Solid Tumors. Annual review of biomedical engineering. 1999;1:241-63.

[193] Scholander PF, Hargens AR, Miller SL. Negative pressure in the interstitial fluid of animals. Fluid tensions are spectacular in plants; in animals they are elusively small, but just as vital. Science. 1968;161:321-8.

[194] Wiig H, Reed RK, Aukland K. Measurement of interstitial fluid pressure: comparison of methods. Ann Biomed Eng. 1986;14:139-51.

[195] Wiig H, Rubin K, Reed RK. New and active role of the interstitium in control of interstitial fluid pressure: potential therapeutic consequences. Acta Anaesthesiologica Scandinavica. 2003;47:111-21.

[196] Chowdhury F, Na S, Li D, Poh YC, Tanaka TS, Wang F, et al. Material properties of the cell dictate stress-induced spreading and differentiation in embryonic stem cells. Nature materials. 2010;9:82-8.

[197] Flenner E, Marga F, Neagu A, Kosztin I, Forgacs G. Relating biophysical properties across scales. Curr Top Dev Biol. 2008;81:461-83.

[198] Foty RA, Pfleger CM, Forgacs G, Steinberg MS. Surface tensions of embryonic tissues predict their mutual envelopment behavior. Development (Cambridge, England). 1996;122:1611-20.

[199] Hutson MS, Ma X. Mechanical aspects of developmental biology: perspectives on growth and form in the (post)-genomic age. Preface. Phys Biol. 2008;5:015001.

[200] David R, Ninomiya H, Winklbauer R, Neumann AW. Tissue surface tension measurement by rigorous axisymmetric drop shape analysis. Colloids and surfaces. 2009;72:236-40.

[201] Kalantarian A, Ninomiya H, Saad SM, David R, Winklbauer R, Neumann AW. Axisymmetric drop shape analysis for estimating the surface tension of cell aggregates by centrifugation. Biophys J. 2009;96:1606-16.

[202] Ninomiya H, Winklbauer R. Epithelial coating controls mesenchymal shape change through tissue-positioning effects and reduction of surface-minimizing tension. Nat Cell Biol. 2008;10:61-9.

[203] Foty RA, Steinberg MS. The differential adhesion hypothesis: a direct evaluation. Dev Biol. 2005;278:255-63.

[204] Lubkin SR, Li Z. Force and deformation on branching rudiments: cleaving between hypotheses. Biomech Model Mechanobiol. 2002;1:5-16.

[205] Wan X, Li Z, Lubkin SR. Mechanics of mesenchymal contribution to clefting force in branching morphogenesis. Biomech Model Mechanobiol. 2008;7:417-26.

[206] Lubkin SR, Jackson T. Multiphase mechanics of capsule formation in tumors. J Biomech Eng. 2002;124:237-43.

[207] Fata JE, Leco KJ, Moorehead RA, Martin DC, Khokha R. Timp-1 is important for epithelial proliferation and branching morphogenesis during mouse mammary development. Dev Biol. 1999;211:238-54.

[208] Hammer. Diffusion and Direct Signaling Models are Numerically Equivalent. J Theor Biol. 1998;192:129-30.

[209] Bratt-Leal AM, Carpenedo RL, McDevitt TC. Engineering the embryoid body microenvironment to direct embryonic stem cell differentiation. Biotechnol Prog. 2009;25:43-51.

[210] Barocas VH, Moon AG, Tranquillo RT. The fibroblast-populated collagen microsphere assay of cell traction force--Part 2: Measurement of the cell traction parameter. J Biomech Eng. 1995;117:161-70.

[211] Larsen WJ. Human embryology. 3rd ed. New York: Churchill Livingstone; 2001.

[212] Djin WAN, Miller NR, Bamber JC, Chapelon JY, Melodelima D. Impact of Real Liver Motion on HIFU Treatments: an in-vivo-data-based modeling. In: Emad SE, editor.: AIP; 2009. p. 175-9.

[213] Feng M, Balter JM, Normolle D, Adusumilli S, Cao Y, Chenevert TL, et al. Characterization of pancreatic tumor motion using cine MRI: surrogates for tumor position should be used with caution. International journal of radiation oncology, biology, physics. 2009;74:884-91.

[214] Kolen AF, Miller NR, Ahmed EE, Bamber JC. Characterization of cardiovascular liver motion for the eventual application of elasticity imaging to the liver in vivo. Phys Med Biol. 2004;49:4187-206.

[215] Doerr R, Zvibel I, Chiuten D, D'Olimpio J, Reid LM. Clonal growth of tumors on tissue-specific biomatrices and correlation with organ site specificity of metastases. Cancer Res. 1989;49:384-92.

[216] Rojkind M, Gatmaitan Z, Mackensen S, Giambrone MA, Ponce P, Reid LM. Connective tissue biomatrix: its isolation and utilization for long-term cultures of normal rat hepatocytes. J Cell Biol. 1980;87:255-63.

[217] Zhang Y, He Y, Bharadwaj S, Hammam N, Carnagey K, Myers R, et al. Tissue-specific extracellular matrix coatings for the promotion of cell proliferation and maintenance of cell phenotype. Biomaterials. 2009;30:4021-8.

[218] Kiprilov EN, Awan A, Desprat R, Velho M, Clement CA, Byskov AG, et al. Human embryonic stem cells in culture possess primary cilia with hedgehog signaling machinery. J Cell Biol. 2008;180:897-904.

[219] Cartwright JH, Piro N, Piro O, Tuval I. Fluid dynamics of nodal flow and left-right patterning in development. Dev Dyn. 2008;237:3477-90.

[220] Yu J, Vodyanik MA, Smuga-Otto K, Antosiewicz-Bourget J, Frane JL, Tian S, et al. Induced pluripotent stem cell lines derived from human somatic cells. Science. 2007;318:1917-20.

[221] Takahashi K, Tanabe K, Ohnuki M, Narita M, Ichisaka T, Tomoda K, et al. Induction of pluripotent stem cells from adult human fibroblasts by defined factors. Cell. 2007;131:861-72.

[222] Jiang P, Rushing SN, Kong CW, Fu J, Lieu DK, Chan CW, et al. Electrophysiological properties of human induced pluripotent stem cells. Am J Physiol Cell Physiol. 2010;298:C486-95.

[223] Wang K, Xue T, Tsang SY, Van Huizen R, Wong CW, Lai KW, et al. Electrophysiological properties of pluripotent human and mouse embryonic stem cells. Stem Cells. 2005;23:1526-34.

[224] Marshall WF. The cell biological basis of ciliary disease. J Cell Biol. 2008;180:17-21.

[225] Cole DG. Kinesin-II, coming and going. J Cell Biol. 1999;147:463-6.

[226] Davenport JR, Yoder BK. An incredible decade for the primary cilium: a look at a once-forgotten organelle. Am J Physiol Renal Physiol. 2005;289:F1159-69.

[227] Pazour GJ, Rosenbaum JL. Intraflagellar transport and cilia-dependent diseases. Trends Cell Biol. 2002;12:551-5.

[228] Praetorius HA, Spring KR. Bending the MDCK cell primary cilium increases intracellular calcium. The Journal of membrane biology. 2001;184:71-9.

[229] Schwartz EA, Leonard ML, Bizios R, Bowser SS. Analysis and modeling of the primary cilium bending response to fluid shear. Am J Physiol. 1997;272:F132-8.

[230] Masyuk AI, Masyuk TV, Splinter PL, Huang BQ, Stroope AJ, LaRusso NF. Cholangiocyte cilia detect changes in luminal fluid flow and transmit them into intracellular Ca2+ and cAMP signaling. Gastroenterology. 2006;131:911-20.

[231] Gradilone SA, Masyuk AI, Splinter PL, Banales JM, Huang BQ, Tietz PS, et al. Cholangiocyte cilia express TRPV4 and detect changes in luminal tonicity inducing bicarbonate secretion. PNAS. 2007;104:19138-43.

[232] Masyuk AI, Gradilone SA, Banales JM, Huang BQ, Masyuk TV, Lee SO, et al. Cholangiocyte primary cilia are chemosensory organelles that detect biliary nucleotides via P2Y12 purinergic receptors. Am J Physiol Gastrointest Liver Physiol. 2008;295:G725-34.

[233] Iomini C, Tejada K, Mo W, Vaananen H, Piperno G. Primary cilia of human endothelial cells disassemble under laminar shear stress. J Cell Biol. 2004;164:811-7.

[234] Quarmby LM, Parker JD. Cilia and the cell cycle? J Cell Biol. 2005;169:707-10.

[235] Hamill OP, Martinac B. Molecular basis of mechanotransduction in living cells. Physiol Rev. 2001;81:685-740.

[236] Sachs F, Morris CE. Mechanosensitive ion channels in nonspecialized cells. Reviews of physiology, biochemistry and pharmacology. 1998;132:1-77.

[237] Holle AW, Engler AJ. Cell rheology: Stressed-out stem cells. Nature materials. 2010;9:4-6.

[238] Desprat N, Supatto W, Pouille PA, Beaurepaire E, Farge E. Tissue deformation modulates twist expression to determine anterior midgut differentiation in Drosophila embryos. Dev Cell. 2008;15:470-7.

[239] Wozniak MA, Chen CS. Mechanotransduction in development: a growing role for contractility. Nat Rev Mol Cell Biol. 2009;10:34-43.

[240] Nonaka S, Shiratori H, Saijoh Y, Hamada H. Determination of left-right patterning of the mouse embryo by artificial nodal flow. Nature. 2002;418:96-9.

[241] Seguin CA, Draper JS, Nagy A, Rossant J. Establishment of endoderm progenitors by SOX transcription factor expression in human embryonic stem cells. Cell stem cell. 2008;3:182-95.

[242] Vallier L, Mendjan S, Brown S, Chng Z, Teo A, Smithers LE, et al. Activin/Nodal signalling maintains pluripotency by controlling Nanog expression. Development (Cambridge, England). 2009;136:1339-49.

[243] Morrison GM, Oikonomopoulou I, Migueles RP, Soneji S, Livigni A, Enver T, et al. Anterior definitive endoderm from ESCs reveals a role for FGF signaling. Cell stem cell. 2008;3:402-15.

[244] Huang BQ, Masyuk TV, Muff MA, Tietz PS, Masyuk AI, Larusso NF. Isolation and characterization of cholangiocyte primary cilia. Am J Physiol Gastrointest Liver Physiol. 2006;291:G500-9.

[245] Schmelzer E, Zhang L, Melhem A, Yao H, Turner W, McClelland R, et al. Hepatic Stem Cells. In: Potten CS, Clarke RB, Wilson J, Renehan AG, editors. Tissue Stem Cells. New York: Taylor and Rancis Group; 2006. p. 161-214.

[246] Vincent JFV. Structural biomaterials. Rev. ed. Princeton, N.J.: Princeton University Press; 1990.

[247] Mansour J. Biomechanics of cartilage. In: Oatis C, editor. Kinesiology: The Mechanics and Pathomechanics of Human Movement. Philadelphia: Lippincott Williams & Wilkins; 2003. p. 66-79.